Lateral variations of scattering properties and implications for monitoring with coda wave sensitivity kernels

Chantal van Dinther

To cite this version:

Chantal van Dinther. Lateral variations of scattering properties and implications for monitoring with coda wave sensitivity kernels. Earth Sciences. Université Grenoble Alpes [2020-..], 2021. English. NNT : 2021GRALU014 . tel-03275905

HAL Id: tel-03275905
https://theses.hal.science/tel-03275905v1

Submitted on 1 Jul 2021

THÈSE

Pour obtenir le grade de

DOCTEUR DE L'UNIVERSITÉ GRENOBLE ALPES
Spécialité : **Sciences de la Terre, de l'Univers et de l'Environnement**

Arrêté ministériel : 7 Août 2006

Présentée par

Chantal van Dinther

Thèse dirigée par **Michel Campillo**
et codirigée par **Ludovic Margerin**

préparée au sein de **l'Institut des Sciences de la Terre (ISTerre)**
et de l'école doctorale **Terre Univers Environnement**

Lateral variations of scattering properties and implications for monitoring with coda wave sensitivity kernels

Variations latérales des propriétés de diffusion et implications pour le suivi temporel avec des ondes de la coda

Thèse soutenue publiquement le **30 mars 2021**,
devant le jury composé de :

Florent Brenguier
Physicien d'Observatoire (professeur) at Université Grenoble Alpes, ISTerre, Grenoble, Président
Michel Campillo
Professor at Université Grenoble Alpes, ISTerre, Grenoble, Directeur de thèse
Ludovic Margerin
Directeur de reserche (professeur) at Université de Toulouse III Paul Sabatier, IRAP, Toulouse, Co-Directeur de thèse
Takeshi Nishimura
Professor at Tohoku University, Sendai, Japan, Rapporteur
Gregor Hillers
Associate Professor at University of Helsinki, Helsinki, Finland, Rapporteur
Bérénice Froment
Ingénieur-chercheur (docteur) at Institut de Radioprotection et de Sûreté Nucléaire, Paris, Examinatrice

Abstract

Intrinsic absorption and scattering properties provide us with information about the physical state and heterogeneity of the Earth's crust. Moreover, they are important input parameters for spatial sensitivity kernels in coda wave monitoring applications. The scattering and intrinsic attenuation coefficients are usually obtained by observing the energy decay of earthquakes, leading to sparse spatial sampling and therefore average scattering values over a large region.

In the first part of this thesis, we therefore use ambient noise recordings of a dense array to derive the scattering properties at small length scale. The study uses ambient noise cross-correlations to analyse the energy decay and scattering properties over a part of the North Anatolian Fault (NAF; Turkey) from ambient noise records in the frequency band 0.1 - 0.5 Hz. The target region has varying geological characteristics and is highly faulted around the northern strand of the NAF. In the noise correlation we measured the spatio-temporal energy decay of the coda waves. The local scattering and attenuation properties are obtained by global optimization of a 2-D solution of the radiative transfer equation for surface waves. We found that the mean free path and attenuation coefficient are considerably varying laterally with strong scattering observed in the region lying along the northern strand of NAF. Furthermore, a concentration of energy in the fault zone for a limited time was observed. We verified our observations with a phonon based Monte Carlo simulation, confirming the large contrast of heterogeneity between a narrow NAF and the surrounding crust.

The findings of this first study are used in the second study of this thesis. The second part focuses on the implications of non-uniform scattering properties for monitoring with coda wave sensitivity kernels. For monitoring the temporal evolution of the sub-surface coda wave sensitivity kernels are required that linearly relate observed changes in recordings to physical medium changes. We computed travel-time, scattering and decorrelation kernels using a flexible Monte Carlo method, which is again based on the solution of the scalar version of the radiative transfer equation. In this work we showed that non-uniform scattering properties can have a profound but non-intuitive effect on coda wave sensitivity kernels. Moreover, a contrast in scattering may lead to additional energy transport channels that connect the source and receiver, depending on the mean free time versus lapse-time. Hence, it would be misleading to neglect the effect of the scattering distribution. Finally, we visually demonstrated the difference between travel-time and decorrelation kernels and consequently the importance of the angular dependency of the intensities. This study therefore emphasises that one needs to be careful with applying physical approximations to the wavefield, such as the diffusion approximation and opens up new venues for imaging of spatio-temporal variations of crustal properties.

Keywords: Wave scattering and diffraction; Coda waves; Seismic attenuation; Numerical modelling; Seismic noise; Fault zone rheology.

Résumé

Les propriétés d'absorption et de diffusion nous fournissent des informations sur l'état physique et l'hétérogénéité de la croûte terrestre. En outre, elles sont des paramètres d'entrée importants pour les noyaux de sensibilité spatiale dans les applications de surveillance fondées sur les ondes de coda. Les coefficients de diffusion et d'atténuation intrinsèque sont généralement obtenus en observant la décroissance d'énergie des tremblements de terre, ce qui conduit à un échantillonnage spatial épars et donc à des valeurs de diffusion moyennées sur une grande région.

La première étude de cette thèse utilise les corrélations croisées du bruit ambiant pour analyser la décroissance énergétique et les propriétés de diffusion sur une partie de la faille de l'Anatolie du Nord (NAF ; Turquie) à partir des enregistrements du bruit ambiant par un réseau dense dans la bande de fréquence 0,1 - 0,5 Hz. La région cible présente des caractéristiques géologiques variées et est fortement faillée autour de la partie nord de la faille nord-anatolienne. Dans la corrélation du bruit, nous avons mesuré la décroissance énergétique spatio-temporelle des ondes de la coda. Les propriétés de diffusion et d'atténuation locales sont obtenues par optimisation globale d'une solution 2-D de l'équation de transfert radiatif pour les ondes de surface. Nous avons constaté que le libre parcours moyen et le coefficient d'atténuation varient

spatialement de façon importante, une forte diffusion étant observée dans la région située le long de la branche nord de la NAF. De plus, une concentration d'énergie dans la zone de faille a été observée pendant un temps limité. Nous avons vérifié nos observations avec une simulation de Monte Carlo basée, confirmant le grand contraste d'hétérogénéité entre la zone de faille étroite et la croûte environnante.

Les résultats de cette première étude sont utilisés dans la deuxième étude de cette thèse. La deuxième partie se concentre sur les implications des propriétés de diffusion non uniforme pour les applications de surveillance fondées sur les noyaux de sensibilité des ondes de la coda. Pour le suivi de l'évolution temporelle du sous-sol, nous avons besoin de noyaux de sensibilité établissant une relation linéaire entre les changements observés dans les enregistrements sismiques et les changements du milieu physique. Dans le cas de perturbations de propriétés de diffusion, nous avons calculé les noyaux de sensibilité pour trois observables: le temps de propagation des ondes, leur intensité et leur décohérence. Pour cela, nous avons utilisé une méthode de Monte-Carlo flexible, fondée sur un modèle de transport radiatif scalaire à 2D.

Nous avons montré que des propriétés de diffusion non uniformes peuvent avoir un effet profond mais non intuitif sur les noyaux de sensibilité des ondes de coda. De plus un contraste des propriétés de diffusion peut donner naissance à de nouveaux chemins de transport d'énergie entre la source et le récepteur. L'importance de ce phénomène dépend du contraste de libre parcours moyen et du temps de propagation des ondes. Il est donc erroné de négliger les variations spatiales des propriétés de diffusion dans le calcul des sensibilités. Enfin, nous avons illustré la différence entre les noyaux de sensibilité du temps de propagation et de la décohérence, montrant ainsi l'importance de la dépendance angulaire des intensités. Cette étude souligne

donc qu'il faut être prudent dans l'application d'approximations physiques au champ d'onde, comme l'approximation de diffusion et ouvre des perspectives prometteuses pour l'imagerie des variations spatio-temporelles des propriétés de diffusion de la croûte terrestre.

Mots-clés: Diffusion et diffraction des ondes ; ondes de coda ; atténuation sismique ; modélisation numérique ; bruit sismique ; rhéologie des zones de faille.

Acknowledgements

I am very grateful for the years that I have spent in Grenoble and at ISTerre. There are some people I would like to thank for the great experience during my PhD:

First, I would like to thank my advisors Michel Campillo and Ludovic Margerin for providing me this great opportunity to work with them on such an interesting and challenging topic. During the last three years they were always available to guide and advise me when it was needed. Merci beaucoup!

Thanks to my jury members, Takeshi Nishimura, Gregor Hillers, Bérénice Froment and Florent Brenguier, for their time to read my manuscript and participate in my defense.

I would also like to thank my thesis committee, Cécile Lasserre and Marco Bohnhoff, for the fruitful discussions.

I am grateful to have had the opportunity to work at ISTerre, an environment with a lot of inspiring colleagues. I would like to thank all my colleagues from the lab and a special thanks to Albanne Lecointre, Laurent Stehly, Pièrre Boué, Leonard Seydoux and Qingyu Wang for their help with certain software packages. I would also like to thank my collaborators of the F-Image team, inside and outside ISTerre, for the great discussions and moments we have had.

Graag wil ik mijn vrienden en familie bedanken voor hun support en vele tripjes naar Grenoble en omgeving. Dankjewel Robbert en Vincent voor jullie hulp met bepaalde software. Janneke, bedankt voor het proeflezen van delen van dit proefschrift.

I am thankful for the friends that I have made in Grenoble, inside and outside the lab, with whom I had a great time. And a special thanks to Sophie for her unlimited support!

Contents

Chapter 1

Introduction

1.1 Context of thesis

Understanding the physical processes at depth is the main purpose of most geophysical studies. Knowledge about the physical properties of the lithosphere can aid our comprehension on these processes and provides insights required to asses seismic hazards. In classical seismology, the Earth is considered to consist of horizontal layers having differing elastic properties, typically determined using travel-time information of body waves and the dispersion of surface waves. However, in reality, the Earth's lithosphere is heterogeneous in nature at different length scales. Small heterogeneities of random sizes and contrasts of physical properties causes seismic energy to spread in space. These heterogeneities, or *scatterers*, such as faults and fractures, lead to very complex wavefield characteristics. The presence of scatterers can therefore be observed as the long wave trains after the P, S - and surface wave arrivals at the end of a seismogram, known as *coda waves*. Coda waves have been disregarded for a long time, because the presence of scatterers causes the wavefield to be rather complex. Only since the pioneering work of Aki (1969) and Aki and Chouet (1975) the interest in coda waves has started. These authors discovered that coda waves contain valuable information on regional scattering and attenuation properties. Currently, it is widely accepted that coda waves are deterministic and reproducible signals. Due to the scattering process, coda waves can spend a long time in the medium. This provides the opportunity to sample the target medium densely for late lapse-times and accumulate the effect of changes in the medium.

Most studies focusing on the detection and/or localisation of medium changes exploit the continuous ambient noise field to reconstruct 'virtual' seismograms (e.g. Obermann et al. 2013b; Sánchez-Pastor, Obermann, and Schimmel 2018; Hirose et al. 2020; Sens-Schönfelder and Wegler 2006; Mao et al. 2019; Hillers et al. 2020; Hillers et al. 2015b; Mordret et al. 2010; Brenguier et al. 2016). Oceanic and atmospheric interactions cause the Earth's surface to permanently vibrate, forming an ambient noise source that can be recorded at any location. Starting in the field of acoustics, Weaver and Lobkis (2001) and Lobkis and Weaver (2001) demonstrated that the Green's function can be obtained by correlating diffusive wavefields. Later in the field of seismology, Paul and Campillo (2001) and Campillo and Paul (2003) showed that a ballistic waves Green's function can be reconstructed in a similar manner using passive ambient noise recordings. These approximate Green's functions, or cross-correlation functions contain comparable characteristics to actual earthquake seismograms, including coda waves, and can be seen as 'virtual' seismograms. Consequently, with the omnipresent noise field, these cross-correlation functions provide the perfect opportunity to image and monitor the subsurface without being dependent on the spatial and temporal distribution of earthquakes. Particularly for monitoring applications this is favourable, since the noise field is always present. It simplifies the comparison of the subsurface's state at different times with respect to finding similar earthquake records to observe changes of the rock at depth. Similarly for characterising scattering and attenuation parameters, cross-correlation functions provide the opportunity to exclude the time and space dependence on earthquake occurrence.

The main challenge is, however, that the effect of scattering on the amplitude of seismic waves is one of the most poorly understood physical processes controlling seismic energy attenuation in the Earth's lithosphere. As a consequence, most studies assume a uniform distribution of scattering properties for imaging and monitoring of the Earth's crust, while it is well-known that in certain settings, especially for fault zones and volcanic areas, the scatterers are non-uniformly distributed.

Therefore, this thesis presents research on laterally varying scattering properties. More specifically, some of the central questions to answer in this work are: Can we exploit the opportunity to construct virtual seismograms on a dense array to obtain laterally varying scattering properties over short spatial distances (in the order of kilometers)? If so, can we use these values to investigate the implications of non-uniform scattering on coda wave sensitivity kernels for realistic settings? Furthermore, do any of these insights lead to constraints on the physical assumptions to describe seismic wave propagation in the Earth's lithosphere?

1.2 Outline of thesis

In this thesis I try to answer above stated research questions, which are focused on the aspect of non-uniformly distributed scattering properties. For this, the thesis is structured into two parts.

Part I focuses on key concepts, definitions and methodologies involved in imaging seismic wave attenuation properties and subsurface monitoring by exploiting coda waves of both earthquake records and cross-correlation functions.

Chapter 2 introduces important definitions and concepts related to wave propagation in complex media.

Chapter 3 starts with a heuristic approach on retrieving 'virtual' seismograms using continuous ambient noise records. Furthermore, it provides a comprehensive overview on methodologies for imaging scattering properties and monitoring the dynamic evolution of the subsurface using scattered waves. In particular, the spatial localisation of medium changes using sensitivity kernels is discussed in the last section of the chapter.

Part II is dedicated to derive non-uniform scattering properties and study their effects on spatial sensitivities, with an application to the North Anatolian Fault zone.

In Chapter 4 we verify the feasibility of using ambient noise recordings in the frequency band of 0.1- 0.5 Hz to image laterally varying scattering properties in the North Anatolian Fault zone in Turkey. Moreover, we show phonon-based Monte Carlo simulations to confirm a seismic signature of the fault zone.

Chapter 5 explores the implications of non-uniform scattering properties for the spatial sensitivity of coda waves. Building on the work of e.g. Planès et al. 2014;

Obermann et al. 2013b; Pacheco and Snieder 2005; Snieder 2006 and in particular on Mayor, Margerin, and Calvet (2014) and Margerin et al. (2016) we construct sensitivity kernels for realistic settings that have non-uniformly distributed scattering properties. Separate sensitivity kernels for travel-time, scattering and decorrelation changes are numerically obtained by performing Monte Carlo simulations based radiative transfer theory. The differences in spatio-temporal sensitivities between uniform media and non-uniform media like volcanic and fault zone settings are described in detail for each type of kernel.

Part I

Concepts and Methods

Chapter 2

Scattering

Contents

This chapter introduces all concepts and definitions related to scattering that are necessary to understand the research performed and described in this thesis. The main waves studied in current work are coda waves, so let us start by explaining what coda waves are, before moving on to important length scales required to describe scattering. This chapter finishes by introducing the concept of scattering using a statistical approach; first to characterise wave propagation and later to describe random media.

2.1 Introducing coda waves

A seismogram shows ground motion, generated by arriving seismic waves, as a function of time. The observed wave field is composed of pressure (P) and shear (S) body waves, surface waves and their coda waves. The different wave types, or modes, have different propagation velocities, therefore the ballistic arrivals of the various modes are recorded at different lapse-times. Fig. 2.1 A shows an example of a seismogram with the various modes. The end-tail of the seismogram is referred to as the *coda*. It consists of waves arriving at slightly different times due to variations in the travel path taken. Its primary contributions are from singly and multiply scattered S waves. In general, the wave train following a direct arrival of a wave is categorized as the coda of that wave type. This gives a set of coda waves, including P coda, S coda, Rayleigh coda and Lg coda waves. Often the coda wave at the end of the seismogram has contributions of multiple wave types, which are difficult to separate. The observation of coda in seismograms has been interpreted as evidence for the existence of random heterogeneities in the Earth's lithosphere (Aki and Chouet 1975).

The mean square (MS) envelope of a seismogram represents the time trace of the wave energy density (Fig. 2.1 B). After the initial surface wave arrivals, we observe an exponential decay of the envelope, the coda attenuation, Q_c^{-1}. The inverse of the coda attenuation is commonly referred to as 'coda quality factor', or

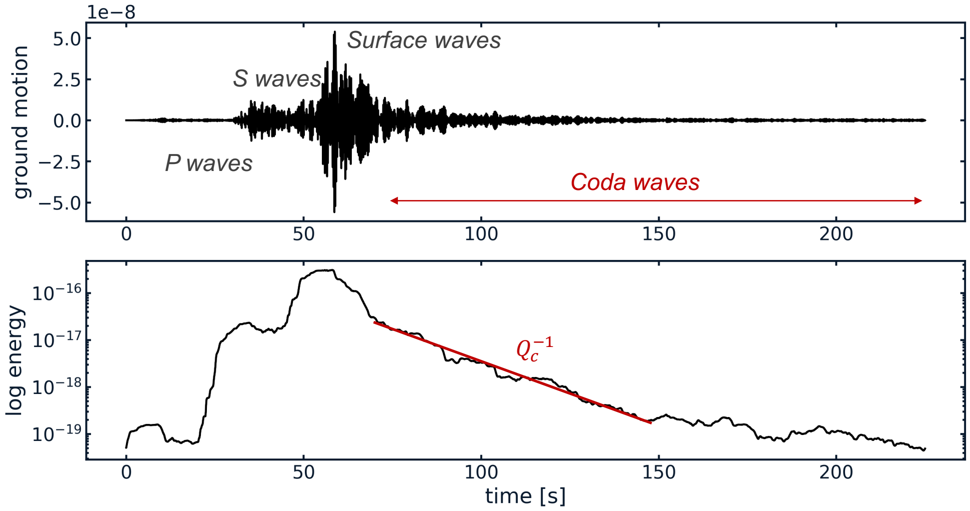

Figure 2.1: Top: Seismogram of earthquake in France, for frequency range 4-8 Hz. Bottom: Semi-logarithmic plot of the smoothed energy. Red line indicates slope of the envelope for Q_c^{-1}measurement (see text).

simply ‘coda Q’. In general there are three main processes that contribute to the attenuation of seismic energy: (1) geometric spreading; (2) scattering attenuation and (3) intrinsic attenuation, an anelastic process in which seismic energy is converted to heat. Although the physical interpretation of Q_c is still under debate, it is known that this parameter depends on the intrinsic attenuation coefficient Q_i, and the scattering coefficient Q_{sc}. Those coefficients are a measure to describe intrinsic attenuation and scattering strength, respectively, and are defined in more detail in the Section 2.2. Furthermore, Q_c shows lateral variations at regional scale (e.g. Hoshiba 1991; Gusev 1995; Calvet and Margerin 2013). Energy leakage can play an important role in the lateral variations of coda attenuation, especially for areas with a large contrast in scattering strength between the Earth’s crust and the mantle (Margerin et al. 1999; Korn 1990; Margerin, Campillo, and Tiggelen 1998). A key factor in the definition of Q_c is the dominant propagation regime of the waves. This may range from a regime where direct and single scattering waves dominate, with $Q_c^{-1} = Q_{sc}^{-1} + Q_i^{-1}$, to $Q_c \approx Q_i$ for the diffusive regime. The propagation regimes are explained in more detail in the next section (Section 2.3.1). Estimations of Q_c^{-1} can be quantified empirically using the following algebro-exponential decay relation:

$$E(f,t) = S(f)\ \exp[-2\pi\ t\ f\ Q_c^{-1}(f)]\ t^{-\alpha} \tag{2.1}$$

where $E(f,t)$ is the MS energy envelope at lapse time t around frequency f. $S(f)$ is a frequency-dependent factor combining the source magnitude and the site effect at the station (discussed below). The exponent α is a fixed parameter that depends on both the regime of scattering (from single scattering to diffusion) and the dominant wave type in the coda (body waves or surface waves). α typically varies between 1 and 2. In practice, Q_c^{-1} is often estimated by performing a linear regression on the log of the envelope to fit the slope of the energy decay in the coda, as shown in Fig. 2.1 B.

In order to compare Q_c values for different source-receiver pairs, one needs to compensate for the source magnitude and site effects ($S(f)$ in Eq. 2.1). This is typically done by applying the 'coda normalisation' technique. This technique is based on the assumption that the coda energy distribution from an earthquake is spatially uniform after sufficiently large lapse times in a certain frequency band (diffusion approximation).

Despite coda normalisation, we still observe a difference in envelope shape for regions with distinctively different geology e.g. an volcanic region, which has strong scattering, versus normal crust, which has weaker scattering strength.

In addition to coda attenuation, which is stronger in volcanic regions, variations

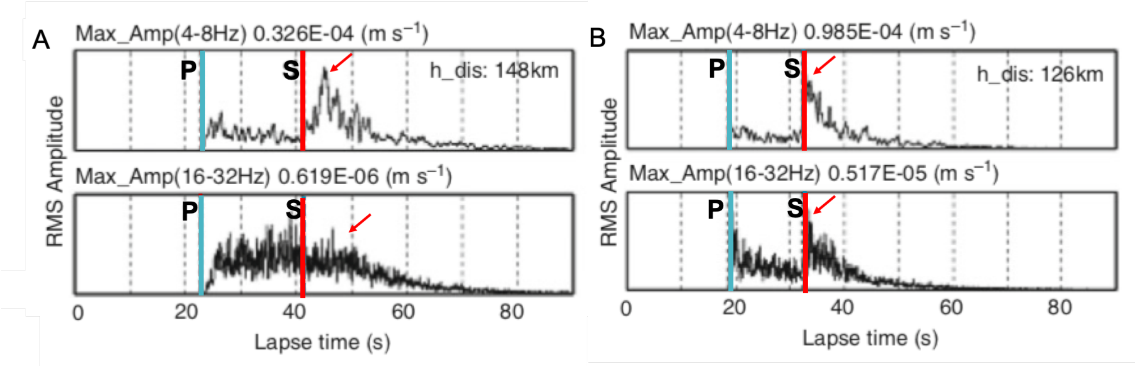

Figure 2.2: Path dependent S-wave envelopes. A) S-wave envelopes for earthquake in the western Hidaka, Japan. The path crossed a volcanic area, and thus the maximum of the envelope (red arrow) is delayed with respect to the S-wave onset (red line). The P-wave onset is depicted as a blue line. B) S-wave envelopes for earthquake in northern Honshu, Japan. The path did not cross a volcanic area. Adjusted after Takahashi et al. (2007).

in peak time delay are observed. The peak time delay refers to the time delay of the maximum of the envelope with respect to the onset of the S waves. It is larger for the recording in the volcanic region than for the normal crust (Takahashi et al. 2007), due to the difference in scattering strength. This phenomenon is known as 'envelope broadening' and is another key observation of heterogeneity in the Earth's lithosphere (Obara and Sato 1995). Fig. 2.2 illustrates envelope broadening for earthquake records in Japan. One record crosses a volcanic region (A) where the peak of the envelope is delayed with respect to the S-wave arrival. The other record does not cross a highly scattering volcanic area (B), therefore the peak of the envelope is closer to the S-wave arrival.

An observation supporting the principle of multiple scattering as the origin of coda waves, is the stabilization of the energy ratio of different wave types, e.g. between pressure and shear waves, $\frac{E_p}{E_s}$, and between horizontal and vertical components, $\frac{H^2}{V^2}$ (Weaver 1982; Shapiro et al. 2000; Hennino et al. 2001; Margerin et al. 2009;

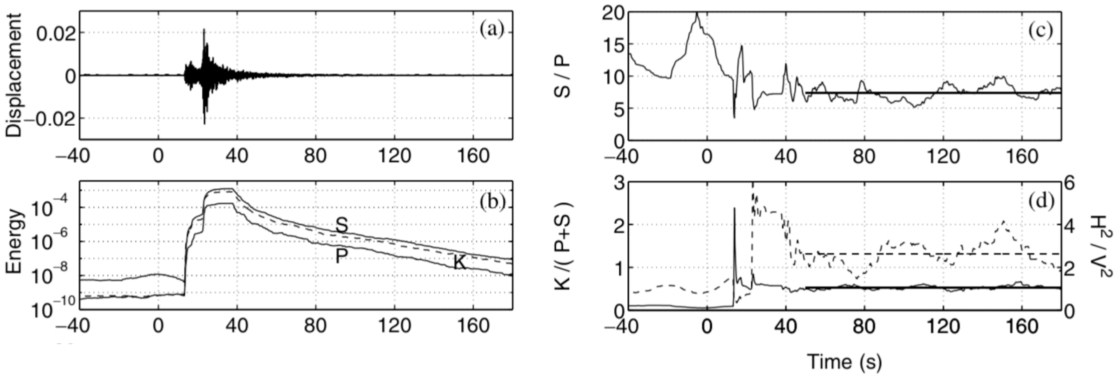

Figure 2.3: Observed seismogram for a magnitude 4.3 event at 35 km epicentral distance in Mexico, bandpassed between 1 and 3 Hz. A) Linear plot of the bandpassed displacement as a function of time, including annotations of wave modes. B) Semi-logarithmic plot of the energy density. The kinetic energy (K, dashed line), shear energy (S), and compressional energy (P) are separately plotted . C) Linear plot of the energy ratio $\frac{S}{P}$. D) Linear plot of the energy ratios $\frac{K}{S+P}$ (solid line) and $\frac{H^2}{V^2}$ (dashed line). The horizontal lines indicate the estimated time average. Adjusted from Hennino et al. (2001).

Sánchez-Sesma et al. 2011). This stabilisation of energy ratios is also known as *equipartition* and is based on the tendency of multiple scattering to homogenise the energy distribution in phase space. Fig. 2.3A shows an example of a local earthquake in Mexico where Hennino et al. (2001) observed equipartition of seismic waves. The first 50 s of the recording show fluctuations of $\frac{E_p}{E_s}$ (Fig. 2.3C) and $\frac{H^2}{V^2}$ (Fig. 2.3D) ratios, whereas after 50 s all wave modes are equiprobably present due to successive scattering events on the heterogeneities. In other words, the polarisation of the initial wave field imposed by the source completely vanished after multiple scattering events. The temporal stabilization of the $\frac{H^2}{V^2}$ ratio is in fact a direct observable of the equipartition of the modes and reflects the multiple-scattering regime.

2.2 Introducing length scales of scattering

Several length scales are involved when describing seismic wave scattering. Fig. 2.4 shows the graphical representation of the most important ones. From the left side of the figure an incident wave arrives, encounters a scatterer, or diffraction point, and changes propagation direction by an angle θ.

A central quantity in scattering theory is the *scattering mean free path*, denoted by ℓ. It is a physical property used to describe a scattering medium and also known as the reciprocal of the *total scattering coefficient*, g_0. The scattering mean free path is the typical length scale beyond which a wave is attenuated significantly due to scattering. It can be seen as the characteristic length between two scattering events of a specific medium as presented in Fig. 2.4. Note, however, that ℓ is not to be interpreted as the geometrical distance between scatterers. We can express the scattering power of a medium with ℓ (or g_0^{-1}) as:

$$\ell = \frac{1}{n\,\sigma_0} = g_0^{-1} \tag{2.2}$$

with n the number density of scatterers; σ_0 is the total scattering cross-section, which is dependent on size, shape and impedance contrast and indicates the capacity to deviate waves. Note that if we describe the scattering power with ℓ (or g_0^{-1}) we cannot distinguish between a small number of strong scatterers and a large number of weak scatterers. The total scattering cross-section is defined as:

$$\sigma_0 = \int \frac{d\sigma(\Omega)}{d\Omega} d\Omega \tag{2.3}$$

where $\frac{d\sigma}{d\Omega}$ is the *differential scattering cross-section*. Here the differential scattering

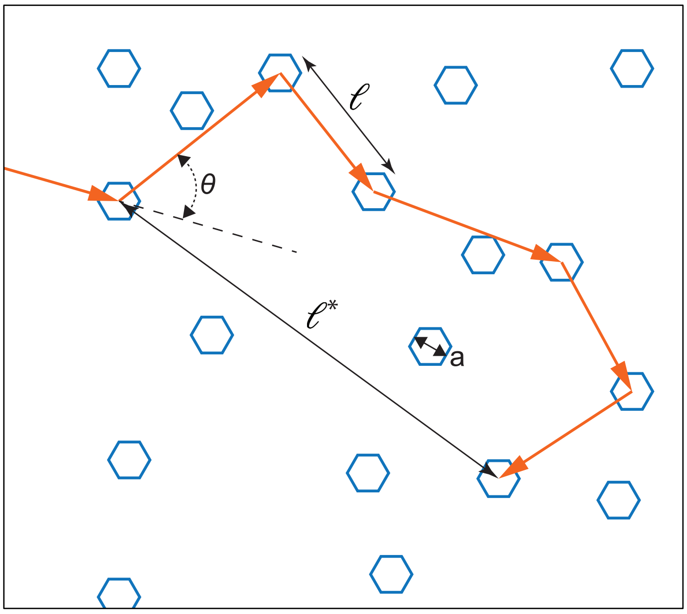

Figure 2.4: Graphical representation of scattering mean free path (ℓ), transport mean free path (ℓ^*) and scattering size (a). The blue hexagons represent the scatterers or medium inhomogeneities. The red arrows represent the seismic rays, where the most left one is the incident wave that changes propagation direction with angle θ after encountering a scatterer.

cross-section is a measure of the scattering power of an individual scatterer (Fig. 2.5), which is the scattered wave energy generated per time in a solid angle ($d\Omega$) for a unit incident energy flux density (J^0). The size of a scatterer, indicated by a, is yet another essential length, especially with respect to the wavelength.

Additionally, the scattering mean free path is used to describe scattering strength and to define the scattering attenuation coefficient, $Q_{sc} = \omega\ell/c$ (or in time as $Q_{sc} = \omega\tau$), with ω as the angular frequency, c as the seismic velocity and τ as the scattering mean free time.

Another physical length to describe scattering is the *transport mean free path*, ℓ^*. It is the distance at which a wave loses memory of its initial propagation direction

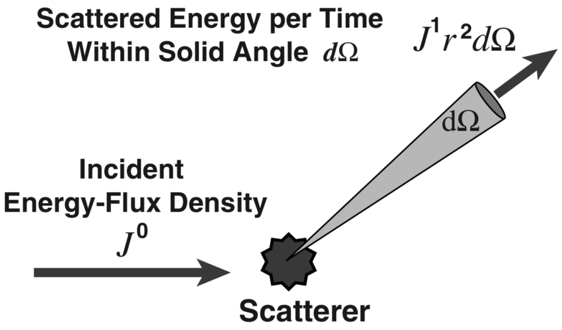

Figure 2.5: Concept of the differential scattering cross-section, $\frac{d\sigma}{d\Omega}$, of a single scatterer. Representing the scattering power of an individual scatterer generated per time in a solid angle ($d\Omega$) for a unit incident energy flux density (J^0). After Sato, Fehler, and Maeda (2012).

(Sato 1993; Paasschens 1997). ℓ^* is related to the scattering mean free path via the following relation:

$$\ell^* = \frac{\ell}{1 - \langle \cos\theta \rangle} \tag{2.4}$$

where $\langle \cos\theta \rangle$ is the directional weighted average of the cosine of the scattering angle θ. If heterogeneities scatter equal amounts of energy in all directions scattering is isotropic and $\ell^* = \ell$. If the scattering strength varies with directivity and thus $\langle \cos\theta \rangle \neq 0$, scattering is considered anisotropic.

The distance over which the energy of a wave is significantly absorbed is called the *absorption length*, ℓ_a, and defines the intrinsic attenuation coefficient $Q_i = \omega\ell_a/c$ (or in time as $Q_i = \omega\tau_a$).

2.3 Statistical description of waves and scattering media

Now we have introduced the key definitions in the field of scattering, we will continue by explaining the concept of scattering using a statistical description of the wavefield and medium.

2.3.1 Wave fluctuations and propagation regimes

Wave propagation in heterogeneous media is governed by the degree of disorder. Using a statistical approach, we can characterise the wave propagation through a random medium as contributions of wavefield u. One part of the wavefield is the coherent wave $\langle u \rangle$ (or coherent intensity $\langle I \rangle$ [1]), which is the part of the wavefield that remains after averaging over the statistical ensemble of realizations of the random heterogeneity of the medium. The coherent wave is also called the ensemble average of u. The main contribution of $\langle u \rangle$ can be found in the time window around the first arrivals. The other part of u is the incoherent wave, u_f, which contributes to all parts of the seismogram and effectively forms the coda. The incoherent mode concerns the generation of the waves that travel in a direction different to that of the incident wave. Essentially, it is the relative contributions of $\langle u \rangle$ and u_f to the total wavefield that govern the propagation regime in which the waves travel at a specific moment in time. Hence, the dominant propagation regime depends on the ratio between the physical property ℓ and propagation distance L for a certain wavelength. The $f-$subscript in u_f refers to fluctuations, since the incoherent wave is dominant

---

[1] Intensities are used in the radiative transfer model, which we use in our studies in Chapter 4 & 5. Radiative transfer theory will be introduced in Section 2.4

in strongly fluctuating regimes. This is the case when the propagation distance $L \gg \ell$, and as a result the coherent part completely extincts (Rytov, Kravtsov, and Tatarskii 1988). This regime is typically referred to as the *diffusive regime.*

In weakly fluctuating regions, where $L < \ell$, the coherent wave is dominant (Rytov, Kravtsov, and Tatarskii 1988). This can be the case in the *single scattering regime*, in which the wave interacts just once with heterogeneties in the crust. Single scattering provides a good description of the propagation characteristics at small distances from the source and at a short lapse time ($t < \tau$) from the source origin time.

Another important propagation regime is the *multiple scattering regime*, which is valid if ℓ and ℓ^* are smaller than the propagation distance. It dominates over single scattering as travel distance or lapse time increases. In the multiple scattering regime the incident wave interacts multiple times with scatterers and thus attenuates strongly.

Lastly, there is the *ballistic regime*, which is most contrasting compared to the diffusion regime. For $L \ll \ell$, there are hardly any fluctuations in the wavefield and thus the ballistic wave is dominant.

In this thesis the focus is not solely on the waves of the diffusive regime but we also analyse waves in the single and multiple scattering regime.

2.3.2 Mathematical description of random media

In the previous section we have seen that the degree of heterogeneity of a medium can be quantified by ℓ (and ℓ^*): the smaller ℓ the more heterogeneous the medium is. Since ℓ is related to σ and a, we can describe the heterogeneity of a random medium

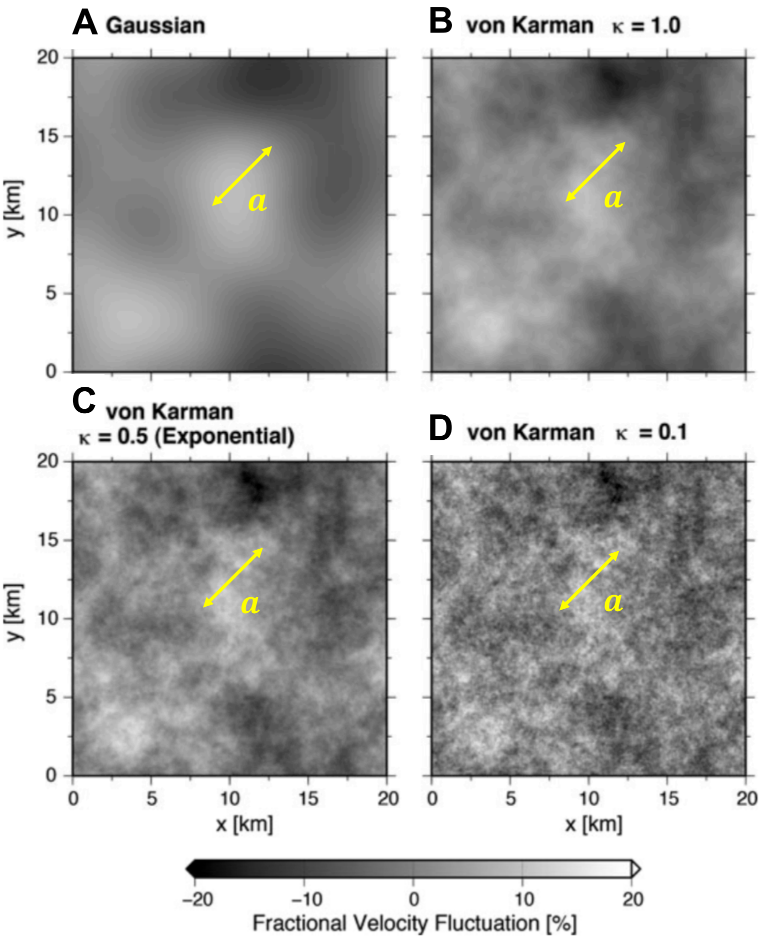

Figure 2.6: Density plots of 2-D random medium samples, where $a = 5$ km and $\epsilon = 0.05$. A) Gaussian ACF B) -D) Von Kármán ACFs. Adjusted after Sato, Fehler, and Maeda (2012).

by defining a function that is dependent on a, e.g. an auto-correlation function (ACF). For the Earth's lithosphere, the correlation length a can for example be used to define distributions of cracks and voids in the subsurface, leading to velocity changes. In this section we will show how ACFs are used to characterise a medium statistically by analysing fluctuations in the seismic velocity field.

The existence of heterogeneities in a medium manifests itself as velocity changes in seismic recordings. The velocity field can be described as a superposition of a deterministic and fluctuating part:

$$V(\mathbf{x}) = V_0 + \delta V(\mathbf{x}) = V_0[1 + \xi(\mathbf{x})] \tag{2.5}$$

where V_0 is the seismic background velocity and $\xi(\mathbf{x})$ is a random function depending on position. A mathematical tool to describe the spectral characteristics of the heterogeneities and 'roughness' of a medium is an ACF:

$$R(\mathbf{x}, \mathbf{y}) = \langle \xi(\mathbf{x})\xi(\mathbf{x} + \mathbf{y}) \rangle \tag{2.6}$$

where the angular brackets, as earlier, represent the ensemble average over multiple realisations. An ACF provides a way to describe the disorder of the medium by the power spectrum $P(m)$. The power spectral density function (PSDF) is the Fourier transform of $R(x)$ and yields the heterogeneity strength at different heterogeneity scale lengths. The standard types of ACFs to describe random media are the Gaussian and the Von Kármán ACFs, as shown in Fig. 2.6. The PSDFs of respectively the

Gaussian, $P_G(m)$, and Von Kármán, $P_{VK}(m)$, are:

$$P_G(m) = \varepsilon^2 a^3 \sqrt{\pi^3} e^{-m^2 a^2/4} \tag{2.7}$$

$$P_{VK}(m) = \frac{8\pi^{3/2}\varepsilon^2 a^3}{\left(1 + a^2 m^2\right)^{\kappa+3/2}} \frac{\Gamma\left(\kappa + \frac{3}{2}\right)}{\Gamma(\kappa)} \tag{2.8}$$

where m represents the wave number, ε^2 the variance of the fluctuation and $\Gamma(\kappa)$ the gamma function. For κ =0.5 the Von Kármán function is exponential, and therefore sometimes considered as a third type of PSDF to characterise random media. While the Gaussian ACF describes media poor in short wavelength well, the Von Kármán is the preferred ACF for media rich in short wavelength components.

Scattering causes fluctuations in both the amplitude and the phase of the wavefield, therefore we can extract information on the statistical properties of the medium by analysing their spectra. Aki (1973) was one of the first applications to obtain the fluctuation properties using an array of earthquake recordings. He analysed the wave around the ballistic window and compared the phase and amplitudes for all receivers and the fluctuations between them. With this analysis Aki (1973) estimated the correlation length, or size of the scatterers (a), and the total variance of the velocity fluctuations in Montana, USA, using the LASA array.

2.4 Seismogram envelope models

There are various methods to model seismogram envelopes in order to explain and study inhomegeneities of the Earth's lithosphere. One method is the Markov approximation, which is valid in the propagation regime where the fluctuating part of the wavefield is dominant over the coherent wavefield. The Markov approximation is based on the parabolic wave equation and describes the wave propagation for one-way only, it therefore does not include back-scattering or turning waves. A more suitable technique to describe energy propagation in scattered media is based on radiative transfer theory (RTT). Since it models intensities, there is no distinction of the wavefield into different propagation regimes. As a result this technique is suitable to model the energy transport for most propagation regimes. Therefore, RTT is also valid for weakly scattering media, where other models such as the diffusive approximation break down. The envelope modelling work in this thesis is based on the radiative transfer theory and therefore we will discuss only this model in more detail.

2.4.1 Intensity model: Radiative Transfer Theory

Initially, radiative transfer was introduced in seismology by Wu (1985) in the mid-1980s. An important tool to solve the radiative transfer equation (RTE) was the introduction of the Monte Carlo method, suggested by Gusev and Abubakirov (1987). The Monte Carlo method simulates the random walk of phonons, which change propagation direction after every step. More details about the specific Monte Carlo method used in this thesis can be found in Section 4.8 and 5.2.3. Other important developments include the introduction of energy leakage (Margerin et al. 1999), full elasticity (Margerin, Campillo, and Van Tiggelen 2000), scattering anisotropy (Margerin 2006) and coupling of surface and body waves (Maeda, Sato, and Nishimura 2008; Margerin, Bajaras, and Campillo 2019). A comprehensive overview of the development of radiative transfer in seismology can be found in Margerin (2005).

Physically, the RTE is a local statement of energy conservation in a random medium and can deal with a high number of scattering events. Mathematically though, the RTE has the form of an integro-differential equation for an angle depended energy flux commonly referred to as the *specific intensity*, denoted by $I(\mathbf{r}, \mathrm{t}, \hat{\mathbf{n}})$. It quantifies the amount of energy flowing around direction $\hat{\mathbf{n}}$, through a small surface element dS located at point $\mathbf{r}$ and at a specific time t within a defined frequency band. The *total intensity* can be obtained by integration over all directions $\hat{\mathbf{n}}$. The fluctuations of the specific intensity can be described by imagining the energy balance for a small beam of rays interacting with a cylindrical scattering medium, with surface area dS and length $c\,dt$, as shown in Fig. 2.7. Energy losses and energy gains contribute to these variations. A decrease of energy is related to (i) absorption, when elastic energy is converted to anelastic energy, and (ii) transfer of energy into other directions. On the other hand, scattering of waves of direction $\hat{\mathbf{n}}^{'}$ towards direction $\hat{\mathbf{n}}$ can also results in an increase of energy, which is linked to the differential scattering cross-section as discussed in Section 2.2. With a certain probability, $\mathrm{p}(\hat{\mathbf{n}}, \hat{\mathbf{n}}')$, energy from direction $\hat{\mathbf{n}}^{'}$ changes direction toward the initial direction $\hat{\mathbf{n}}$.

The total effect of the difference in intensity is captured in the RTE as (Paasschens 1997):

$$\begin{aligned}\left(\frac{\partial}{\partial t} + c\,\hat{\mathbf{n}}\cdot\nabla\right) I(\mathbf{r},\hat{\mathbf{n}},t) &= -\left(\frac{1}{\tau} + \frac{1}{\tau_a}\right) I(\mathbf{r},\hat{\mathbf{n}},t) \\ &+ \frac{1}{\tau}\int_{S^{D-1}} p\left(\hat{\mathbf{n}},\hat{\mathbf{n}}'\right) I\left(\mathbf{r},\hat{\mathbf{n}}',t\right) d\hat{\mathbf{n}}' + S(\mathbf{r},\hat{\mathbf{n}},t)\end{aligned} \tag{2.9}$$

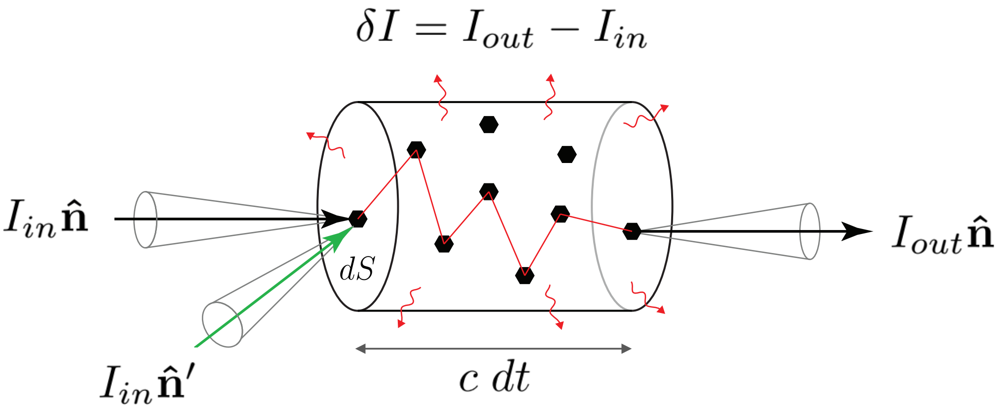

Figure 2.7: Graphical representation of Radiative Transfer Equation. A beam of initial energy flux (I_{in}) flows into the scattering medium of volume $dS \times c\,dt$ (scatterers as black hexagonals), where energy is lost (in red) due to conversion into heat and scattering into other directions. An additional beam of energy flux (green) flows into the medium from another direction, $\hat{\mathbf{n}}'$, partly adding to the energy flux coming out on the right side (I_{out}). Adapted after Mayor (2016)

where the surface integral is on the unit sphere in dimension D. Eq. (2.9) is, apart from the additional source term $S(\mathbf{r}, \hat{\mathbf{n}}, t)$, similar to what is shown in Fig. 2.7. The LHS of Eq. 2.9 describes the space-time variations of the specific intensity in the direction $\hat{\mathbf{n}}$. The first term on the RHS corresponds to the energy losses by absorption and diffusion out of direction $\hat{\mathbf{n}}$, while the second term represents the energy gain due to diffusion from all directions $\hat{\mathbf{n}}'$ to $\hat{\mathbf{n}}$. Recalling that the scattering mean free time is denoted by τ, with $\tau = \frac{\ell}{c}$. Note that the implicit dependence on the frequency has been removed from the expression for readability purposes.

In the case of isotropic scattering (when $p(\hat{\mathbf{n}}, \hat{\mathbf{n}}') = 1/S^{D-1}$) the solution for the 2D scalar version of the RTE is provided by Sato (1993) and Paasschens (1997) as:

$$I(r,t) = \frac{e^{-ct/\ell}}{2\pi r}\delta(ct-r) + \frac{1}{2\pi\ell ct}\left(1 - \frac{r^2}{t^2c^2}\right)^{-1/2} \exp\left[\ell^{-1}\left(\sqrt{c^2t^2 - r^2} - ct\right)\right]\mathcal{H}(ct-r) \tag{2.10}$$

the symbols $\delta(x)$ and $\mathscr{H}(x)$ represent, respectively, the Dirac delta function and the Heaviside step function. The distance between (virtual) source and receiver is indicated by r. The first term of Eq. (2.10) describes the direct wave contribution and is non- zero only at $t = r/c$. The second term models the diffuse energy forming the coda for $t > c/r$.

The just introduced solution of the 2D scalar version of the RTE plays a central role throughout this thesis. In Chapter 4 we use it to synthesise energy envelopes. Furthermore, the Monte Carlo simulations used in Chapter 4 and 5 are based on the solution of the 2D RTE too.

Chapter 3

Imaging and monitoring with scattered waves

Contents

In seismology one can use earthquake records to image and monitor the subsurface.

A major disadvantage of earthquakes is their distribution in time and space. Ambient noise signals on the other hand, can provide continuous recordings at every location one can place a receiver. In the first part of this chapter we briefly discuss the origin of this noise and introduce a method to reconstruct the Earth's response (Green's function) between two receiver locations by cross-correlating their continuous recordings.

Recalling from the previous chapter, coda waves are the result of wave scattering on heterogeneities in the Earth's crust. Knowledge of scattering properties provide insights into the nature of the Earth's interior and places constraints on seismic wave propagation. Therefore, the ability to separately estimate the spatial distributions of intrinsic and scattering attenuation is crucial for improving our understanding of the Earth's structure. In the second part of this chapter (Section 3.2) we discuss methods to estimate scattering properties from coda waves of earthquake records, but they can also be applied to cross-correlation functions as we will see in Chapter 4. Since coda waves sample the subsurface densely for long lapse-times, they are sensitive to small medium changes. Therefore, coda waves are ideal to monitor the dynamic evolution of the Earth's crust. The last part of this chapter (Section 3.3) therefore focuses on how the subsurface can be monitored using scattered waves of either cross-correlation functions or earthquake records.

3.1 Green's function retrieval and cross-correlations

The ambient field is omnipresent and its amplitude varies with position, time, and frequency. Nowadays, the characteristics of the noise are well studied (e.g. Stehly, Campillo, and Shapiro 2006; Friedrich, Krüger, and Klinge 1998; Nishida, Kobayashi, and Fukao 2002). The origin of the noise depends strongly on the frequency range considered (Bonnefoy-Claudet, Cotton, and Bard 2006). The spectra of the ambient noise field contain two prominent peaks, referred to as microseisms. The primary microseism has its highest amplitude with periods between about 30 and 10 s. It corresponds to the forcing of oceanic waves on seafloor topography and can generate Rayleigh and Love waves (Saito 2010). The secondary microseism peaks is generally between 5 - 7 s. It is characterized by stronger amplitudes and the suggested origin is from surface pressure oscillations, caused by the interaction between oppositely travelling components with the same frequency in the ocean wave spectrum (Longuet-Higgins 1950). Above 1 Hz the noise field is dominated by anthropogenic sources and should therefore be analysed with care (Campillo et al. 2011). More details on the physics of ambient noise generation can be found in the work by Ardhuin, Gualtieri, and Stutzmann (2019).

Ambient noise techniques are typically based on the concept that the cross-correlation between continuous recordings of two stations approximates the Green's function between those two stations. This alternative method to obtain seismograms thus minimises the dependence on earthquake occurrence and active seismic sources.

Historically speaking, helioseismology was the first field in which ambient noise cross-correlation was performed (Duvall et al. 1993; Giles et al. 1997). In the field of acoustics, Weaver and Lobkis (2001) and Lobkis and Weaver (2001) demonstrated that the Green's function can be obtained by correlating diffusive wavefields. Paul and Campillo (2001), Campillo and Paul (2003), and Shapiro and Campillo (2004) were the first to demonstrate the feasibility of Green's function retrieval from passive records in the field of seismology. However, the first interests in seismology where introduced decades earlier by studies of Aki (1957) and Claerbout (1968).

The reconstruction of the Green's function by cross-correlation can be done using records from active or passive sources. The use of active sources, like explosions, has been limited to exploration of natural resources. In general, passive reconstruction of the Green's function refers to the use of earthquake signals or ambient noise as inputs. The retrieval of the Green's function is not perfect and therefore a specific strategy should be chosen depending on the type of wave to be reconstructed. Virtual seismograms can be reconstructed from coda waves emitted by earthquakes, as demonstrated by Paul and Campillo 2001; Campillo and Paul 2003; Paul et al. 2005, for the reconstruction of surface waves, as well as for the reconstruction of coda waves (Chaput et al. 2015). Coda waves of earthquakes represent a limited amount of data. Noise records, on the contrary, are vastly available. Therefore, a strong interest in the construction of virtual seismograms from noise records has emerged. Surface waves have been extracted by correlation of noise (Shapiro and Campillo 2004; Shapiro et al. 2005; Sabra et al. 2005; Yao, Van Der Hilst, and Montagner 2010), leading to numerous applications of the method worldwide for surface wave tomography. Body waves have also been retrieved at local to global scale (Poli et al. 2012b; Poli et al. 2012a; Boué et al. 2013; Nishida 2013; Zhan et al. 2010; Roux et al. 2005).

In the following we use coda of noise correlations for monitoring purpose. The reconstruction of coda waves from noise correlation has been shown by Sens-Schönfelder and Wegler (2006), where the authors compared the decay of correlations with the decay of actual earthquakes. The nature of the correlation signals was confirmed by

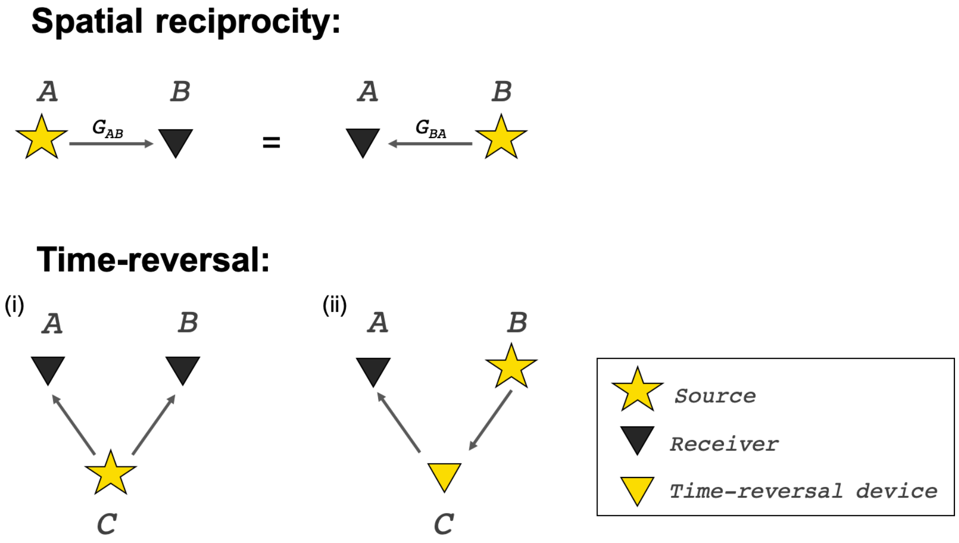

Figure 3.1: Graphical representation of two properties used for the analogy of Green's function retrieval. Upper: reciprocity theorem. Lower: Illustration of fact that there is equivalence between having a correlation at two stations from a source (i) or a source in B that emits a signal that gets time-reversed in C and later recorded at A (ii).

Stehly et al. (2008a), who re-correlated coda of correlations (commonly referred to as C3) and retrieved surface waves and even coda waves. The feasibility of coda waves retrieval is also demonstrated by Froment, Campillo, and Roux (2011) using the C3 method. For more details the reader is referred to the review studies of Campillo (2006), Gouedard et al. (2008), and Larose et al. (2006), and tutorials by Wapenaar et al. (2010a) and Wapenaar et al. (2010b).

A brief overview for the Green's function reconstruction based on the principles of spatial reciprocity and time-reversal is provided in the following, based on the heuristic approach of Derode et al. (2003b) and Derode et al. (2003a).

First, there is the concept of *spatial reciprocity* (Richards and Aki 1980), or source-receiver reciprocity. This implies that we can consider a signal emitted by a source at location A and recorded at a receiver with location B, to be identical to the signal emitted by a source at location B recorded at location A. With other words, the position of the source and receiver are interchangeable (Fig. 3.1).

Another important concept to understand the relationship between the Green's function and cross-correlations is *time reversal* (Fink 1992). In order to understand this, let us consider the acoustic wave equation:

$$\frac{\partial^2 u}{\partial t^2} = c^2 \nabla^2 u \tag{3.1}$$

with u the displacement, c the speed of acoustic waves and ∇^2 the Laplace-operator. If $u(t)$ is a solution of Eq. (3.1) (for the forward propagation), then $u(-t)$ is also a solution (for the backward propagation) because $\partial(\cdot)/\partial t^2 = \partial(\cdot)/\partial(-t)^2$.

Fig. 3.1 shows two situations (i & ii) that aid in the understanding of the analogy between cross-correlations and time reversal. In the first situation, in panel (i), we consider a source at C and two receivers at A and B. Source C emits a signal $e(t)$ for which the displacement is recorded at A and B. This recorded signal $S(t)$ is equal to the convolution of the source signal at C with the medium response, which is the Green's function, G_{AC} (G_{BC}) recorded at A (B), respectively:

$$\begin{aligned} S_A(t) &= e(t) \otimes G_{AC}(t) \\ S_B(t) &= e(t) \otimes G_{BC}(t) \end{aligned} \tag{3.2}$$

The correlation $C(\tau)$ between the signals at A and B is as follows, in the last line assuming that the source is a Dirac δ:

$$\begin{aligned} C_{AB}(\tau) &= S_A(t) \otimes S_B(-t) \\ &= e(t) \otimes G_{AC}(t) \otimes e(-t) \otimes G_{BC}(-t) \\ &= G_{AC}(t) \otimes G_{BC}(-t) \end{aligned} \tag{3.3}$$

where τ is the correlation time. The minuses for the times related to receiver B are not associated to the time reversal, they are due to the time flipping involved by the convolution process.

In the second situation, panel (ii) of Fig. 3.1, time reversal is considered. The source is now placed at location B. As demonstrated in the first part of this section $G_{CB} = G_{BC}$ due to spacial reciprocity. The receiver at location C can now be considered a time reversal device: recording a signal, reversing it in time and re-emit it. The re-emitted signal is time reversed and therefore $G_{BC}(t)$ becomes $G_{BC}(-t)$. The displacement recorded at A, caused by an impulse source at B that has been time reversed at C is therefore given by:

$$S_A(t) = G_{CA}(t) \otimes G_{BC}(-t) \tag{3.4}$$

The relation between correlation and time reversal is clear now we see that Eq. (3.3) and Eq. (3.4) are identical. Note that this result is not the same as the medium response between A and B. However, the objective is still to reconstruct G_{AB}, but to obtain this we need to consider a physical experiment. We do this by expanding the analogies on spatial reciprocity and time-reversal. Instead of a single time reversal device, we consider a full array of time-reversal devices enclosing A and B (as shown

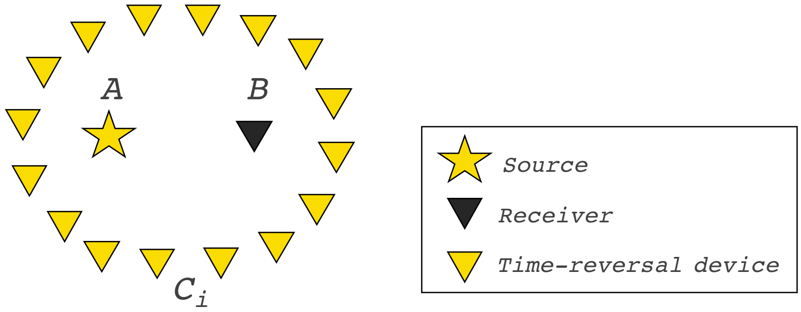

Figure 3.2: Set-up of physical experiment. A signal is emitted from location A. This signal is then received and time-reversed by the array of time-reversal devices C_i. The time-reversed signal, emitted by C_i, then focuses again at location A. The diverging and converging wavefield, from and to A, respectively, can also be recorded at B.

in Fig. 3.2).

If energy would be injected at location A as a Dirac δ, energy would propagate in all directions away from A and would be recorded at all locations C$_i$ as G_{AC_i}. Similarly to the previous experiment, the devices at C$_i$ then emit the time-reversed signals $G_{AC_i}(-t)$, which focuses again at location A. Assuming continuously distributed devices in array C$_i$ and no loss of information, the time-reversed wave that propagates back from C$_i$ focuses in A. Both the diverging and converging wavefield, from and towards A, respectively, also passes though location B and gets recorded as $G_{AB}(t)$ and $G_{AB}(-t)$, respectively. This implies that the physical time-reversal experiment is similar to the sum of the Green's functions between A and B at negative and positive time. Since the time-reversal is analogous to the cross-correlation, the relationship canbe expressed as:

$$\sum_{C_i} G_{AC_i}(t) \otimes G_{C_iB}(-t) = G_{AB}(t) + G_{AB}(-t) \tag{3.5}$$

One can thus derive a proxy for the Green's function between station A and B for a homogeneous medium, in case of isotropic source distribution around A and B. For highly heterogeneous media it can be shown that there is less need for an isotropic source distribution, as the scatterers act as secondary sources, causing the wavefield to lose a dominant directivity (Derode et al. 2003a; Derode et al. 2003b).

However, in practice we are often interested in reconstructing the Green's function for weakly scattering media, were the wavefield is typically not diffuse for not late lapse-times. In those cases the noise source distribution is non-isotropic, which leads to an asymmetric Green's function (Paul et al. 2005). Various techniques aid in improving the quality of the Green's functions, including but not limited to pre-processing the data before cross-correlating such as 1-bit normalization (Campillo and Paul 2003) or whitening and equalization (Bensen et al. 2007), stacking of cross-correlation functions and filtering (e.g. Baig, Campillo, and Brenguier 2009; Stehly, Cupillard, and Romanowicz 2011; Moreau et al. 2017), cross-correlation of cross-correlations known as C3 (Stehly et al. 2008a).

Now we have established that we can use ambient noise to reconstruct 'virtual seismograms' between any two stations, without knowledge of the position of the actual sources that excite the wavefield, the possibilities to study the subsurface are countless. In the next sections we will present methods to image scattering properties and monitoring medium changes by exploiting the information accumulated by coda waves, from either real earthquake records or virtual seismograms.

3.2 Imaging of scattering and absorption properties

Various methodologies have been developed to image scattering properties of the Earth's lithosphere. Researchers have been able to separate the contribution of seismic scattering and absorption, and later even map their spatial variations to aid in the interpretation of main geological features.

One approach to describe medium heterogeneities is to extract a deterministic description from a seismic velocity tomography model. As explained in Section 2.3.2, medium fluctuations can be described by its ACF or PSDF. Estimating the ACF parameters of a velocity model could therefore be used to provide a deterministic image of the scattering properties (e.g. Nakata and Beroza 2015). The main drawback of this indirect method to characterise a medium is however, that it is difficult to differentiate between the actual medium properties and the imprint of the tomography strategy. First, the resolution of the velocity model is governed by the Fresnel zone, the path and wavelength amongst other factors. Furthermore, during the inversion process itself smoothing or damping is applied, which directly affects the variance of the fluctuations and the correlation length. Hence, even though it may be an interesting approach one needs to be aware of the biases it imposes on the solution.

Many studies have separately estimated intrinsic and scattering attenuation by fitting observed envelopes to theoretical ones based on radiative transfer theory (e.g. Padhy, Wegler, and Korn 2007; Jing, Zeng, and Lin 2014; Wang and Shearer 2017; Calvet and Margerin 2013; Margerin and Nolet 2003). An extension of this approach is the 'Q-open' method of Eulenfeld and Wegler (2016), where not only the attenuation parameters but also the source and site amplification terms are estimated. By applying Q-open to the USarray network and interpolation, Eulenfeld and Wegler (2017a) derived the 2-D distribution of scattering properties in the United States. Recently, Izgi et al. (2020) examined the 2-D variations of frequency-dependent scattering parameters in the North Anatolian Fault zone (NAFZ), utilising 249 earthquake records. The authors employed procedures presented by Sens-Schönfelder and Wegler (2006) (for the inversion) and Eulenfeld and Wegler (2017a) (for the interpolation) to obtain the spatial distribution of scattering properties by fitting earthquake envelopes, assigning them to station locations and then averaging and interpolation them. Izgi et al. (2020) study exactly the same region of the NAFZ as we do in Chapter 4. It is therefore interesting to compare results for the lowest frequency (0.75 Hz) with our results derived from ambient noise cross-correlations in the frequency band 0.1-0.5 Hz. The resulting map of Izgi et al. (2020) is shown in Fig. 3.3. A detailed comparison between these results and our findings is made in Chapter 4.

A new approach for imaging spatial variability of the attenuation parameters, however, is the use of sensitivity kernels for the scalar case (Ogiso 2019). So far, most studies applied a from of regionalisation, or station interpolation, to obtain the spatial distribution of scattering properties. Ogiso (2019) conducted a 3-D attenuation tomography strategy based on time-dependent sensitivity kernels for the full envelope in an application to the southwestern part of Japan. The authors' approach is divided into two steps: first, both intrinsic and scattering attenuation parameters, but also source and site amplification factors, are estimated for each earthquake by an envelope-fitting method (Eulenfeld and Wegler 2016). Second,

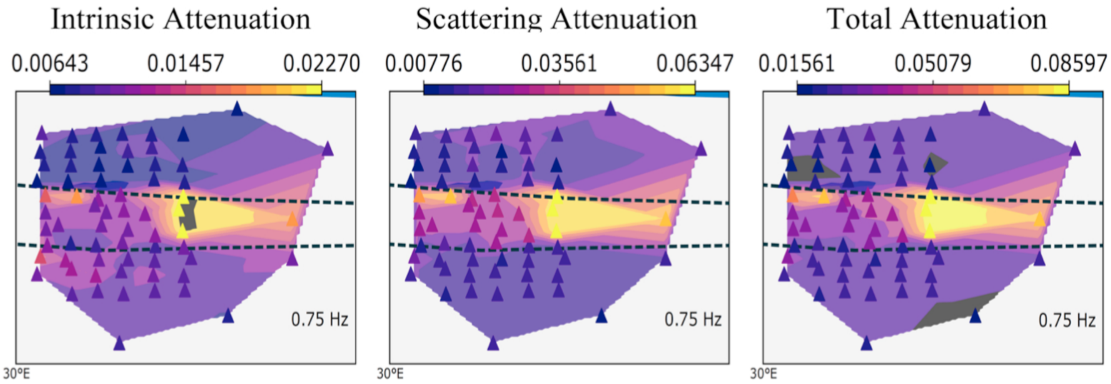

Figure 3.3: Attenuation coefficients in the eastern part of the North Anatolian Fault Zone, in the vicinity of Izmit. The 2-D variation of inverse intrinsic attenuation coefficient Q_i^{-1} (left), inverse scattering coefficient Q_{sc}^{-1} (middle) and inverse total attenuation coefficient Q_t^{-1} (right) are represented for the frequency band with a central frequency of 0.75 Hz. Purplish colours mean weaker attenuation while yellowish colours indicate stronger attenuation. Triangles show the station locations. Attenuation values between stations are interpolated. After Izgi et al. (2020).

those attenuation parameters are mapped in 3-D using sensitivity kernels based on Monte Carlo simulations proposed by (Takeuchi 2016). To reduce computational cost, the sensitivity kernels are calculated in a sequential manner for each earthquake separately. Utilizing sensitivity kernels to retrieve a more accurate 3-D spatial distribution of scattering properties is a promising next step in the field of imaging with coda waves. Note that in step one Ogiso (2019) employed an envelope-fitting procedure to estimate Q_i and Q_s separately, but one could also chose another method, such as the multiple lapse-time window analysis (MLTWA; Fehler et al. (1992) and Hoshiba (1993)) method.

The MLTWA is a widely-used technique to distinguish between the contribution of scattering and intrinsic absorption. In this method one estimates the best fitting scattering parameters by modelling the spatio-temporal distribution of energy densities using RTT. In an application to the North Anatolian Fault zone we chose to utilize the MLTWA to estimate ℓ and Q_i from ambient noise cross-correlations. Therefore, we outline the main principles of the MLTWA technique in more detail in the following section.

3.2.1 MLTWA

The *multiple lapse-time window analysis* is based on the observation that the time integrals of energy density in several time windows are affected by the relative amounts of scattering and intrinsic attenuation. The foundation of the MLTWA originates from the work of Wu and Aki (1985). The author calculated a suite of curves for various values of medium parameters in the case of isotropic scattering, for which he showed the relation between the integrated energy density with source-receiver distance. The method, based on radiative transfer theory, allowed to discriminate the relative contributions of scattering and intrinsic attenuation from the total attenuation. Later, Fehler et al. (1992) improved the method by combining it with a modelling approach of Hoshiba, Sato, and Fehler (1991) in an application of earthquake recordings of the Kanto-Tokai region in Japan. The seismograms were divided into three time windows, in which the integrated energy density was calculated and plotted against source-receiver distance. The name multiple lapse time window analysis comes from this splitting of recordings into multiple finite windows (Fehler et al. 1992). The obtained energies were corrected for geometrical spreading, site amplification and source effects. Thanks to the development of time-domain solutions to the radiative transfer theory those observed energy densities could be compared to models obtained by Monte Carlo simulations (Hoshiba, Sato, and Fehler 1991) to derive the parameters for B_0 and g, where B_0 represents seismic albedo.

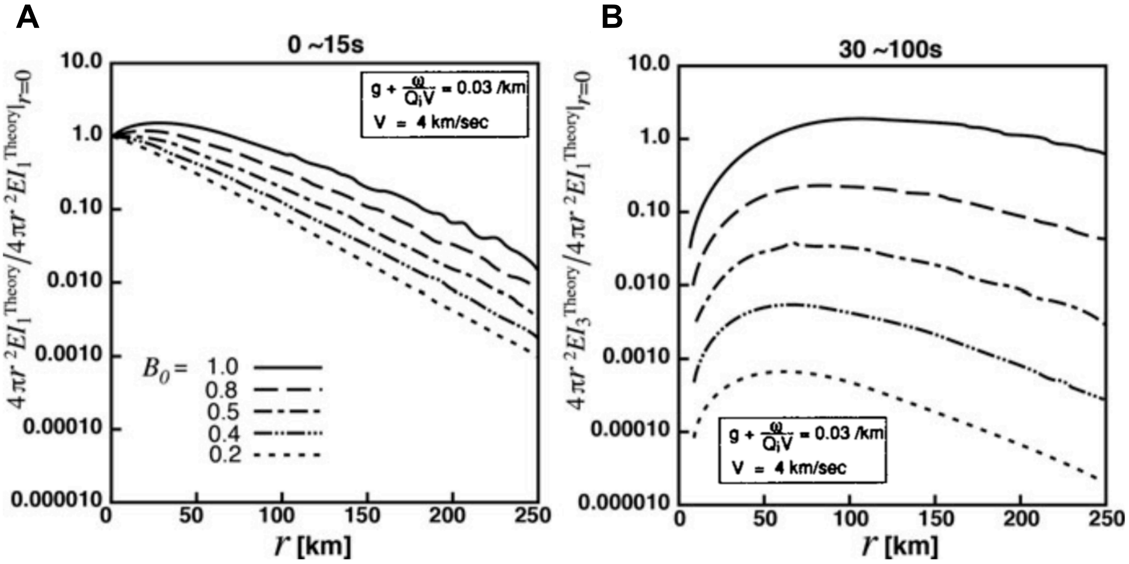

Figure 3.4: Integrated energy density corrected for geometrical spreading, relative to that at $r = 0$, versus epicentral distance for two time windows calculated with Monte Carlo simulations of the multiple isotropic scattering model. Each trave is normalised by the integral for the first time window at r=0. A) Result when energy is integrated in time window 0-15 s. B) Result when energy is integrated in time window 30- 100 s. After Fehler et al. (1992).

Seismic albedo, ranging from 0 to 1, is defined as the ratio of scattering attenuation to total attenuation (Wu 1985):

$$B_0 \equiv \frac{Q_s^{-1}}{Q_s^{-1} + Q_i^{-1}}$$

Media with strong scattering due to heterogeneity and no-intrinsic absorption have albedo close to one, and homogeneous media have zero seismic albedo. Integrated energy densities calculated from Monte Carlo simulations for various values of seismic albedo are shown in Fig. 3.4. Fig. 3.4A demonstrates that when seismic albedo is small, indicating a dominance of intrinsic attenuation, the relation between the log of the integrated energy densities with distance is near linear for the first time-window. For the later time window (panel B), the curves with small seismic albedo have low amplitude compared to the earlier time window. Hence, little scattering and thus small amounts of energy in the coda. Analysing the ratio between the running mean energy intensities of the different time windows Fehler et al. (1992) observed that the ratio between the early and late window is dominated by the amount of scattering. Note that the running mean refers to the average over a 15 km window. Another important observation from their study was that the slope of the running mean energy intensities of the first window is dominated by the total amount of attenuation.

Hoshiba (1993) expanded the MLTWA technique from a multi-station approach to an approach that can use data from only one single station to create three curves. For each earthquake at each station he calculated the energy densities and corrected for site amplification and source effects using the coda normalisation method (as described in Section 2.1). The observed energy densities were then compared with theoretical ones, which were synthesized using a multiple isotropic scattering model. Minimising the misfit between the observed and theoretical energies would then allow for extraction of the best fitting scattering properties. The main advantage of his method is the resulting spatial variability of scattering properties, because the curves are developed for individual stations separately.

A well-known application of the MLTWA is the work by Carcolé and Sato (2010). Exploiting the above described method (Hoshiba (1993)), the authors derived scattering properties over the entire Japanese region. Carcolé and Sato (2010) used 135,000 events, recorded by the three-component Hi-net stations and analysed the

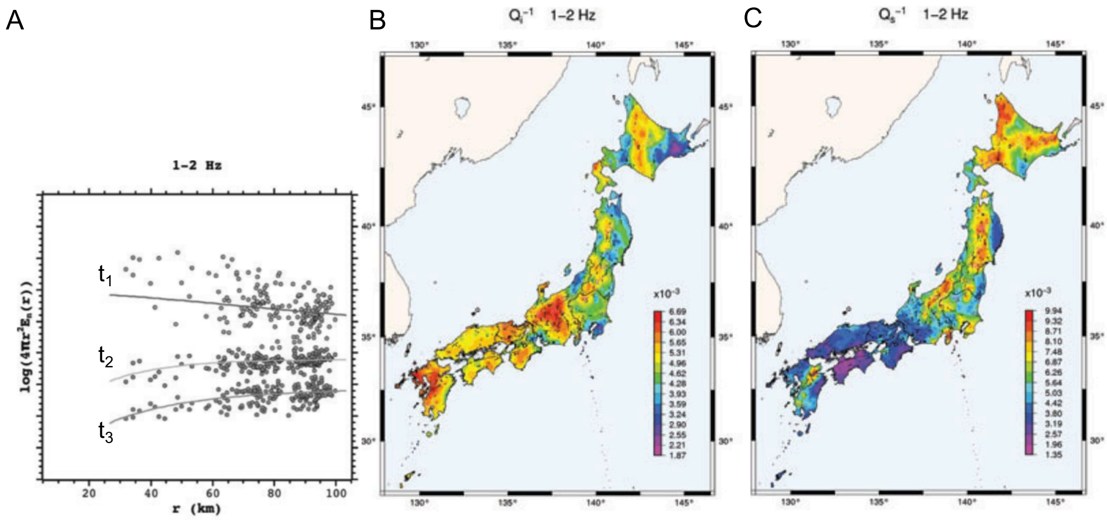

Figure 3.5: Results for MLTW analysis in Japan in the frequency band 1-2 Hz. A) Normalised energy densities versus epicentral distance for three time windows (early, mid and latest time window t_1, t_2 and t_3, respectively). B) Obtained Q_i^{-1}map. C) Obtained Q_s^{-1}map. Modified after Carcolé and Sato (2010).

energy density with epicentral distance for three 15s-time windows in the frequency bands 1-2 Hz, 2-4 Hz, 4-8 Hz, 8-16 Hz and 16-32 Hz. Reducing the misfit between the observed energy densities and the theoretical ones, which were synthesised using the analytical approximation of Sato (1993) and Paasschens (1997), they obtained the best fitting Q_i^{-1} and Q_s^{-1} per frequency band. An example of the synthetic and theoretical energies for the frequency band of 1-2 Hz are shown in Fig. 3.5 A. Panel B and C show the obtained Q_i^{-1} and Q_s^{-1} maps, respectively. The maps are obtained by averaging and interpolating the scattering properties measured at the stations.

This section has provided a brief overview on imaging scattering properties using coda waves. Realistic estimates of those properties are required for locating temporal medium changes, as they serve as input parameters for coda wave sensitivity kernels. The next section is dedicated to introduce (ambient noise) monitoring of the Earth's crust with coda waves.

3.3 Monitoring with scattered waves

The state of the Earth's crust is not static, over time the rock properties can change in response to changes in stress and migrations of fluids such as water and magma. This dynamic evolution of the subsurface includes the alteration of elastic medium properties, leading to apparent seismic velocity changes, and perturbations in the rock's heterogeneities e.g. due to opening or closing of fractures. Coda waves sample a large volume of the subsurface and are therefore sensitive to small changes of the medium they sample. Consequently, coda waves may be more suitable to characterise temporal variations of the Earth's crust than direct waves, which only sample a narrow volume along the ray path between the (virtual) source and receiver. Let us start this section by discussing methods to quantify medium changes, followed by the introduction of sensitivity kernels to locate medium changes.

3.3.1 Monitoring of apparent velocity changes

Changes in macroscopic elastic medium properties appear as velocity changes and can be observed as a travel-time delay (or phase shift) between two recordings as shown in Fig. 3.6 A. In the last two decades various techniques have been developed to capture the travel-time shifts using coda waves, which can be subdivided into four main methods. Firstly, originating from the *doublets method* of Poupinet, Ellsworth, and Frechet (1984), Brenguier et al. (2008b) and Brenguier et al. (2008a) and Clarke et al. (2011) apply the *Moving-Window Cross-Spectrum technique* (MWCS) to noise cross-correlation functions (CCF). Snieder et al. (2002) verified the mathematics of the doublet method and named it ‘coda waveform interferometry’ (CWI). It is a frequency domain measurement based on phase shifts, which I will briefly explain in the following. One of the first steps in the MWCS analysis is dividing the CCFs, both the reference and the current, into Nw smaller windows in which the delay-time measurement is performed. Then the time-delay in the jth window, δt_j, between the two CCFs can be found by a linear regression of the phase of the complex cross-spectrum, $\phi_j(f)$, with its frequency f in Hz:

$$\phi_j(f) = m \cdot f_j, \qquad\qquad m = 2\pi\delta t_j \tag{3.6}$$

Each of these δt_j is then assigned to a lapse time, corresponding to the centre of the window in which it is measured. This first linear regression is illustrated in Fig. 3.6 B. If the perturbation is due to a homogeneous change the resulting velocity perturbation, $\delta v/v$, will also be homogeneous. Consequently, the current recording appears as a stretched version of the reference recording, where the stretching is constant over time t. Poupinet, Ellsworth, and Frechet (1984) showed that in this case the following relationship holds, and we can obtain the apparent velocity perturbation via a second linear regression over the delay-times measurements (Fig. 3.6 C.):

$$\frac{\delta t}{t} = -\frac{\delta v}{v} \tag{3.7}$$

Note that if the delay-time measurements are not linear with the lapse time, one should carefully analyse the δt further as a function of lapse time to capture the heterogeneous velocity perturbation.

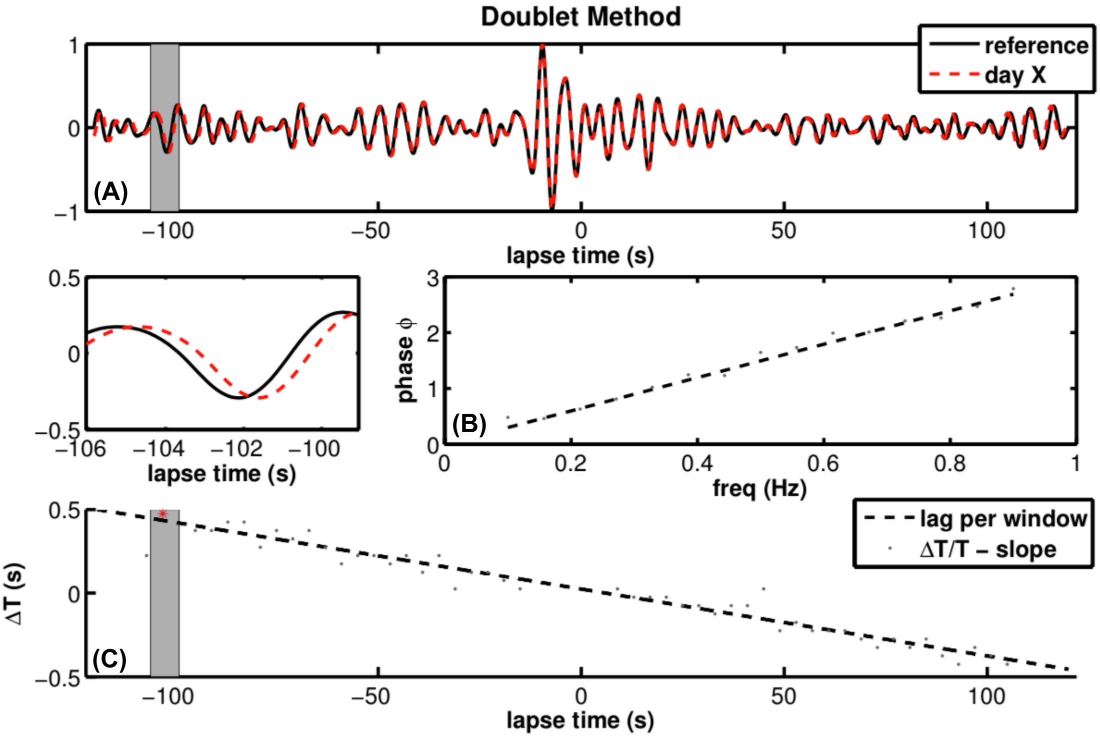

Figure 3.6: Graphical overview of the different steps in the Moving-Window Cross-Spectrum (or doublet) method. A) Reference recording (black solid line) and current recording (red dashed line). B) First linear regression in the frequency domain. C) Second linear regression over all lapse times to obtain global $\frac{dt}{t}$ measurement. After Hadziioannou (2011).

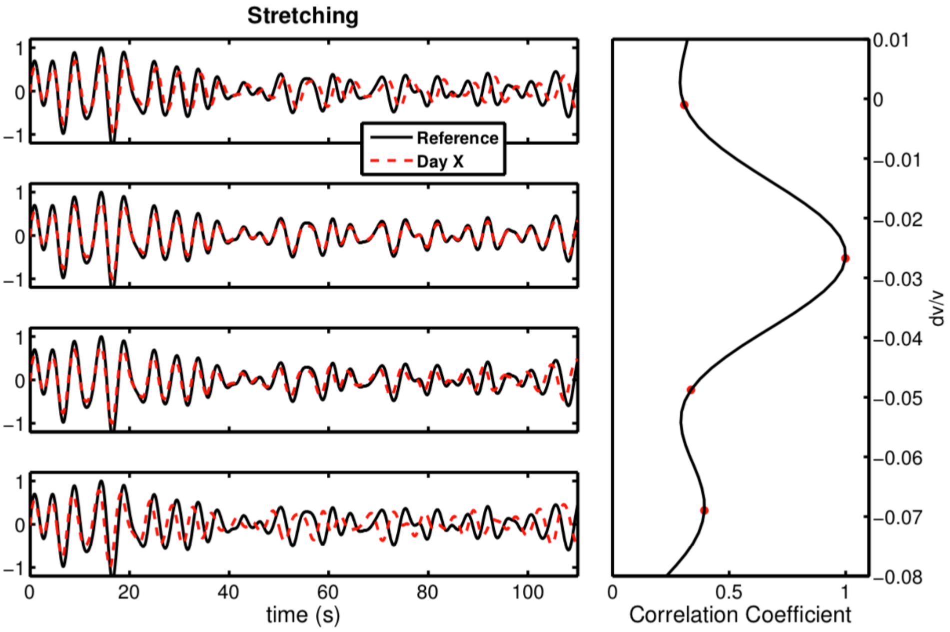

Figure 3.7: Graphical representation of the stretching method. Left: The reference (black solid line) and current (red dashed) CCFs for different stretching coefficients. Right: dv/v values corresponding to the different stretching coefficients on the left. After Hadziioannou (2011).

Another classical method is the *stretching method*, introduced by Lobkis and Weaver (2001) and Sens-Schönfelder and Wegler (2006) and shown in Fig 3.7. Contrary to the MWCS analysis, this approach is based on the waveform in time domain. It aims to derive a stretching coefficient by maximising the correlation-coefficient between the current and the reference CCF. The stretching coefficient, ϵ_{max}, is obtained by deforming the reference waveform by stretching or compressing. This method is robust in case of high level of noise in the data. Another advantage of this fast and effective approach is that is can deal with a large dv/v (Hadziioannou et al. (2009)). However, stretching does not conserve the spectrum, which could be a limitation.

Recently, Mao et al. (2020) introduced the *Wavelet Cross-Spectrum Analysis*

(WCSA) method. Based on the continuous wavelet transform, this approach provides the highest resolution in both time and frequency. This strategy is especially powerful if one is interested in the velocity changes in multiple frequency bands, and therefore with different depths. The WCSA needs a ‘mother wavelet’ to work properly, and choosing the correct one is delicate. First, the shape of the mother wavelet needs to correspond to the character of the signal. Furthermore, the wavelet affects the resolutions, so with the choice of the wavelet comes the trade-off between the temporal and spatial resolution.

Alternatively, there is the *dynamic time wrapping* technique, which exploits all the coda wave information. Additional to the time shift, it uses the amplitude and decoherence to estimate dv/v.

The techniques outlined above are the four main means of estimating travel time shifts between different correlation functions. These dt can then be inverted to estimate the relative difference in seismic wave velocity, dv/v, that we are after eventually. Classically, a direct linear regression is used as explained for the homogeneous medium change, Eq. (3.7). However, there are several implications with this approach, such as the incapability to account for lapse-time dependent relative delay-times and the choice of the reference recording. If the medium perturbation is localised the change is not felt by the entire coda wave, but instead differently for each lapse-time, i.e. the dt/t will not be constant over all lapse-times and thus relation (3.7) does not apply. Furthermore, the reference recording is often an arbitrary choice of either the first day’s CCF, the last day’s CCF or more commonly the stacked CCFs over the entire recording period. This is ambiguous and can result in misleading outcomes. Brenguier et al. (2014) suggests a doublet-inversion method, in order to avoid an arbitrary choice of the reference recording and to improve the precision by separately computing travel-time changes for all possible daily CCFs for each station pair. The daily velocity changes are then retrieved via a Bayesian inversion scheme. Alternatively, Taylor and Hillers (2020) proposes the Markov chain Monte Carlo (MCMC) method to invert the daily measurements. The advantage is that it produces a full probability distribution and that it does not require arbitrary smoothing for inversion stability, as is the case for inversion strategy of Brenguier et al. (2014).

3.3.2 Observations and applications of global velocity change monitoring

In the previous section we have briefly outlined the most commonly used methods for monitoring temporal velocity changes using coda wave interferometry. In the following we provide an overview about the current observations and applications to gain understanding of the complex and often simultaneous processes that cause these medium changes. The main causes of seismic wave velocity changes include static and dynamic changes in stress and strain state of the Earth due to earthquakes, both co-and post-seismic, environmental perturbations causing changes in external forces and industrial activities, such as geothermal reservoir stimulation and hydrocarbon reservoir changes.

Taking advantage of the extensive amounts of seismic data recorded over the last decades, including the deployments of temporary and permanent dense arrays (e.g. AlpArray, California Array, Dense Array for North Anatolia), noise-based monitoring has been applied at different scales and more frequently.

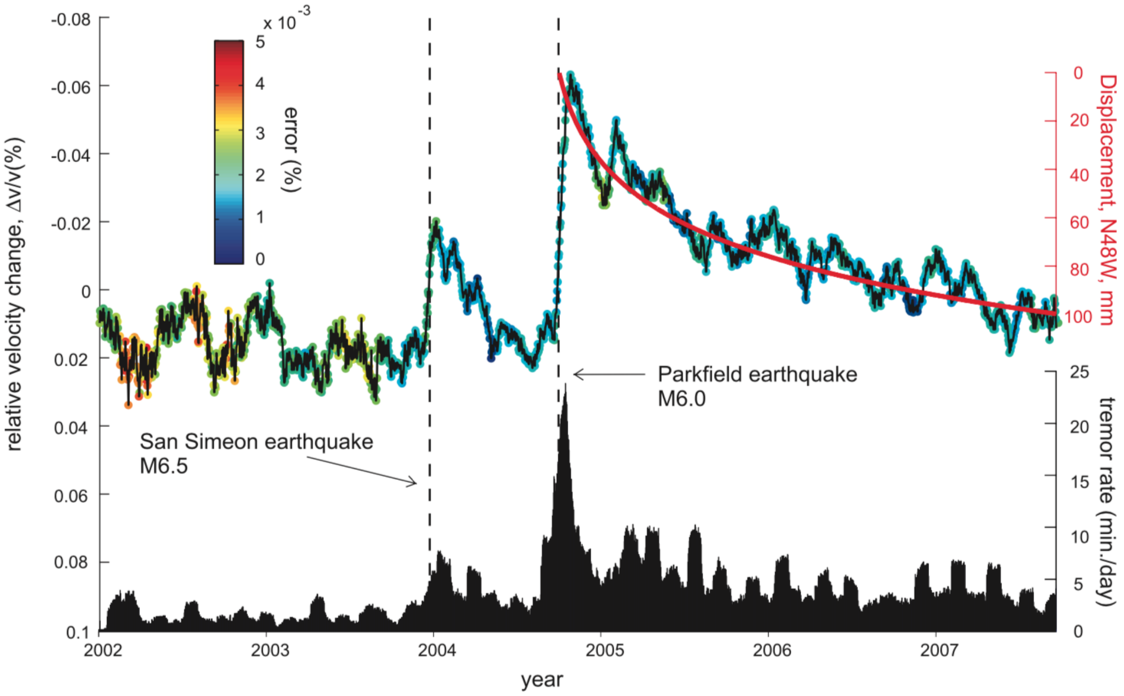

Figure 3.8: Top: Relative seismic velocity change due to Parkfield M6.0 earthquake in the San Andreas fault zone. Bottom: tremor rate as function of calendar time. Brenguier et al. (2008a)

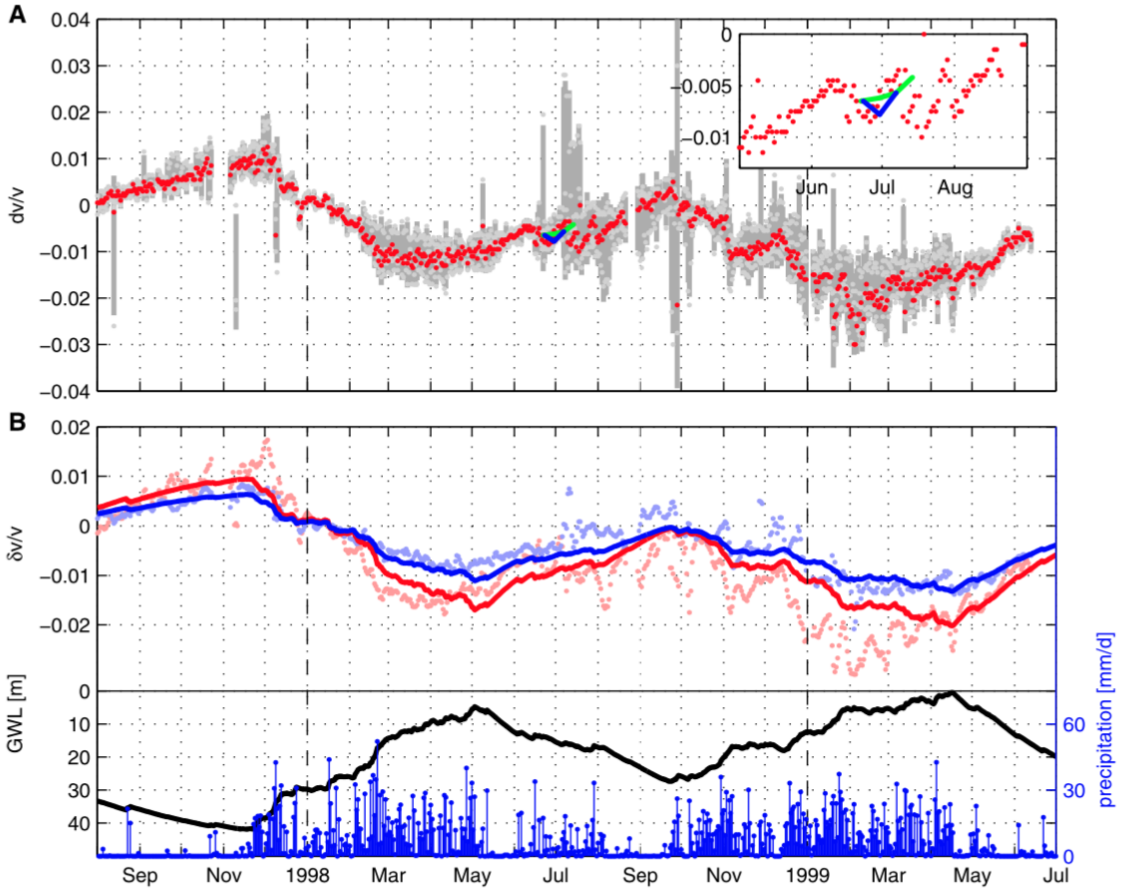

Figure 3.9: Seasonal effects observed in seismic velocity perturbations at Merapi volcano, Indonesia. A) Red dots mark the measurements in the 2–8 s time window. B) (bottom) Daily precipitation rate (blue) and modeled ground water level (black). (top) Measured (light red dots) and modeled (dark red line) velocity variations in the 2–4 s time window. Same for the 6–8 s time window in blue. After Sens-Schönfelder and Wegler (2006).

Studies of the changes in mechanical stress and strain in the subsurface due to large earthquakes can provide us with information about the processes that occur at depth. The main observations have a fast and a slow dynamical component, a sharp velocity drop at the moment of the earthquake and a slow recovery afterwards. Depending on the damage caused to the medium and the actual changes in stress, the recovery process may take from days to years and is commonly referred to as 'postseismic relaxation' (e.g. Wegler and Sens-Schönfelder 2007; Brenguier et al. 2008a; Brenguier et al. 2014; Wang et al. 2019; Poli et al. 2020). The study of Brenguier et al. (2008a) in the San Andreas fault zone found a velocity change of 0.08% due to both co-seismic damage in the shallow layers and stress changes in the deeper layers caused by the Parkfield M6.0 earthquake (Fig. 3.8. Consistent results are suggested by numerical and laboratory experiments (Lyakhovsky et al. 1997; Lyakhovsky et al. 2009; Sens-Schönfelder, Snieder, and Li 2019). This deformational aspects are often referred to as non-linear elastic and brittle behaviour. Brenguier et al. (2014) and Wang et al. (2019) analysed the velocity perturbations in Japan after the M9.0 Tohoku-Oki earthquake. Brenguier et al. (2014) link the co-seismic seismic velocity decrease of 0.08% to mechanical weakening of the pressurized crust caused by the dynamic stress associated with the seismic waves. Wang et al. (2019) interprets the short-period strong seismic velocity reductions (0.07%) as a result of the ground shaking, directly induced by the earthquake. The long-period velocity changes (0.04%) are linked to the static strain induced by the visco-elastic relaxation and afterslip in the deeper layers.

Another application of CWI monitoring is associated to volcanic setting (e.g. Anggono et al. 2012; Nishimura et al. 2005; Sens-Schönfelder and Wegler 2006;

Mordret et al. 2010; Brenguier et al. 2016; Sánchez-Pastor, Obermann, and Schimmel 2018; Mao et al. 2019; Obermann et al. 2013b). Systematic seismic velocity reduction observations can serve as volcanic eruption precursors (e.g. Brenguier et al. 2008b). Other seismic velocity changes are linked to the compression and dilatation of the magmatic reservoirs (Sens-Schönfelder, Pomponi, and Peltier (2014) and Hirose, Nakahara, and Nishimura (2017)). More recently, the ballistic-wave monitoring study of Takano et al. (2020) suggests the observed velocity changes at the Piton de la Fournaise volcano are a result of the strain complexity due to the subtle pressurization of the shallow volcanic system.

The average velocity change observed is often a combination of multiple processes of different scales and magnitudes. Apart from tectonic and volcanic processes there are other perturbations caused by external loading forces such as variations in pressure and temperature (Meier, Shapiro, and Brenguier (2010), Richter et al. (2014), and Mao et al. (2019)), rainfall (Sens-Schönfelder and Wegler (2006), Hillers, Campillo, and Ma (2014), Hillers et al. (2015a), and Wang et al. (2017)), snowfall, wind and tides (Mao et al. (2019)). The challenge is to remove those effects in order to isolate the changes related to internal processes of natural or industrial origins. Typically, these environmental effects modulate with a certain period. Fig. 3.9 shows an example of the velocity variations caused by external forces.

Insight into the effect of the poro-elasticity on the seismic wave velocity was gained by studies focusing on the rainfall and groundwater changes (e.g. Sens-Schönfelder and Wegler 2006; Meier, Shapiro, and Brenguier 2010). These works suggest that rainfall causes changes in pore pressure in the shallow crust. When the rainwater infiltrates the pore spaces the shear modulus drops, and consequently, a lower seismic velocity can be observed. The timing of this decreased velocity is delayed compared to the peak of rainfall and depends on the permeability of the rock.

Recently, developments focus on improving spatial and temporal resolution. The current minimal detectable temporal resolution when using passive noise sources is one day (Hadziioannou et al. 2011; Stehly et al. 2015) or even down to one hour (Mao et al. (2019)). This however requires good quality noise correlations with high signal-to-noise ratios, which is achievable by either the use of a dense array (Mao et al. (2019), $\sim$ 1h resolution) or stacking over long time windows (Hadziioannou et al. (2011) and Stehly et al. (2015), $\sim$ 1 day resolution).

Recently, an interest arose in using ballistic waves of noise correlations to estimate small seismic velocity changes (Brenguier et al. 2020; Takano et al. 2020; Mordret et al. 2020; Boué et al. 2013; Mordret, Shapiro, and Singh 2014; Nakata et al. 2015; Nakata et al. 2016) in order to improve spatial resolution. An important requirement for this technique is the huge amount of seismic stations ($\geq$ 100, Nakata et al. (2015)) in the form of a dense array. These are necessary to build the virtual shot-gathers used in estimating the change in apparent slowness. The main drawback of using ballistic waves, compared to coda waves, is their strong sensitivity to temporal changes in noise source distribution, which can mask physical changes in seismic properties (Weaver, Froment, and Campillo 2009; Colombi et al. 2014). Yet, this effect could be weakened by using efficient beam-forming techniques.

Another strategy to improve spatial resolution is the use of sensitivity kernels. Similarly to the developments in imaging scattering properties (Section 3.2), sensitivity kernels can be employed to gain knowledge about the spatial location of the medium changes; these will be introduced in Section 3.3.4.

3.3.3 Monitoring of structural medium changes

Amongst elastic medium changes there may be structural changes in the subsurface too. An example of a structural change, or perturbation in scattering, is the closing or opening of a fault or cavity at depth. We can observe a perturbation in scattering as a decorrelation in the recorded waveform. Let us again consider a wave that encounters a local velocity perturbation. If we quantify the delay-time between two CCFs via the stretching method described in Section 3.3.1, and correct for this by multiplying the obtained maximum correlation coefficient with the current CCFs, a small difference between the two CCFs still remains. This decorrelation in waveform, especially visible at later lapse-times, can be observed as slight changes in phase and amplitude and is caused by the wave interacting with structural changes. The decorrelation can be expressed as (e.g. Planès et al. 2014):

$$DC = 1 - C(\epsilon_{max})$$

where $C(\epsilon_{max})$ is the correlation coefficient between the two CCFs for which the stretching coefficient is maximum.

Another observation of a structural medium change is a perturbation in intensity δI. An additional scatterer can result in either higher or lower intensities (energy densities), which can be measured by analysing certain time windows of a seismic envelope. A more detailed description can be found in Chapter 5.

Having discussed how to detect medium changes, let us go a step further and see how we can solve the locations of those perturbations in order to gain more insight into the processes at depth.

3.3.4 Localising medium changes with sensitivity kernels

Application of the procedures described in Section 3.3.1 (3.3.3) allows to obtain global apparent velocity (structural) changes, respectively, which may be interesting in its own right as the observations in Section 3.3.2 demonstrated. Nonetheless, to deepen our understanding of the processes in the Earth's subsurface it is important to know where in the medium those changes occurred, especially when they are localised e.g. the opening of a crack, or fluid movements in a volcanic setting. The spatial sensitivity of the scattering waves to medium changes, however, is rather complex due to the dependence on the wavefield characteristics, the frequency and lapse-time of the observations, and the medium properties.

Geometrical regionalisation can yield a first order estimate on the spatial distribution, but a more sophisticated approach is performing an inversion using so-called sensitivity kernels. The advantage in using sensitivity kernels is that it does not rely on the approximation of $dv/v_{local} = dt/t$, which is not verified for non-uniform changes. A sensitivity kernel describes which portion of the medium has been sampled by the wave in a probabilistic manner.

Several strategies to obtain sensitivity kernels have been proposed, such as purely numerical approaches (e.g. Kanu and Snieder 2015a; Kanu and Snieder 2015b; Snieder, Duran, and Obermann 2019; Duran, Planès, and Obermann 2020) but also exact analytical solutions (e.g. Pacheco and Snieder 2005; Planès et al. 2014; Mayor, Margerin, and Calvet 2014; Margerin et al. 2016). The definition of the obtained kernels depends on the physical approximations used to derive them, e.g. one can use the diffusion model or the radiative transfer model for the propagation of energy. For both cases the Green's function will be different and thus the obtained kernel will be different. The first sensitivity kernels for coda wave interferometry have been introduced by Pacheco and Snieder (2005) for the diffusive wavefield. Shortly after, Pacheco and Snieder (2006) provided the first probabilistic kernels for the single scattering model. Both kernels are in the form of a spatio-temporal convolution of mean intensities of the coda waves. The kernels based on the diffusive approximation may be valid if the propagation time and distances are much larger than the mean free time and mean free path, respectively, and if the medium changes are not located in the vicinity of the source. These constraints hold because the diffusion approximation does not describe energy transported by the coherent wave. Consequently, it may be suitable in strong scattering media such as volcanic regions (Wegler and Lühr 2001; Wegler 2004). However, for weakly scattering media, kernels based on radiative transfer theory may be more appropriate. Recently, Mayor, Margerin, and Calvet (2014) and Margerin et al. (2016) demonstrated that knowledge of the angular distribution of the energy fluxes of coda waves is required for the accurate prediction of intensities, in order for it to be valid with an arbitrary distribution of heterogeneities and for all propagation regimes. The authors obtained this by employing a radiative transfer approach, which directly predicts intensities.

An interesting application of spatial monitoring of subsurface changes is the study by Obermann et al. (2013b) using 19 broadband stations around the active volcano Piton de la Fournaise (PdF) on Reunion Island. Using the stretching method Obermann et al. (2013b) measured the apparent velocity change and the waveform decorrelation for the period between June and December 2010, as shown in Fig. 3.10. During this period two eruptions occurred (grey periods on Fig. 3.10). To obtain spatial information on the medium changes, they used a sensitivity kernel obtained

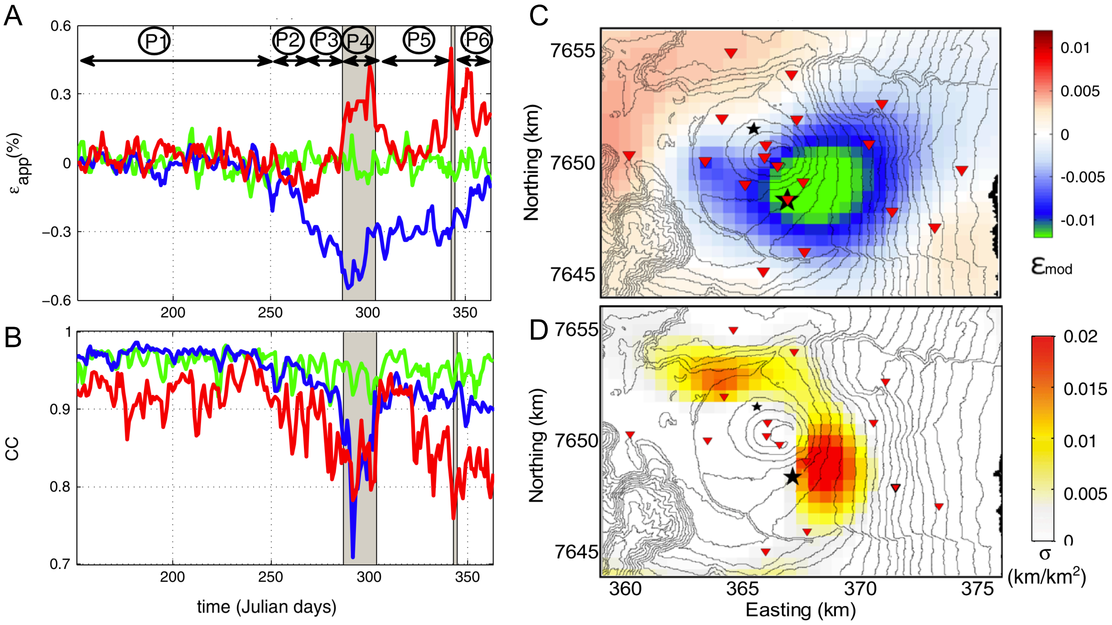

Figure 3.10: Temporal medium changes at Piton de la Fournaise on Reunion Island for June to December 2010. The three colours in panels A-B indicated three different station pairs. A) Apparent velocity change for recording period obtained by stretching method. The recording period is separated in 6 periods corresponding to different activities: P1-P6. The grey moments depict periods during with an eruption occurred. B) Correlation coefficient for recording period. C) Map with spatial distribution of mechanical medium changes during period P4. D) Scattering cross-section density map during period P1-4. After Obermann et al. (2013b).

from the diffusion approximation by Pacheco and Snieder (2005), Larose et al. (2010), and Planès et al. (2014) where the intensity propagators are based on the analytical solution of the 2D RTE (Shang and Gao 1988a; Sato 1993; Paasschens 1997). As mentioned in the previous section, knowledge about the scattering properties is necessary input for the sensitivity kernels. Instead of estimating the scattering mean free path and intrinsic absorption from the local recordings, the authors choose to use representative values derived in a similar setting by Del Pezzo, Bianco, and Saccorotti (2001) at Mount Etna in Italy. A least squares linear inversion scheme was then employed to invert for the mechanical and structural changes separately, although the same kernel was used for travel-time and decorrelation inversion. Fig. 3.10 shows the resulting maps for the mechanical (panel C) and (panel D) changes in scattering cross-section density, respectively, for the period in which the volcanic eruptions take place. Their results are in good agreement with the actual active eruptions. Furthermore, the authors demonstrated that the temporal variations are good potential precursors of volcanic eruptions at PdF.

Another application that estimates the spatial distribution of scattering perturbations at depth is by Hirose et al. (2020). Ambient noise cross-correlations from before and after the 2008 Mw 6.9 Iwate-Miyagi Nairiku earthquake in Japan are compared to estimate waveform decorrelations. Hirose et al. (2020) estimated the spatial distribution of changes in seismic scattering using a sparse inverse modelling method. The input scattering properties for the decorrelation kernel were obtained with a MLTWA (Hoshiba 1993) method as in Hirose, Nakahara, and Nishimura (2017). The authors used the kernel definition derived by Margerin et al. (2016), based on the solution of the scalar version of the RTE (Shang and Gao 1988a; Sato

1993; Paasschens 1997). Using only 5 seismic stations they found that the largest change was located south of the epicentre. The same location was retrieved using 17 seismic stations. Their proposed sparse modelling technique is promising since not all areas of interest have a high number of seismic stations operating at the same time.

Various improvements to the kernel definitions and implementations can lead to more realistic and accurate spatial sensitivities of medium changes. One important aspect is the coupling of body and surface waves to obtain sensitivities as function of depth, because scattered waves can convert back and forth between body and surface waves. Obermann et al. (2016) and Obermann et al. (2013a) showed that a linear combination of the 2-D surface wave and 3-D body wave kernels is a suitable proxy to describe the sensitivity as function of lapse-time and in depth. A formal approach to couple body and surface waves is provided by Margerin, Bajaras, and Campillo (2019). Another key development towards more realistic spatial monitoring applications is to take the distribution of scattering properties into account. This is one of the aspects we will focus on in this thesis (Chapter 5).

Most studies that apply sensitivity kernels to invert for medium changes assume uniform scattering properties. Earlier in this chapter we have seen that scattering properties are not uniformly distributed in the Earth's crust, and that they can be estimated using coda waves. Since the distribution of scattering properties plays a crucial role in the wave sensitivities, as we will see in Chapter 5, it is important to estimate the scattering mean free path and intrinsic attenuation values as input for the kernels. In the next chapter we will demonstrate that scattering properties can laterally vary with a factor of more than 10 over a short distance, in a study on the eastern part of the North Anatolian Fault zone.

Part II

Application and Simulation

Chapter 4

Laterally varying scattering properties in the North Anatolian Fault Zone

Contents

Laterally varying scattering properties in the North Anatolian Fault Zone from ambient noise cross-correlations

Chantal van Dinther[1], *Ludovic Margerin*[2], *Michel Campillo*[1]

[1] Université Grenoble Alpes, ISTerre, C.N.R.S., B.P. 53, 38041 Grenoble, France.

[2] Institut de Recherche en Astrophysique et Planétologie, Université de Toulouse III

Paul Sabatier, C.N.R.S., C.N.E.S, 14, Av. Edouard Belin, 31400 Toulouse, France.

Published in Geophysical Journal International 2020 (doi: 10.1093/gji/ggaa606)

4.1 Abstract

Intrinsic absorption and scattering properties provide us with information about the physical state and heterogeneity of the Earth's crust. These properties are usually obtained by observing the energy decay of naturally occurring earthquakes, leading to sparse spatial sampling and therefore average scattering values over a large region. The present study uses ambient noise cross-correlations to analyse the energy decay and scattering properties over a part of the North Anatolian Fault (NAF; Turkey) from the continuous records of the 73 stations of the DANA temporary array in the frequency band 0.1 - 0.5 Hz. The region covered by the stations has rapidly varying geological characteristics and is highly faulted around the northern strand of the NAF. We measured in the noise correlations the space-time evolution of the energy of the coda waves. We first perform measurements in separate sub-regions. The local scattering and attenuation properties are obtained by global optimization of a 2-D solution of the radiative transfer equation for surface waves. We found that the mean free path and attenuation coefficient are considerably varying laterally with strong scattering observed in the region lying along the northern strand of NAF. The optimization provides well-constrained values for the scattering mean free path on the order of 10 km in the fault region. The mean free path is much larger (>100 km) in the neighbouring regions. We compare our global observations with a phonon based Monte Carlo simulation of scattered energy in a laterally variable scattering model. These simulations confirm the large contrast of heterogeneity between NAF

and the surrounding crust and provide further constraints on the lateral extent of NAF. When sources are located inside the fault zone, we find a signature of the actual non-uniform scattering properties, observed as a concentration of energy in the fault zone for a limited amount of time. This in turn suggests that lateral variations of scattering properties should be taken into account in future monitoring studies.

4.2 Introduction

After the pioneering works of Aki (1969), it has been widely accepted that the coda of seismic records is composed of waves scattered by heterogeneities in the lithosphere. Aki and Chouet (1975) proposed to describe the energy decay in the coda as a combination of an algebraic and an exponential component. The latter is quantified by a frequency dependent inverse coda quality factor Q_c^{-1} (Aki and Chouet 1975) and varies with the tectonic style of the region where it is measured (Singh and Herrmann 1983). The energy decay in the coda has since then been widely used to extract empirical information on the attenuation properties of the medium (Fehler and Sato 2003). In spite of this success, it has become clear that precise information on the level of scattering cannot be obtained from the coda decay alone. Based on analytical solutions of the diffusion model in a half-space geometry, it has been proposed that Q_c^{-1} should be close to Q_i^{-1}, the intrinsic quality factor of the crust (Aki and Chouet 1975). However, Calvet and Margerin (2013) show that even in this simple geometry Q_c^{-1} and Q_i^{-1} only agree when scattering is not too strongly anisotropic and at sufficiently large lapse-time. To properly assess the statistical properties of heterogeneities, and thereby extract detailed information on the Earth's structure and composition, one needs to quantify and distinguish between absorption and scattering, both processes contributing to coda attenuation through a relation that cannot be established in general.

One phenomenological method to investigate the relationship between the observed seismogram envelopes and the spectral structure of the random heterogeneity of the Earth is based on the scalar radiative transfer equation (RTE) (e.g. Wu 1985; Wu and Aki 1988; Hoshiba 1991; Hoshiba 1993; Hoshiba 1994; Sato, Nakahara, and Ohtake 1997; Margerin, Campillo, and Tiggelen 1998). In the case of a multiple-scattering medium there are two important parameters that describe the heterogeneity: the scattering mean free path ℓ and the transport mean free path ℓ^*. ℓ, the reciprocal of the scattering coefficient, represents the average distance between two scattering events. ℓ^* is the propagation distance required for a wave to lose memory of its initial direction. The first study taking multiple scattering into account to estimate the relative contribution between scattering and intrinsic absorption was by Wu (1985). The work was based on a stationary transport equation. Later, time-dependent radiative transfer theory has been introduced to describe energy propagation in randomly inhomogeneous media (Shang and Gao 1988b; Sato 1993). The first Monte-Carlo simulations using radiative transfer for envelope synthesis were developed in parallel (e.g. Gusev and Abubakirov 1987; Abubakirov and Gusev 1990). Hoshiba, Sato, and Fehler (1991) and Fehler et al. (1992) analysed the entire S-seismogram envelopes (including the ballistic wave) to measure the ratio of scattering attenuation and intrinsic attenuation quantitatively. Their method, known as the multiple lapse-time window analysis (MLTWA), has lead to a large number of studies reporting regional values of the scattering properties (e.g. Mayeda et al. (1992) in Hawaii, Long Valley and Central California; Hoshiba (1993) in Japan; Jin et al.

(1994) in Southern California; Carcolé and Sato (2010) using the Hi-net stations in Japan; Eulenfeld and Wegler (2017b) in the contiguous United States). Sato (2019) provides a comprehensive review of transport mean free paths measurements from rock sample to lithospheric scales. The majority of the these studies use records of local earthquakes with magnitudes large enough for evaluating coda properties at large lapse times. This limits the spatial coverage and therefore provides average or regional values of scattering properties instead of more specific local values.

Ambient noise cross-correlations (e.g. Shapiro and Campillo 2004) offer an attractive alternative to study the attenuation parameters on a more local scale, particularly in the lower frequency bands ($f < 1$ Hz). From scattering theory we know that we can reconstruct the Green's function between two stations if we correlate the coda of an impulse source, such as an earthquake (Campillo and Paul 2003). Furthermore, it has been shown that we can use the coda of correlations to also reconstruct the Green's functions (Stehly et al. 2008b). This is a good indication that the coda of correlations is analogous to the earthquake coda and contains valuable information on the propagation properties.

Wegler and Sens-Schönfelder (2007) were the first to estimate the coda attenuation Q_c^{-1} from ambient noise auto-correlations in Japan. More recently, Soergel et al. (2020) mapped Q_c in the greater Alpine region using ambient noise records in the 2.5-20 s period band and found large spatial variations of coda attenuation related to the geology. Hirose, Nakahara, and Nishimura (2019) demonstrated that cross-correlations functions (CCF) can be used to derive scattering properties by comparison with active shot data. In their study they derived average scattering properties at the Sakurajima volcano in Japan by minimising the misfit between the energy densities measured in CCFs and the predictions of scalar RTE. Motivated by these recent results, we use the coda of ambient noise CCFs to detect and quantify possible lateral variations of scattering properties across the North Anatolian Fault Zone. Although the mapping of these spatial variations of attenuation across the fault is interesting in its own right, it may also have some important implications for the accurate location of velocity changes based on coda wave interferometry (CWI). Indeed, geological and geophysical studies (see e.g. Ben-Zion and Sammis 2003, for a review) suggest that the assumption of uniform scattering properties underlying most CWI tomographic studies may well break down near fault zones.

Our study area is the North Anatolian Fault Zone (NAFZ; Turkey). This is a seismically active fault zone formed where the Anatolian block and the Eurasian continent meet. The ∼1200 km long dextral strike-slip fault has an east-west orientation. The region around the Izmit rupture zone is the area we are considering in current work (see Fig. 4.1). Here the NAFZ splays into a northern and southern strand; separating the study region into the Istanbul Zone in the north, the Armutlu Block in the centre and the Sakarya Zone in the south. The Istanbul zone is dominated by marine clastic sediments and marls, overlying a crystalline basement. Another main geological feature is the Adapazari Basin, a pull-apart sedimentary basin (Şengör et al. 2005). The central block mainly comprises the Armutlu and Almacik Mountains, an accretionary complex of Cretaceous and metamorphosed sediments overlying a metamorphic basement (Yılmaz et al. 1995). In the southern part of this block, constrained by the southern strand of the NAF, one finds a small sedimentary basin that is shallower than the Adapazari basin to the north. The southernmost part of our study region is the Sakarya Terrance. It mainly consists of limestones, red

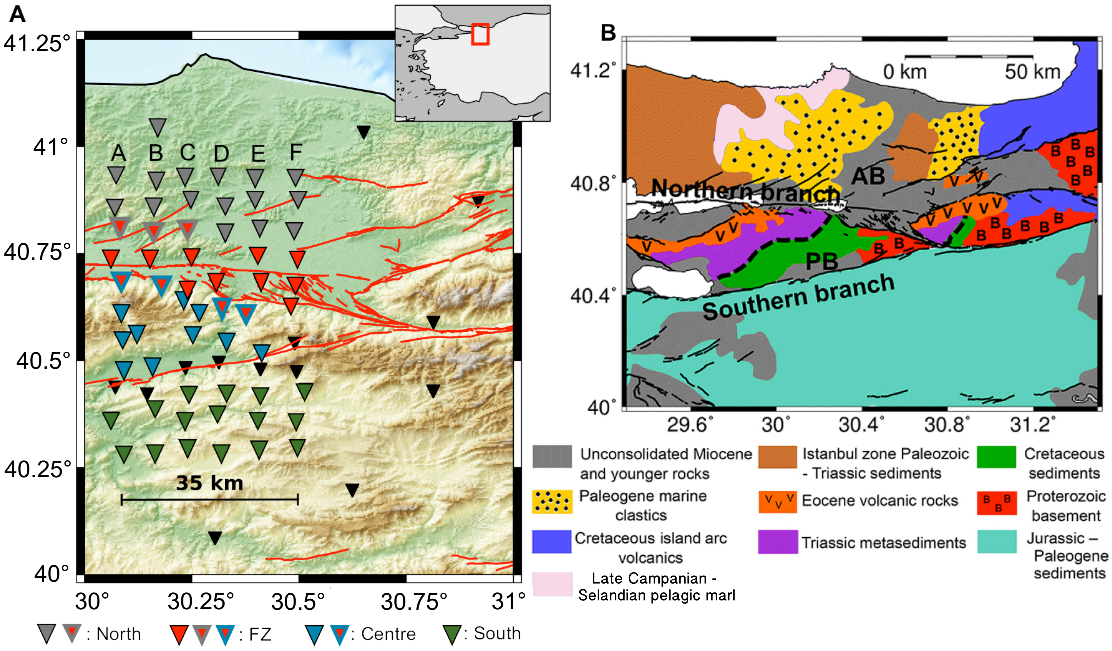

Figure 4.1: A) Map of the study region showing the DANA network (triangles) and the main faults (red; from Emre et al. (2018)). The selection of stations for the four sub-regions used in the MLTW analysis are indicated by the coloured triangles; triangles with a coloured outline belong to two sub-regions as indicated in the legend. The array is composed of 6 columns of stations, labeled A to F from west to east. Each column comprises 11 stations, numbered 1 to 11 from south to north. B) Geological map of the the wider study region (adjusted from Taylor et al. (2019) and Akbayram, Sorlien, and Okay (2016)). The Adapazari and Pamukova basin, are indicated by AB and PB, respectively.

beds and other marine sediments with some metamorphic rocks towards the southern strand of the NAF, such as serpentinite, all overlying a metamorphic basement (Yılmaz et al. 1995; Okay and Tüysüz 1999). The northern strand of the NAF will be referred to as 'fault zone' (FZ) in this study, because it has a wider faulted zone than the southern strand, due to the additional small normal faults. The complexity of the NAF has been documented by several recent seismological studies, thanks to the deployment of the Dense Array for North Anatolia (DANA 2012). Taylor, Rost, and Houseman (2016) and Taylor et al. (2019) used DANA data to provide a detailed tomographic images of seismic velocities across the fault zone. Gaebler et al. (2019) and Izgi et al. (2020) used earthquake data to infer intrinsic, scattering and total attenuation in the region. The latter study is particularly relevant to ours, because it focuses specifically on DANA data. We will therefore compare our results to the findings of Izgi et al. (2020) throughout the manuscript.

The manuscript consists of two main parts. In the first part, we estimate the spatial variation of intrinsic attenuation Q_i^{-1} and scattering mean free path ℓ from ambient noise cross-correlations (Section 4.4) using a data regionalisation approach guided by geological considerations. In the second part we validate the inferred scattering properties by direct comparison between the data and results of Monte Carlo simulations in media with laterally varying mean free path and intrinsic attenuation (Section 4.5). The next section presents the dataset and the signal processing workflow. The coda decay properties of ambient noise CCF is also briefly described.

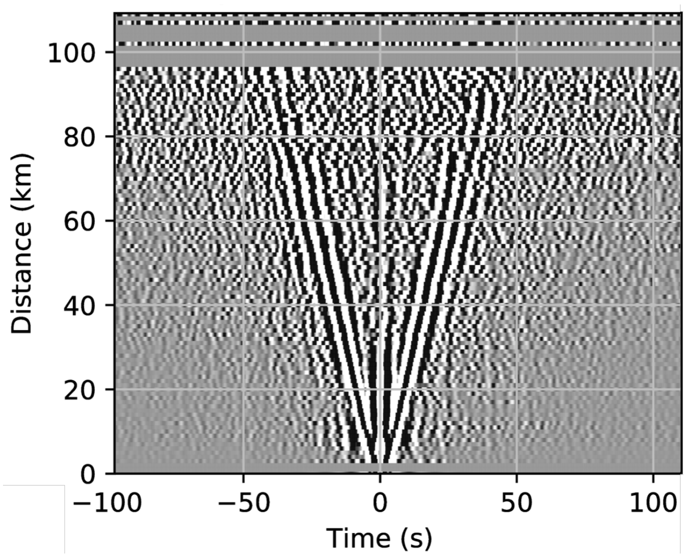

Figure 4.2: Bin-stacked cross-correlations between all pairs of North-components recorded at DANA in the 0.1-0.5 Hz frequency band. The dominant arrivals show energy propagating at velocities that are typical of surface waves.

4.3 Data processing and decay properties of coda waves

In this section, we describe the basic processing applied to the data. We show that the coda can be effectively reconstructed and perform an empirical analysis of its decay properties.

4.3.1 Data pre-processing

In this study we exploit ambient noise records from the Dense Array for North Anatolia (DANA (2012); see Figure 4.1). This array consists of 73 three-component broadband stations, 63 of which are forming a rectangle covering an area of approximately 35 by 70 km with an average inter-station distance of 7 km. The body wave reflection study by Taylor, Rost, and Houseman (2016) and the surface wave tomography by Taylor et al. (2019) provide convincing evidence that microseismic noise can be used successfully at frequencies lower than 1 Hz to reconstruct empirical Green's functions from autocorrelations and CCFs with the DANA array. To extract the direct Rayleigh wave and its coda with sufficient signal-to-noise ratio, we computed CCFs using the complete 18 months of continuous data which were recorded during the period between May 2012 and October 2013. The continuous data were first divided into one-hour segments. All components were down-sampled to 25 Hz and corrected for the instrument response before removing segments containing earthquakes of magnitude ≥ 2 as inferred from a local catalog (Poyraz et al. 2015). A spectral whitening was applied to the data between 0.01 and 1 Hz, followed by 4th-order zero-phase Butterworth filtering in the 0.1-0.5 Hz frequency band. One-bit normalisation is the last step of the pre-processing and was applied to remove any remaining transient signal. We computed the full cross-correlation tensor between all pairs of stations using 1h windows of pre-processed data. For each station pair, the results from all windows were subsequently stacked to obtain the mean CCFs over the full acquisition period.

Fig. 4.2 shows an example of the resulting CCFs for the averaged horizontal component pairs (for all 9 separate component pairs, see Fig. S1 in Supplement). From the first arrivals we derive a velocity, which is approximately equal to 2.1 km/s, indicating that the main energy pulse is most likely composed of surface waves. Henceforth, we will assume the coda to be mostly composed of scattered surface waves. For the short inter-station distances, it is hard to differentiate between Rayleigh and Love waves. This observation is confirmed by the surface wave tomography

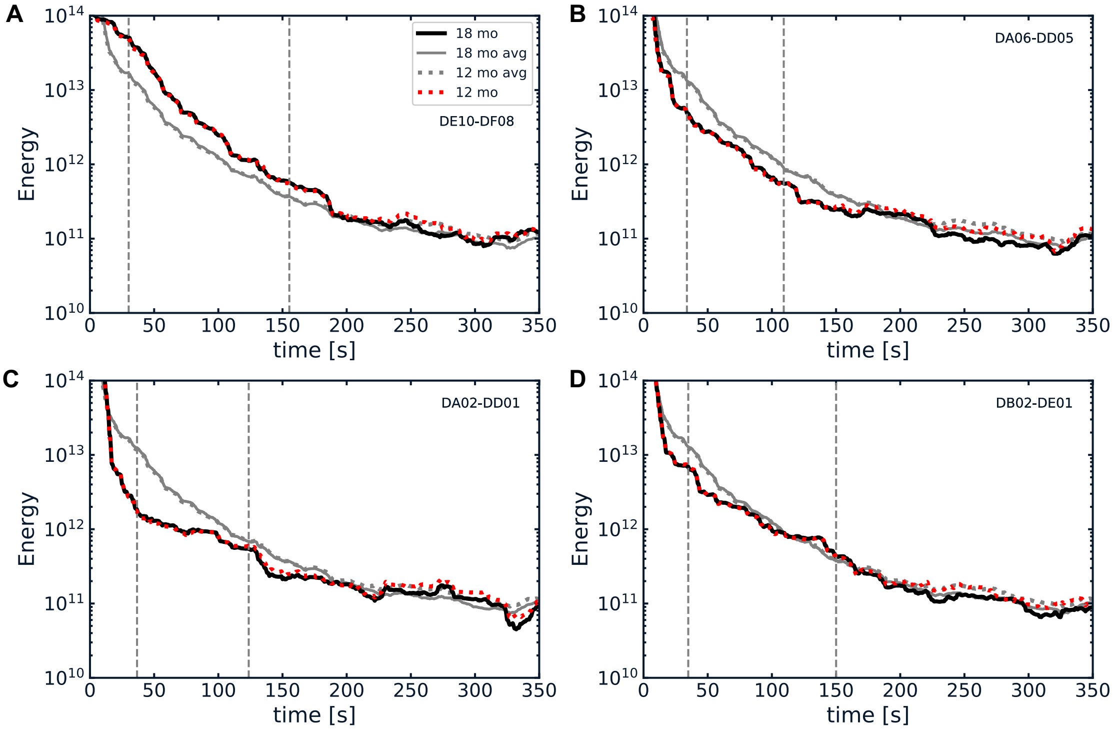

Figure 4.3: Envelopes of ambient noise cross-correlations obtained by stacking 12 months of data (red dotted line) versus 18 months of data (solid black line). As a reference, the grey solid (dashed) lines show the energy averaged over all four station pairs for 18 (12) months stacked data, respectively. The two dashed vertical grey lines show the coda window, preceded by ballistic waves and followed by noise. The four panels correspond to a representative sample of station pairs across the array; A and B show the envelopes for a station pair in the north and centre, respectively. C and D both show the envelopes for station pairs in the south.

Taylor et al. (2019), who show that the average velocities of Love and Rayleigh waves are very similar over the study area in the 0.1-0.5 Hz frequency band. To verify convergence of the calculated CCFs we compare in Fig. 4.3 the envelopes of CCFs derived from 12 months of stacked data versus 18 months of stacked data. In the coda window the differences are negligible and we are thus confident that our CCFs have converged. The later part of the envelopes however, are different, showing that the noise levels vary spatially across the study area.

4.3.2 Measurement of Coda attenuation Q_c^{-1}

A first estimate of seismic wave attenuation in the Earth's crust underneath the DANA array, for the frequency band 0.1-0.5 Hz, can be empirically obtained by measuring the energy decay of coda waves. Akinci, Taktak, and Ergintav (1994) used earthquake records in higher frequency bands to derive coda-Q in Western Anatolia. Following Aki and Chouet (1975), we assume that the energy envelopes of noise CCFs obey the same algebro-exponential decay as earthquake data:

$$E(f,t) = S(f)\ \exp[-2\pi\ t\ f\ Q_c^{-1}(f)]\ t^{-\alpha} \tag{4.1}$$

where $E(f,t)$ is the mean-squared energy envelope at lapse time t around frequency f, $S(f)$ is a frequency-dependent factor combining the virtual source magnitude and the site effect at the station and α is an exponent to be discussed below. $E(f,t)$ is obtained by applying a moving smoothing window, with a length of 16 times the central period, to the squared CCF. This smoothing is sufficient to remove rapid fluctuations of the envelope while preserving the average decay properties. To further improve the stability of the measurements, we subsequently average all four horizontal components of the energy envelopes of the cross-correlation tensor after a normalization of each term has been performed at a fixed lapse-time of 100 s. In Eq. (4.1) the exponent α is a fixed parameter that depends on both the regime of scattering (from single scattering to diffusion) and the dominant wave type in the coda (body waves or surface waves). It typically varies between 1 and 2. Assuming that the ballistic and coda waves are mostly composed of surface waves, we choose $\alpha = 1$. It is worth noting that in 2-D isotropically scattering media, the theoretical algebraic decay of energy is of the form t^{-1} in both the single-scattering and multiple-scattering regimes (Paasschens 1997). Like in previous studies (e.g. Soergel et al. 2020), we estimate Q_c^{-1} directly from the slope of the Log-Energy decay of the envelope against lapse time t with a linear least-squares method. We emphasize that the choice of α changes the absolute values of Q_c^{-1}, but does not affect the conclusion on lateral variation on Q_c^{-1}. We note, nevertheless, that the quality of the coda reconstruction is not uniform over the network. In particular, stations located in the south of the array show generally lower signal to noise ratios (SNR). To avoid underestimation of the decay rate due to noise contamination, we decided to adapt the duration of the measurement window to the quality of the CCF. The coda typically starts 25 s after the ballistic arrival and ends when the SNR drops below 5. We reject all CCFs for which (1) the coda duration is less than 75 s or (2) the correlation coefficient of the linear regression R^2 is less than 0.75. This provides us with good quality estimates of Q_c^{-1} for the relatively early part of the coda. About ∼55% of the constructed CCFs pass the selection criteria, leading to 1328 Q_c^{-1} measurements. We note that this number of Q_c^{-1} measurements is for a maximum interstation distance of 35 km (see next section for details).

4.3.3 Mapping of lateral variations of Q_c^{-1}

To facilitate the discussion of the results, the inter-station measurements of Q_c in the 0.1-0.5 Hz frequency band have been converted to 2-D maps. The study area is first discretized onto a grid of (∼8.5 km-by-12 km) pixels. At each pixel, we identify all the inter-station paths of total length smaller than 35 km that propagate through and record the corresponding values of Q_c^{-1}. We then estimate the local value of Q_c^{-1} and

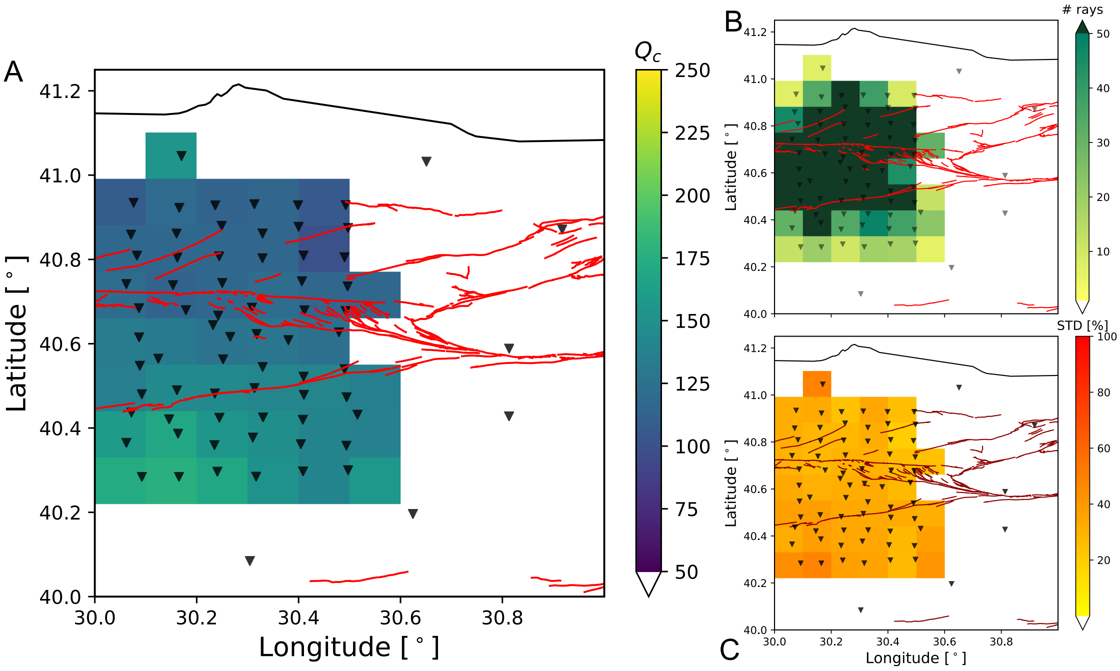

Figure 4.4: A) Q_c map derived from the causal part of the energy envelope of CCFs averaged over horizontal components. It shows the arithmetic mean of Q_c for all rays that cross the cell with a minimum of 5 rays. B) Ray coverage C) Relative standard deviation in percents.

its uncertainty by computing the arithmetic average of the recorded Q_c^{-1} values and their standard deviation. The choice of maximum path length (35 km) avoids mixing different propagation regimes and provides a fine spatial resolution. The number of interstation paths per pixel are displayed in Fig. 4.4B. There are typically more than 50 rays crossing each pixel at the centre of the array which ensures that the features shown on the map are reliable. In Supplement 2 (Fig. S3 & S4), we show that maps derived from both causal and anti-causal parts of different component combinations are very similar. Therefore, we conclude that there is no obvious bias entailed by the possible noise directivity. Fig. 4.4 illustrates that Q_c is relatively uniform over the entire study region. In particular, the fault zone does not distinguish itself from the surrounding crust. From this negative result, we may be tempted to conclude that the attenuation properties are uniform across DANA. This is not the case, however, as indicated by the direct observations of energy propagation presented below.

4.3.4 Laterally varying propagation properties

To give a direct image of the propagation properties of the region, and to detect potential local differences in properties, we have represented the energy distribution at different times deduced from the envelopes of the correlation functions. We considered virtual sources located in two very different geological contexts. The first source is located at the extreme south of the network (station DA01, Fig. 4.5A) while the second source is located in the immediate vicinity of the northern branch of the fault (station DA07, Fig. 4.5B). We measured the energy on non-normalised CCFs between these stations and all others stations of the array. The energy is averaged for all horizontal components in 8 different time windows of 30 seconds,

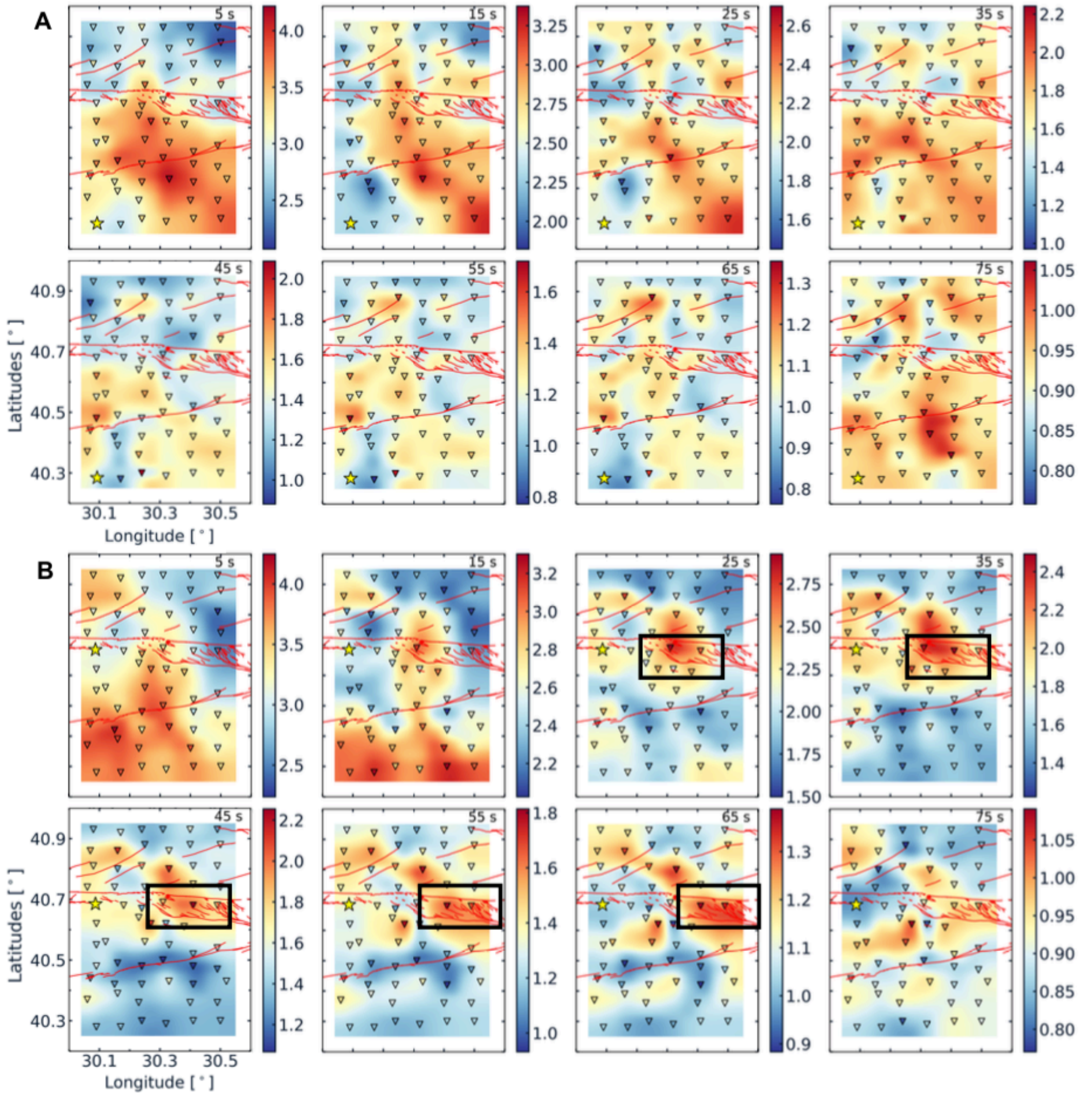

Figure 4.5: Snapshot of seismic energy distribution derived from ambient noise cross-correlations. The energy values have been normalised for display purposes only. Assuming an average coda-Q of 150 in the study area and an average frequency of 0.3 Hz, the energy per time window is multiplied by $e^{2\pi f t/Q_c}$. A) The virtual source is located in the south at station DA01. B) The virtual source station DA07 (depicted by a yellow star) is located inside the fault zone. The colour map indicates the normalised energy. The moving black box highlights the concentrated energy in the fault zone, slowly propagating towards the eastern side of the fault zone.

between 5 and 75 seconds. The energy snapshots are presented in Fig. 4.5 after temporal correction by the average Q_c . For a source south of the fault system, Fig. 4.5A does not show any spatial pattern after the initial flow of energy from the source. The energy distribution exhibits a speckle-like behaviour, without indication of any energy being concentrated at a particular location. On the contrary, when the source is close to the main fault, Fig. 4.5B shows that the energy is not spread uniformly but that it is higher inside the fault zone, especially in the eastern side, than outside the fault zone for lapse times between 25 and 65 s. The absence of such a pattern for the source in the south (Fig. 4.5A) indicates that the energy concentration observed in Fig. 4.5B along the northern strand cannot be explained by a local effect such as an amplification due to a shallow structure. One may notice that the region where we find the energy concentration is close to a kink of the main fault where intense fracturing is expected (King 1986) and observed (Fig. 4.1). A dense fracture network would result in a strong scattering strength for seismic waves. No clear energy concentration is found for the scenario with a virtual source in the vicinity of the southern branch of the fault zone. These direct observations suggest specific propagation characteristics along the northern branch that are not revealed by Q_c mapping. In the following, we rely on the MLTWA (Fehler et al. 1992; Hirose, Nakahara, and Nishimura 2019) to evaluate quantitatively the scattering and absorption properties in different sub-regions.

4.4 Mapping of attenuation properties

4.4.1 Transport model and inversion strategy

As stated in introduction, the attenuation properties of the medium as quantified by the intrinsic attenuation Q_i^{-1} and the scattering mean free path ℓ, are related to Q_c via an unknown non-linear function. Although the previous section did not reveal significant variations of coda-Q over the region, it does not imply that the scattering properties may not be variable. Since Q_c^{-1} especially relies on the assumption of a simple linear decay of the Log-Energy in the time domain, it may be insensitive to finer details of the spatio-temporal distribution of energy, particularly at small spatial scales such as shown in Fig. 4.5. To assess the possible contrasts in scattering properties between the fault and the surrounding crust, we choose to split the study area into four sub-regions where we measure the scattering properties separately. We will refer to the sub-regions as North, 'Fault Zone' (FZ), Centre and South, following a self-explanatory naming convention (see also Fig. 4.1). A similar data regionalisation was used by Izgi et al. (2020), but these authors did not distinguish between fault zone and centre. The definition of each sub-region results from a compromise between the following criteria. A sub-region should be: (1) small enough to ensure some uniformity in the geology and therefore in the scattering properties; (2) large enough so that the aperture of the sub-array enables reasonable estimates of the scattering properties as further discussed below. We note that the selected stations in each sub-region are colour-coded in Fig. 4.1. Only station pairs for which both stations belong to the same sub-region are taken into account.

To estimate the local scattering parameters we perform a MLTWA as originally

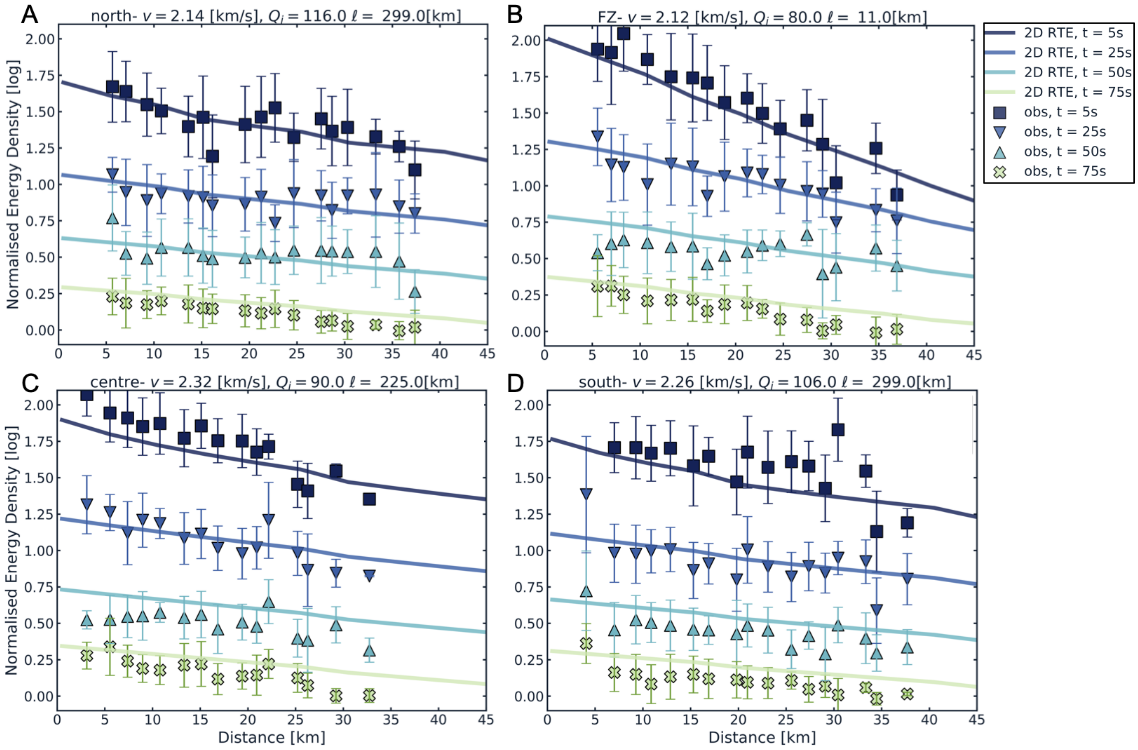

Figure 4.6: Normalised energy density (NED) in four sub-regions located inside the FZ (B) and outside the FZ (A, C, D). Individual markers show the observed NED. The lines represent the NEDs modelled by the 2-D RTE using the best fitting parameters indicated at the top of each plot. The errorbars represent ± 1 STD of the individual measurements per bin. The colours correspond to four time windows, with lighter colours for increasing lapse times (5 s, 25 s, 50 s, and 75 s after the ballistic waves).

proposed for earthquake data by Fehler et al. (1992) and recently applied to ambient noise CCFs by Hirose, Nakahara, and Nishimura (2019). In the case of the DANA data, we measure the total energy of the four horizontal components of the CC tensor in four 15-s long time windows starting at 5 s, 25 s, 50 s and 75 s after the ballistic arrival. The choice of the first time window starting at 5 s is due to high noise levels around $t=0$, which is most plausibly caused by incoming teleseimic P-waves. The energy in a late time window of 15 s duration starting at lapse-time $t=100$ s is used to normalise the measurements for the magnitude of the virtual sources and the site effects. The time window adopted for normalization purposes generally depends on the dataset. In our case, a lapse-time of 100 s has been adopted to guarantee that the SNR is high enough and the wavefield sufficiently diffuse. The observed normalised energy densities (NEDs), E_{obs}, are then averaged in 2-km-wide distance bins, in order to avoid bias towards one specific distance. The spatio-temporal distribution of NEDs in the four sub-regions is shown in Fig. 4.6. It is apparent that the spatial energy decay in the first time window is much faster inside the FZ than outside, which suggests a contrast of attenuation properties between the FZ and its environment. To confirm this interpretation, we infer the values of the scattering mean free path ℓ and the intrinsic quality factor Q_i in each sub-region by comparing the observed NEDs to the predictions of a 2-D radiative transfer equation (RTE) applied to the transport of surface waves (Sato 1993; Paasschens 1997):

$$\begin{aligned} P(r,t) = & \frac{e^{-ct/l-\omega t/Q_i}}{2\pi r}\delta(ct-r) \\ & + \frac{1}{2\pi lct}\left(1-\frac{r^2}{t^2c^2}\right)^{-1/2} \exp\left[l^{-1}(\sqrt{c^2t^2-r^2}-ct)-\omega t/Q_i\right]\mathcal{H}(ct-r) \end{aligned} \tag{4.2}$$

In Eq. (4.2), $P(r,t)$ represents the energy density at hypocentral distance r and lapse time t, for energy traveling at velocity c. The symbols $\delta(x)$ and $\mathscr{H}(x)$ represent, respectively, the Dirac delta function and the Heaviside step function. The first term on the RHS of Eq. (4.2) represents the direct wave contribution and is non- zero only at $t = r/c$. The second term models the diffuse energy forming the coda for $t > c/r$. Note that the dependence of the intrinsic quality factor Q_i and the scattering mean free path ℓ (and in turn of the energy density P) on the central frequency of the signal ($f = \omega/2\pi$) is implicit. We assume dominance of surface waves in the direct wavefield and therefore that the coda is dominated by surface wave energy, even though it is known that there is conversion of surface wave to body wave energy and vice versa in the coda (for more details we refer the interested reader to Margerin, Bajaras, and Campillo (2019)). Even though the scattering mean free path and intrinsic absorption values would be different when taking into account this mode conversion, the focus of this study is on the first order effect of the non-uniform scattering properties, thus the assumption of surface wave dominance is sufficient.

To quantify the agreement between the observed and simulated NEDs, we introduce the following misfit function, with SR as the sum of squared residuals:

$$SR = \sum_{i=1}^{4} \sum_{j=1}^{M} \left[\log \left(\frac{E_{RTE}(t_i, j)}{E_{obs}(t_i, j)} \right) \right]^2 \tag{4.3}$$

where E_{RTE} denotes the energy density predicted by the 2-D transport model and the indices i, j refer respectively to the time window and the hypocentral distance bins. Note that the same normalization procedure is applied to the observed and modeled energy densities. In Eq. (4.3) the logarithm ensures that all epicentral distances and lapse-time contribute equally to the misfit. Physically, the effect of scattering is most pronounced in the early lag times. For this reason we chose not to down-weight the SR according to the variance of the measurements in Eq. (4.3), which would be conventional in a least-square fitting approach. To find the optimal value of mean free path and intrinsic attenuation, we perform a similar grid search as in Hirose, Nakahara, and Nishimura (2019) and Fehler et al. (1992). The search range for ℓ and Q_i^{-1} is the same for all sub-regions with ℓ varying between 5 and 300 km with increments of 1 km and Q_i varying between 60 and 200 with increments of 2. Before discussing the inversion results in the next section we briefly recall why separation of scattering and absorption properties is made possible by MLTWA.

The basic ideas were presented in Fehler et al. (1992) but we may revisit their arguments in the light of the sensitivity analysis of Mayor, Margerin, and Calvet (2014) which discuss the effect of local perturbations of attenuation properties. These authors show in particular the drastically different impact of scattering vs absorption on the seismogram energy envelopes. Scattering mostly affects the amplitude of ballistic waves and the early coda. If the scattering perturbation is located on the direct ray connecting the source and station, energy is removed from the direct waves and redistributed at later time in the coda. By contrast, a perturbation of absorption has a uniform impact on the energy envelope and affects the overall rate of decay of the energy in the time domain. For more complicated scenarios (e.g. scattering perturbation located off the direct ray), we refer to Mayor, Margerin, and Calvet (2014). The fact that different time windows of the signal have quantitatively distinct sensitivities to elastic and anelastic perturbations is the key to MLTWA.

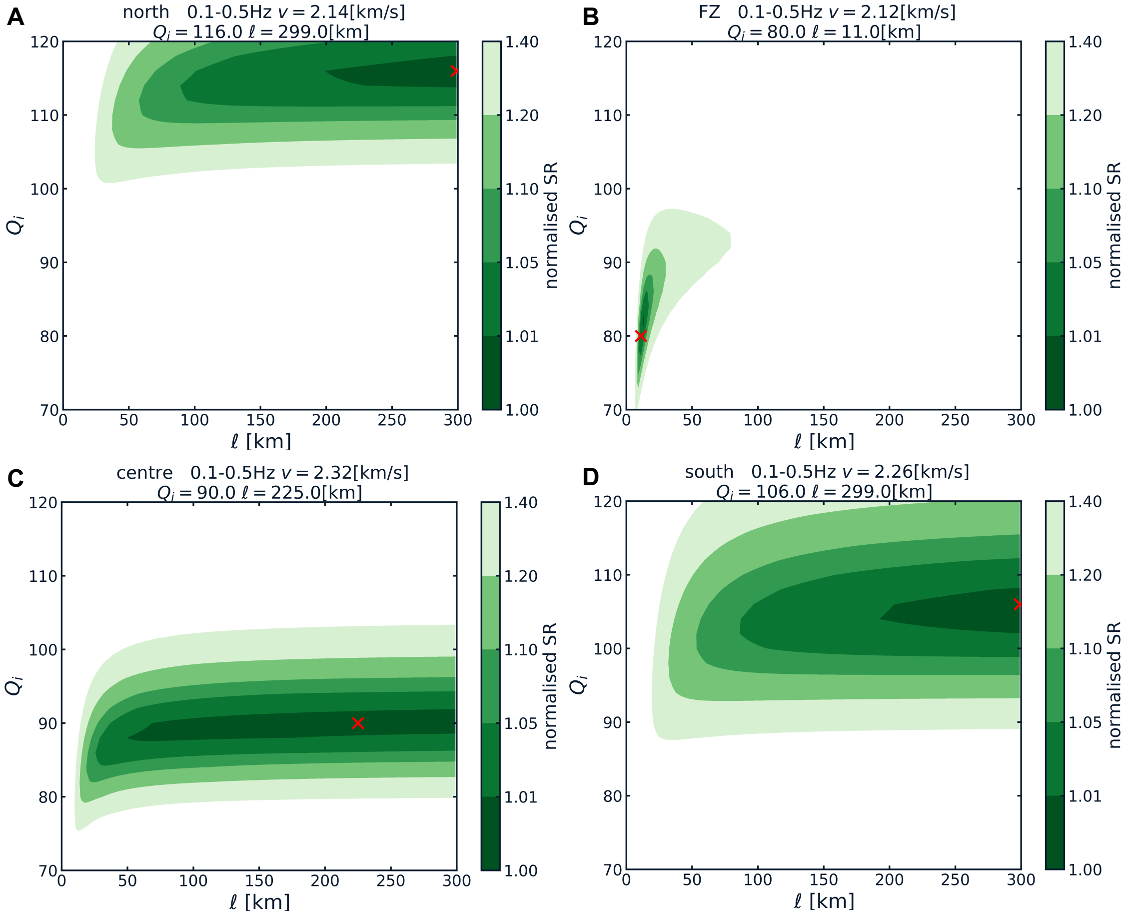

Figure 4.7: Residuals and optimal values for the grid search in the 4 sub-regions of NAF. A), C) and D) for the regions outside the FZ, north, centre and south respectively; B) for inside the FZ. The green colour indicates the values of normalised sum of the residuals (SR; as in Eq. 4.3), with the darkest colour for the smallest misfit. The values are normalised w.r.t. the minimum SR. The best fitting values are indicated by the red crosses ('X').

4.4.2 Inversion results: absorption (Q_i^{-1}) and scattering (ℓ).

Fig. 4.6 and 4.7 show the results of the optimization procedure for the scattering mean free path and the intrinsic absorption in each sub-region. The comparison of the predictions of the best-fitting model with the data indicates that a simple 2-D RTE is sufficient to capture the general spatio-temporal energy distribution across DANA, provided that different attenuation parameters and velocities are used in different sub-regions (see Fig. 4.6). From north to south, the surface wave velocity used in the simulations is 2.1 km/s, 2.1 km/s, 2.3 km/s and 2.3 km/s, as derived from the arrival time of the direct waves. We first discuss the inversion results in the FZ. We note that the level curves of the misfit function in the $\ell - Q_i$ plane shown in Fig. 4.7B indicate well-constrained values for ℓ of the order of 11 km and $Q_i \approx 80$. The most outstanding observation which is reproduced by the RTE-model is the rapid spatial energy decay inside the fault zone, mainly visible in the earliest time window of Fig. 4.6. Compared to typical values reported in the literature (Sato 2019), a scattering mean free path of the order of 10 km is rather small. Yet it is still larger than the dominant wavelength of surface waves so that localization effects (see e.g. Hu et al. 2008) are probably negligible and the use of a transport model is legitimate. This extreme value of scattering mean free path matches the value found by Izgi et al. (2020) in the northeastern part of their central zone. It is worth emphasizing that a scattering mean free path of 10 km is not common in Earth's crust. Although comparisons with earthquake data are generally not straightforward due to the difference in frequency bands, comprehensive studies by Carcolé and Sato (2010) in Japan or Eulenfeld and Wegler (2017b) in the United States suggest typically larger values of the order of 100 kms or more. The level of absorption

($Q_i \approx 80$) is also found to be rather low but not exceptional for the sub-surface of the Earth. Izgi et al. (2020) report even lower values of intrinsic absorption ($Q_i \approx 50$) from earthquake records at 0.75 Hz. For the southern strand of the NAF we also performed the inversion, but no significant difference in neither the spatial decay rate nor the resulting ℓ and Q_i were observed compared to the neighbouring central and southern sub-regions.

In the neighbouring sub-regions, Q_i is well-constrained and the best-fitting values are slightly higher than inside the fault zone with $Q_i \approx 116, 90, 106$ for the north, centre and south respectively. Izgi et al. (2020) suggest slightly larger spatial variations of Q_i at 0.75 Hz than found from ambient noise data. Our values of Q_i are generally not consistent with the estimates of Q_c, as we would have expected the reversed trend with higher Q_i values in the south than in the north. This discrepancy may again be purely a consequence of the generally more complicated envelope shape of the data than the simple parametric form of the decay underlying Q_c measurements. The misfit contours of Figure4.7 show that the mean free path is less well constrained outside the fault zone than inside. This is not surprising, as the mean free path ($\ell \geq 40$km) appears to be of the same size or larger than the largest linear dimension of the sub-network. The 20% error range indicates ℓ may range from 40 km to over 300 km (300 km is the maximum value tested) in the normal crust. These values are typical of what is found worldwide (Carcolé and Sato 2010; Eulenfeld and Wegler 2017b; Sato 2019).

4.4.3 Effect of Velocity Model and Noise

To asses the robustness of the optimization method and to better understand the poorer constraint on ℓ we explore the effect of the surface wave velocity and of the ‘noise’ in the data. In each sub-region a different velocity is used, as derived from the estimated propagation time of the first arrival. Similar to the Rayleigh wave tomography results of Taylor et al. (2019), we found the highest velocities in the centre and the lowest in the north. The actual values of the velocities, however, may be slightly different from the ones we derived via the first arrival estimate, which affects the optimization. Although marginally better fits (smaller SRs) are obtained when using lower velocities in all sub-regions, there is no significant effect on the inverted scattering properties (for more details see Supplement S9.3). Additionally, fluctuations in the NED measurements, or ‘noise’, affect the optimization and the resulting scattering properties as well. This is especially the case for zones with slow energy decay with distance in combination with a short array aperture. This aspect is also explored in greater details in Supplement S9.3. The main findings from this section are that (1) Q_i is always well resolved because Q_i controls the typical energy ratio between the different time windows and (2) ℓ may only be well resolved when the variation of the NED in the first time window is sufficiently large over the aperture array. Otherwise, the inversion can only provide a lower bound for the mean free path.

4.5 Completing the cycle: comparing observations with energy transport simulations

To better understand the physical processes that play a role in the spatial and temporal energy propagation in a medium containing non-uniformly distributed scatterers, we perform Monte-Carlo simulations of 2-D energy transport in a medium with possibly variable ℓ and Q_i. Technical details of the numerical implementation are presented in Appendix 4.8. Comparing the observations with the results from the simulations provides us with insights about the scattering process in the NAFZ.

To facilitate the discussion, we compare two types of models: i) uniform models, where the full space has the same scattering properties everywhere (further details may be found in Supplement S9.4), and ii) non-uniform models, where space is divided into four different sub-regions including a fault zone, each with different scattering properties. The motivations for this non-uniform model are as follows (1) as discussed in Section 4.4.2, the optimization is performed region by region, consequently there is no guarantee of global agreement between the data and the model, and (2) as we have observed in Fig. 4.6, the fit between the data and the model is not perfect, suggesting that there is room to improve the model of lateral variations. To maximise the ability to compare the simulations with the observations, we use the same dimensions in the simulations as in the study region.

4.5.1 Constraints on the fault zone width

Two different configurations are used for the simulations in the case of non-uniform models. The first configuration has east-west oriented receiver lines. They record

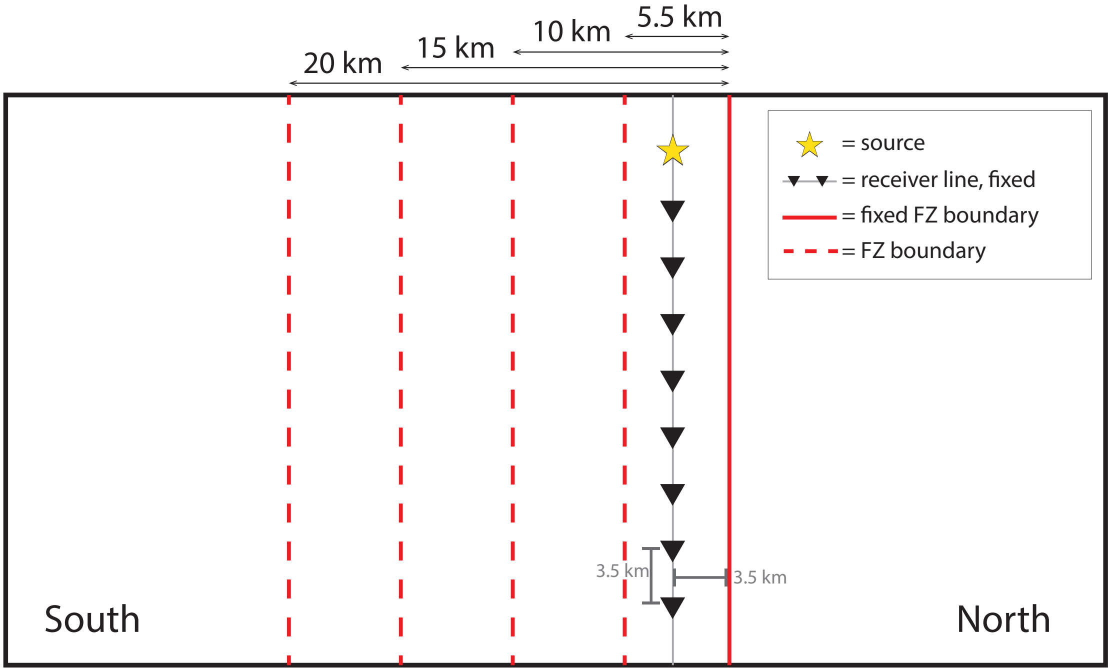

Figure 4.8: Example of the configuration for the simulations. Depending on the specific case, uniform or non-uniform, the model is divided in sub-regions where a source and an east-west receiver line is placed with receiver spacing 3.5 km. The specific configuration shown above is used for the non-uniform case with different fault zone widths. The different widths are realized by shifting the southern boundary (dashed red line). The fault zone boundary towards the north (right side) is fixed, as is the position of the receiver line w.r.t. the northern boundary and the source.

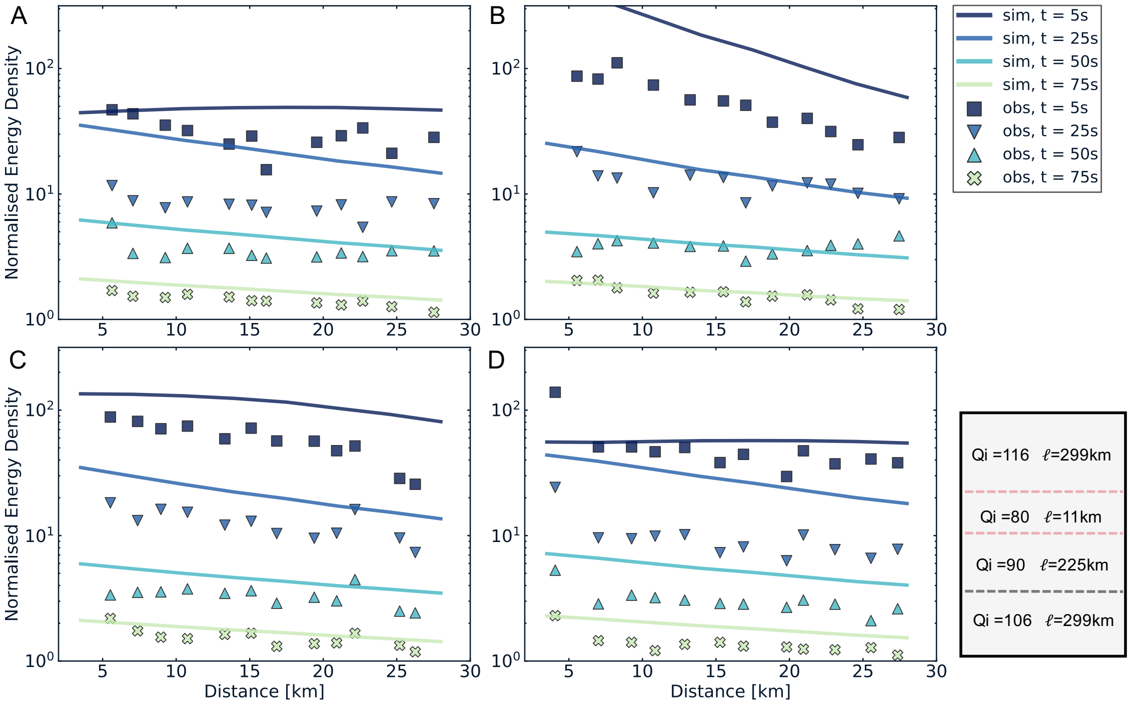

Figure 4.9: Comparison of spatio-temporal energy evolution between observations (markers) and simulations (lines) for all sub-regions: A) north, B) FZ, C) centre and D) south. The colours indicate the different 15 s-long time-windows, starting at 5 s, 25 s, 50 s and 75 s respectively. The results correspond to the initial non-uniform model, based on the scattering properties derived from the regionalisation approach and schematically shown in the lower right corner.

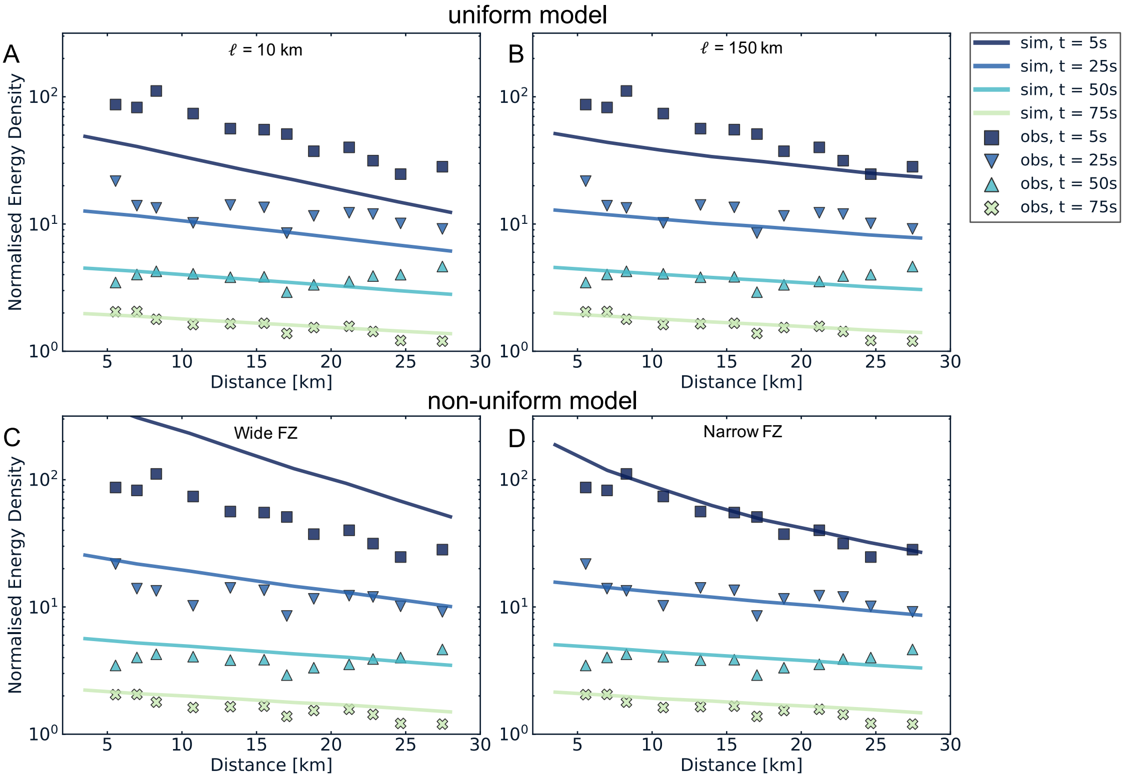

Figure 4.10: Comparison of spatio-temporal energy evolution between observations (markers) and simulations (lines) for the FZ only. The upper two panels correspond to simulations in uniform models with A) $\ell = 10$ km and $Q_i = 100$, B) $\ell = 150$ km and $Q_i = 100$. The lower two panels are for a simple model with ℓ=10 km and $Q_i = 80$ inside the FZ, and $\ell = 150$ km and $Q_i = 100$ outside the FZ. C) for a wide fault zone, of 14 km and D) for a narrow FZ of 5.5 km. The colours indicate the different 15 s wide time windows, starting at 5 s, 25 s, 50 s and 75 s respectively.

the intensities for sources excited in the corresponding sub-region. An example of this configuration is shown in Fig. 4.8. For these simulations we perform again the MLTWA and compare the results with the observations. Fig. 4.9 shows that for all sub-zones and all time windows the NEDs are greater in the simulations than in the observations, especially for the fault zone and the centre at early times. Taking simply the parameters derived in four uniform models and combining them to one non-uniform model seems insufficient to explain all observations in our study area. We note that the simulated NED for the $t = 5$ s window in the north and south appear to be constant or even increase with distance in certain epicentral distance ranges. This is related to the more complex wave propagation in a non-uniform model compared to a uniform model. One of the phenomena at work is back-scattering as shown in Fig. 4.12 and Fig. 4.13, and will be discussed in more detail in Section 4.5.3. We have seen in the previous sections that (i) we constrain ℓ inside the FZ but it proved to be more difficult outside, and (ii) there is a clear difference in the decay rate with distance between inside and outside the fault zone (Fig. 4.6). Consequently, the main focus of this section will be on explaining the observations in the fault zone. To simplify the analysis we assume uniform scattering properties outside of the fault zone from here onward (see Section S9.4 in Supplement for test on uniform Q_i).

Fig. 4.10 shows four panels with observation and simulation results inside the FZ. We first discuss the simple uniform models: panel A for a model space where Q_i =100 and $\ell = 10$ km, and panel B where Q_i =100 and $\ell = 150$ km. Both models do not match the observations to a desirable degree, especially in the first time window. For the model with strong scattering (A), the spatial energy decay in the first time window of the simulations is similar to the observations but the values themselves are too low. For the weaker scattering model (B), it seems the other way around. The decay rate with distance at early times in the simulations is too slow, but the NED values are closer to the observations. Panel C and D show results for a simple non-uniform model, with inside the FZ Q_i =80 and ℓ = 10 km, and outside the FZ uniform scattering properties for all sub-zones (Q_i =100 and ℓ = 150 km). The difference in the models between panels C and D is the width of the FZ, 14 km for (C) and 5.5 km for (D). Although the results for the wide FZ have the correct energy decay rate with distance, using a narrower zone with strong scattering yields an almost perfect match to the observations. This is in line with the findings of the tomography studies in the region (e.g. Kahraman et al. 2015; Taylor, Rost, and Houseman 2016), suggesting a fault zone that is perhaps not wider than 7 km down to the mantle.

4.5.2 The signature of a finite width scattering zone

In the case of a structure with a fault zone of material associated with high scattering taken between regions of low scattering, the energy decay with distance depends not only on the values of ℓ, as we saw in the numerical tests of the previous section, but also on the width of the FZ. Fig. 4.11 shows the simulation results for fixed values of ℓ (10 and 150 km) and varying the FZ width W. We compare the behaviour of non-uniform models with that of uniform models associated with the two values of ℓ, 10 and 150 km. Note that for the non-uniform models and the uniform model with ℓ =150 km, the energies were normalised with a 15 s long time window starting at a lapse-time of 100 s, as was done in the data analysis. A first observation is that in our time and distance configuration, the non-uniform models have very similar behaviours

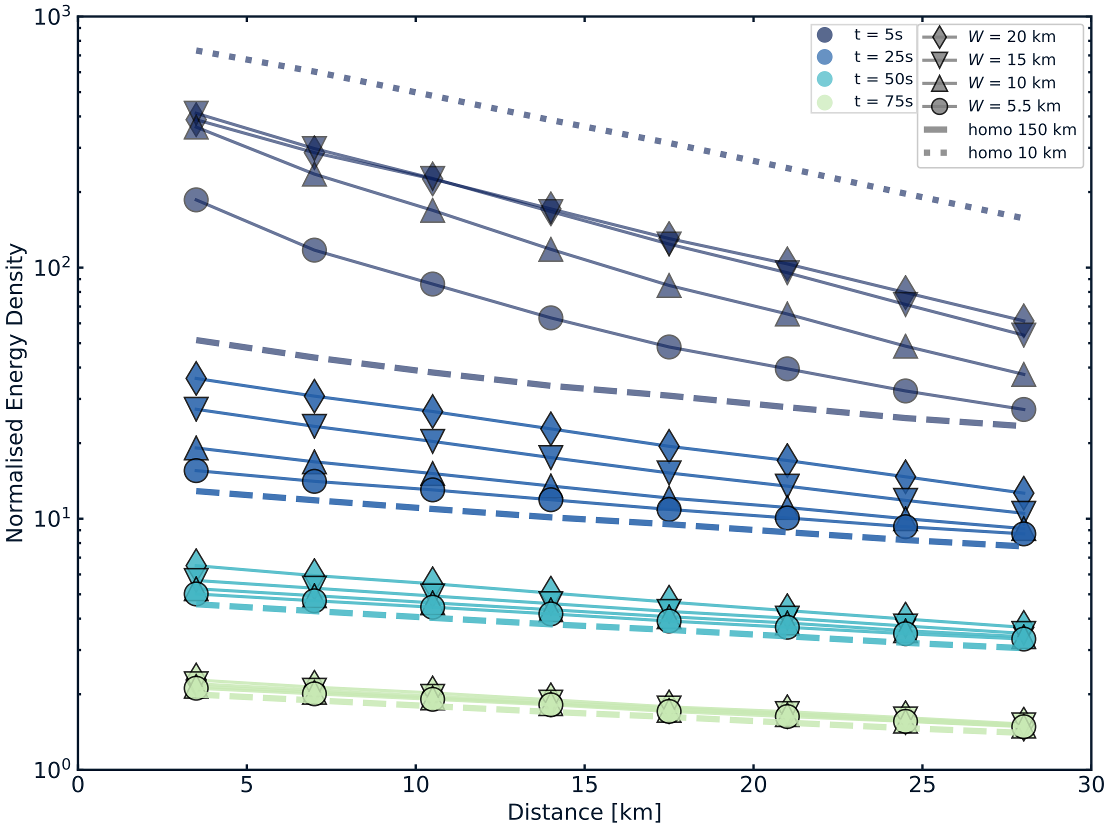

Figure 4.11: Comparison of spatio-temporal energy evolution of simulations using uniform and non-uniform models with different FZ width. The dashed and dotted lines show NEDs for uniform models with ℓ=150 and 10 km, respectively. The NEDs of the non-uniform models are indicated by the continuous lines and markers, for different widths of the fault zone, W, as indicated in the legend. The colours indicate the different 15 s wide time windows, starting at 5 s, 25 s, 50 s and 75 s respectively.

at 50 s and almost identical at 75 s. For the latter time the results are very similar to those of the uniform model with ℓ =150 km. A first simple argument to explain this observation is that the area of the strong scattering zone becomes small in comparison with the total area covered by the scattered waves (Fig. 4.8). The results presented here have been normalised at 100 s, to be consistent with the MLTWA analysis, but we have verified that the absolute long time energies for the non-uniform and uniform models with $\ell = 150$ km are close (see Fig. S30 in Supplement). Their relative difference follows approximately a scaling in W/t, deriving from the same simple geometrical argument. We thus observe a convergence towards the solution of a uniform model with ℓ =150 km for long time in all cases. These results thus indicate that it is difficult to detect a heterogeneity from the observation of temporal decreases at long times, which explains why our characterization with Q_c yielded grossly similar results inside and outside the fault zone.

The most important differences among the models are observed for the short times. Let us consider the case of the window starting 5 s after the arrival of the direct waves, which is critical in our comparison with the data. For this time window we have plotted in Fig. 4.11 in dotted line the uniform model decay with ℓ =10 km, the value in the band representing the fault zone. Contrary to the other models and the data, the energies were not normalised with the 100 s values for this uniform model. Based on our previous conclusions, the normalization was done with the values of the external uniform model (ℓ =150 km) towards which the solutions of the non-uniform models tend for long times. This normalization is carried out only for interpretation purposes, while approaching the data analysis conditions. Indeed, we know that the solutions converge towards the uniform case with ℓ =150 km, but that they show differences at finite times (see Fig. S30 in Supplement for non-normalised results). Since the FZ widths considered are small in relation to the distances travelled by the waves, and the sources are located near the FZ boundary, a significant portion of the energy escapes rapidly from the central FZ and will not be subject to intense scattering. Thus, a significant shift between the curve of the normalised ℓ=10 km uniform model and the non-uniform models is observed even at short distances. For all widths, this shift increases with distance. Remembering that the absolute time of the energy measurement increases with distance (as the lag time is added to the ballistic wave arrival time), this can be explained by the decreasing role played by the central FZ as the total surface occupied by the diffracted waves grows, leading to the convergence of the non-uniform models towards the uniform one with ℓ =150 km for long times. We note, furthermore, that all non-uniform models exhibit a decay with distance that is larger than the one of the uniform ℓ =10 km model.

Fig. 4.11 illustrates that the amplitude and decay of the normalised energies vary significantly with W. In the case where W= 5.5 km, that is smaller than ℓ in the FZ, a significant shift is observed between the uniform model ℓ = 10 km and the other models at the shortest distance. The curve exhibits first a rapid decrease with distance then approaches the curve of the uniform model ℓ = 150 km, a convergence which is observed with the curves of the longer times. The amplitude is explained by the small size of the strongly diffracting FZ (5.5 km) with respect to the radius of the region sampled by the waves. Even at the shortest distance, with the time window considered (here between 6.5 and 21.5 s), the propagation of the waves is predominantly in the low-scattering environment. Hence, the position of the source in the FZ must also be taken into account when comparing amplitudes at short distances for the different geometries.

For the other values of W, the same evolution can be observed globally. For $t =$ 5 s, the curves gradually separate to approach the asymptote at distances increasing with W. The same behaviour is observed for the other lapse-times. The evolution of the curves illustrates the transition between two limit models: strong scattering in the FZ for short times and weak for long times. Note that our configuration does not allow the first regime to be fully observed because the widths of the fault zone are small. For the windows with lapse-times larger than 5 s, the differences between the non-uniform models diminish rapidly with time or distance and the constraints on the model must be searched in a rather short time range but over a range of distances that covers the characteristic dimension/width of the scattering heterogeneity. If we consider an observation at a fixed distance, e.g. 3 km, the amplitudes for W from 10 to 20 km are very similar for $t = 5$ s (the waves sample the same part of the model), much more separated for 25 s (at different convergence stages), then again very close for larger lapse-times (close to the asymptote). This numerical example shows the need for the observation of multiple lag windows at multiple distances to decipher the global view of the energy behaviour, and also the need for a complete modelling to relate it to the model parameters ℓ and W. In particular, the effects of finite size of the diffracting FZ cannot be simply expressed by a single attenuation operator for each pair (W, ℓ) that would apply at all times.

4.5.3 Back-scattered Energy from the Fault Zone

In this section we pursue our investigation of the effects of a strong, narrow band of scattering on the energy evolution in space and time. The model we use is the

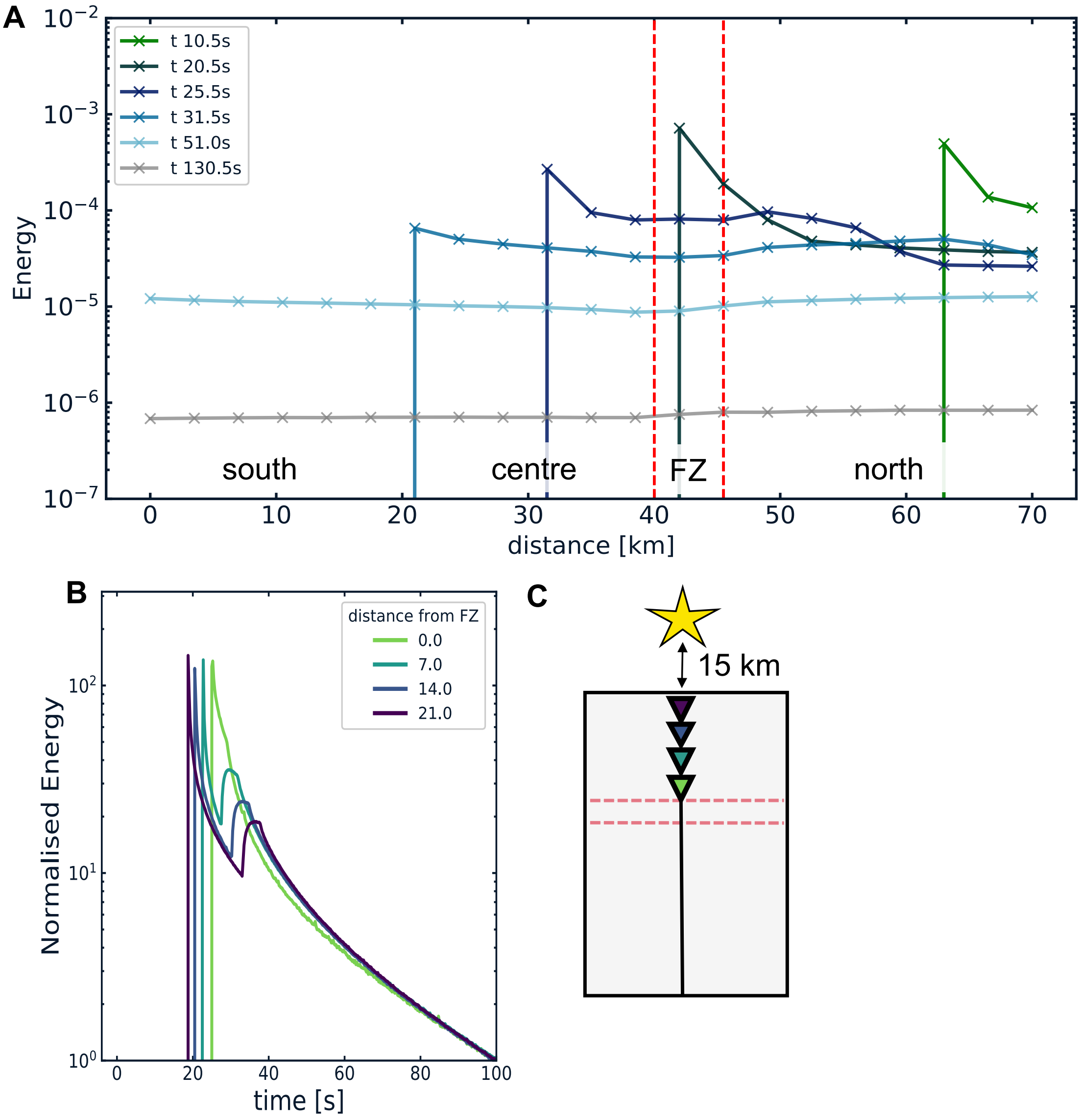

Figure 4.12: A) Snapshots of energy propagation, showing the effect of a strong scattering zone. The graphs show the energy density as function of distance (from right, north, to left, south) at different times. The red dashed lines indicate the fault zone. B) Normalised energy density versus time for four different receivers (7 km apart) in the same simulation. C) Simple non-uniform model used for the simulation exhibiting a narrow fault zone, with $W = 10$ km, $\ell = 10$ km inside the FZ, $\ell' = 150$ km outside the FZ and $Q_i = 100$ everywhere. The receiver line is oriented north-south, in line with the source in the north, 15 km from the first receiver (yellow star). In panels B and C, colours are used to encode the distance between the station and the fault zone.

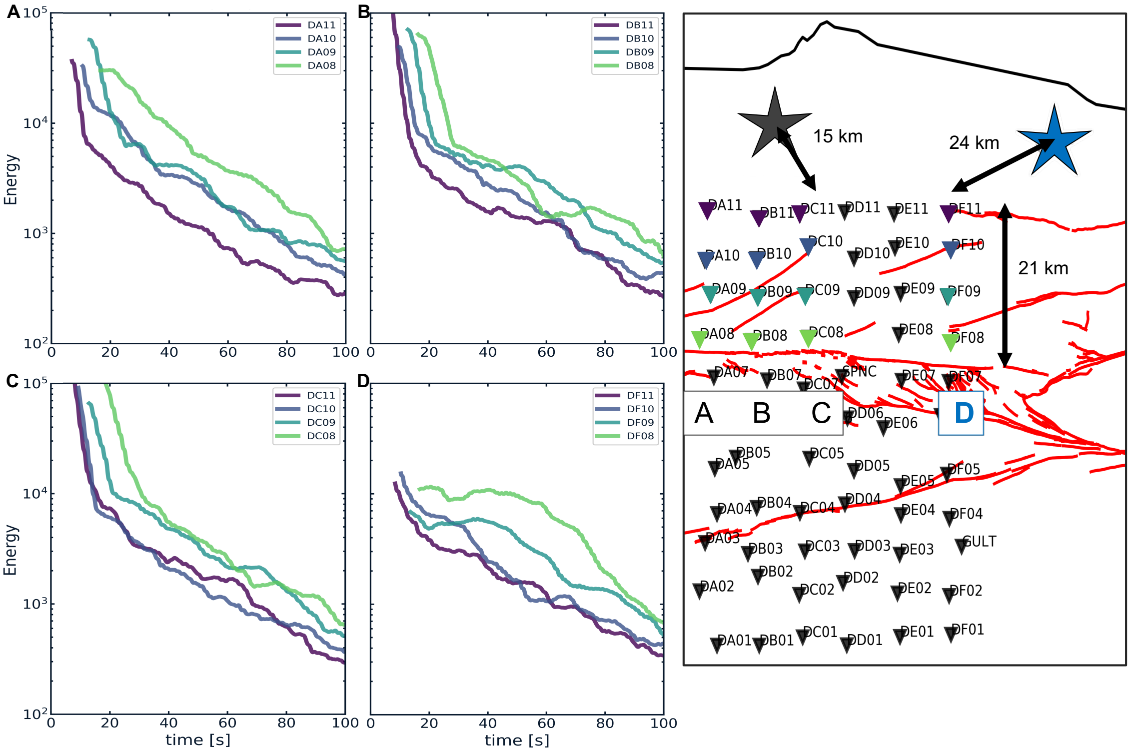

Figure 4.13: Observations of energy envelopes for station pairs oriented perpendicular to the fault zone. The same colour code as in Fig. 4.12B-C is used to indicate the distance between the stations and the fault zone. The map view shows sections A-D. For section A-C, the virtual source is the grey star (permanent station KO07). For section D, the virtual source is the blue star (permanent station KO06). The distance to the virtual sources are indicated on the map. Note: envelopes have been re-scaled with respect to the distance, d, between virtual source and station ($20 \times d$) to enhance the visibility of energy move-out, i.e. the envelopes are shifted on the log-scale to separate them.

one that seems most optimal from the previous section (with a FZ width, W, of 5.5 km and $\ell = 10$ km inside, and $\ell = 150$ km outside the FZ). The configuration for these simulations is different than previously. The model space is again non-uniform but the receiver line is north-south oriented. Snapshots of the resulting energy distribution, normalised energy envelopes as a function of lapse-time and the simulation configuration are shown in Fig. 4.12A-C, respectively. The most striking feature we observe on both the time-domain envelopes and the snapshots is a 'bump', which can be interpreted as back-scattered energy from the fault zone. When the ballistic energy reaches the fault zone, a front of diffuse energy propagates back towards the direction of the source (Fig. 4.12A). Fig. 4.12B shows the same feature, where for stations farther away from the FZ it is easier to distinguish between ballistic energy and back-scattered energy. As we can see when the station is closest to the FZ, both back-scattered energy and ballistic energy arrive at similar times. At a lapse time of the order of 50 s, we observe an inhomogeneous distribution of energy associated with the lateral variations of scattering properties that progressively disappears at long lapse-times (Fig. 4.12A). If this phenomenon of strong back-scattering energy is also present in the actual data, mixture of these energies can have profound implications for the coda decay and scattering properties analysis. Unfortunately, identification of these bumps in the actual CCFs proved to be more difficult than expected.

In the map view of Fig. 4.13 we show four sections (A-D) perpendicular to the fault zone, with a 'virtual source' roughly in line but as far as possible from the stations to accommodate a move-out of this potential back-scattered energy. Sections A-C have permanent station KO07 (grey star) and section D has permanent station

KO06 (blue star) as their virtual source. The simulation (Fig. 4.12B) discussed above is most similar to section B of Fig. 4.13. Additionally, the colour codes for the envelopes are kept similar. It is expected for the back-scattered energy to arrive later in the stations farther away from the fault zone. Unlike the predictions from the simulations, we fail to observe back-scattered energy in the data (Fig. 4.13). The simple model with a strong narrow band of scattering (Fig. 4.12) seems to make predictions that are impossible to discern in the data. This suggest that the fault zone is far more complex than the simple conceptual model proposed in this paper. Other medium properties such as the density and seismic velocity may be significantly different inside the fault zone versus outside. This can cause a high acoustic impedance contrast and therefore trap energy within the fault zone (Ben-Zion and Sammis 2003). In our simulations we have not taken other medium properties than intrinsic attenuation and scattering mean free path into account. It also seems reasonable to think that there are variations of scattering strength along the strike of the fault.

4.5.4 Fault zone coda energy concentration

As described in Section 4.3.4, when a virtual source is inside the northern branch of the fault the scattered energy appears to localise inside the fault at a distance larger than 20 km and for lapse times between 25 and 65 s (Fig. 4.5B). For comparison, no energy concentration is found for the scenario where the virtual source is in the southern most part of the study area (Fig. 4.5A). We observe that the relative energy spot is slowly propagating away from the source. This suggests that the energy concentration could be related to the diffuse energy in the fault zone where the small

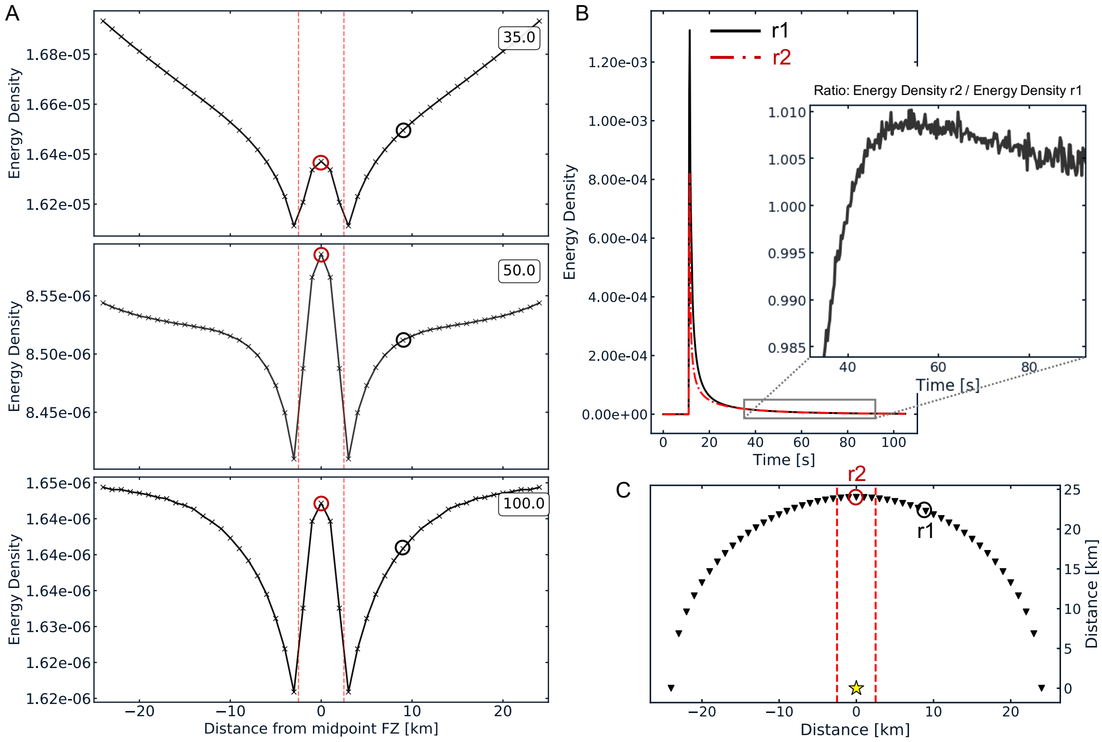

Figure 4.14: Simulation of energy entrapment in the fault zone for a non-uniform model with a source inside the fault zone. A) On a linear scale the energy versus distance from the centre of the fault zone is shown, before (t =35 s), during (t =50 s), and after (t =100 s) energy entrapment. The black and red circles denote station r_1 and r_2 respectively, as indicated on panel C. B) On a linear scale the energy versus time at two receivers, r_1 (outside the FZ; black solid line) and r_2 (at the centre of the FZ; red dash-dotted line). The inset shows the energy density ratio between the two receivers (r_2/r_1) in the time window indicated by the grey box. C) Configuration of the simulation. Black triangles represent the 49 receivers, the distance to the middle of the FZ between the stations increments by 1 km. All stations are at equal distance from the source (yellow star).

mean free path implies a slow expansion with respect to the surrounding medium. To verify this further we performed an additional simulation, where the source is put in the middle of the fault zone, and the receivers are placed in a half-circle over the fault zone with the virtual source at its centre. The source-receiver distance is therefore constant, 24 km, and the total of 49 receivers are placed with 1 km increment of distance to the median line of the fault zone. This allows for relative energy analysis without the source receiver distance dependence in the region around the fault zone. The scattering properties (uniform Q_i=100, ℓ=10 km inside and ℓ=150 km outside the fault zone) and width of the fault zone (∼5 km) are similar to the optimal model described in the previous section.

Fig. 4.14A shows clearly the diffuse energy concentrated in the fault zone. At 35 s, the energy is actually minimum in the region of the fault, although a small secondary maximum is visible in the centre of the fault zone. For this early time, the dominant effect is the strong scattering attenuation in the fault zone while the diffuse energy in the fault is relatively weaker than in the surroundings. At 50 s the diffuse waves have a higher energy in the fault zone than in the surrounding region. This dominance lessens at 100 s when the scattered wave field is increasingly homogenised. The negative halo just outside the fault zone of Fig. 4.14A cannot be observed in the data (Fig. 4.5B). This may be because the data is not sampled densely enough, with the array having a 7 km inter-station spacing. Another contributing factor could be the oversimplification of our model. The actual fault zone may have a more gradual change in scattering properties than our model that has an abrupt large scattering contrast. A comparison of the energy as a function of time for one receiver outside the fault zone (r_1) and one inside the fault zone (r_2) is shown in Fig. 4.14B, where we can observe in the inset that the energy density of r_2 exceeds that of r_1 after 40 s. The location of the receiver outside the fault zone is chosen close to the fault zone but outside the negative halo. The simulation is reproducing the observation of a concentration of energy in the fault zone during a limited period of time starting much later than the passing of the ballistic waves and their possible local resonances. This effect, and particularly the fact that it is late and transient, cannot be explained by simple wave amplification effects and is therefore the signature of the actual non-uniform properties of scattering. The stronger scattering attenuation towards the eastern part of the fault zone reported by Izgi et al. (2020) is yet another observation supporting the idea of a non-uniform strong zone of scattering. Although we see similar behaviour between the data and the model, the match between the two is far from perfect quantitatively, likely due to the complexity of the fault zone and surrounding geology. While our model certainly oversimplifies the reality, it offers an explanation for the late concentration of energy, which is consistent with the geological observation of a narrow heterogeneous fault zone. In the southern branch of the NAF we did not find any evidence of a similar transient local increase of relative energy. This is in line with the findings of Section 4.4.2, that is the lack of significantly different scattering properties for this branch of the fault zone compared to the surrounding southern region. The absence of both concentrated energy and distinct scattering properties in the southern branch may be explained by the smaller damage zone, e.g. due to the lower activity of this fault (e.g. Aslan et al. 2019, and references therein).

4.6 Conclusions

This paper demonstrates that a high scattering limited fault zone is a reasonable first order model for the North Anatolian FZ in the area of the Izmit rupture zone. A narrow fault zone of ∼5.5 km width (± 50 %) with a scattering mean free path of the order of 10 km, surrounded by a medium with 150 km scattering mean free path, has been obtained by analysis of ambient noise cross-correlations in the 0.1-0.5 Hz frequency band. We verified that our model reproduces a concentration of energy in the fault zone when the source is inside, similar to what we observe in the data. Currently, ambient noise monitoring methods rely on the assumption that scattering properties are the same across fault zones. Here, we have demonstrated that this is not the case. Therefore, laterally varying scattering properties need to be taken into account in future monitoring efforts.

From a methodological perspective we can conclude that one can use the coda of correlations for attenuation studies. Although we know that scattering properties vary between different types of crust, e.g. between volcanic and normal crust, variations on such short scale have not been reported yet. Our results have direct implications for applications such as monitoring velocity changes in the Earth's crust. In particular, our study suggests that a good estimate of the spatial variations of scattering properties is key to correctly recover the temporal variations of seismic properties. Future improvements of our scattering model of the NAFZ should be focused on incorporating lateral variations along the fault zone, because the data revealed that there is even more complexity than described by our model. A larger array, with an extension towards the east, is necessary to capture this complexity.

4.7 Outlook

We have seen that wave propagation is affected by the distribution of scattering properties For this reason, it is necessary to have knowledge about the scattering and intrinsic attenuation coefficients of the medium that is targeted for monitor. The scattering properties serve as input parameters for the spatial sensitivity kernels as we will see in the next Chapter. In Chapter 5 we will also discuss in detail the implications of the distribution of scattering properties on the spatial sensitivities of coda waves.

4.8 Appendix A: Monte-Carlo simulations in laterally varying scattering media.

We remind the reader that Monte-Carlo simulations designate a class of stochastic methods of solution of radiative transport equations. In this approach, energy is represented by discrete seismic phonons who undergo a sequence of collisions upon which their direction of propagation changes according to the laws of scattering. In a medium with uniform scattering properties, the distance d between two collisions (also called free path length) is governed by an exponential probability law of the form $p(x < d < x + dx) = \ell^{-1} \exp(-x/\ell)dx$ with ℓ the scattering mean free path. For greater details, we refer the reader to the literature as summarized in Shearer and Earle (2004) and Sato, Fehler, and Maeda (2012). To simulate the transport of seismic energy in media exhibiting spatial variations of scattering and absorption, we have used the so-called method of null or delta-collisions (Lux and Koblinger

1991). This is an exact method of simulation that maps the transport process from a medium where attenuation properties vary spatially onto a medium where they are constant. Let us remark first that, in the framework of Monte-Carlo simulations, absorption may be treated as a scattering process that reduces the energy of a particle by a factor B, with B the local value of the albedo. Hence, to get a grasp on the method it is sufficient to treat the case of non-uniform scattering properties, which is also most relevant to our applications.

Consider a 2-D transport equation with a spatially varying mean free path $\ell(\mathbf{r})$. The equation governing the transport of the energy is (e.g. Paasschens 1997):

$$(\partial_t + c\mathbf{k}\cdot\nabla + \tau(\mathbf{r})^{-1})e(t,\mathbf{r},\mathbf{k}) = \tau(\mathbf{r})^{-1}\int_{2\pi} p(\mathbf{k},\mathbf{k}')e(t,\mathbf{r},\mathbf{k}')dk' \qquad (4.4)$$

with $e(t,\mathbf{r},\mathbf{k})$ the energy density flowing in direction $\mathbf{k}$ (vector on the unit circle) at time t and position $\mathbf{r}$, $p(\mathbf{k},\mathbf{k}')$ the scattering pattern governing the rate of transition from propagation direction $\mathbf{k}'$ to propagation direction $\mathbf{k}$, c the seismic velocity, and $\tau = c\ell$ the scattering mean free time. The integral on the right-hand side is over all the directions in the plane. We remark that if $e(t,\mathbf{r},\mathbf{k})$ solves Eq. (4.4), it also solves the following equation where the effective scattering mean free time τ_e is <u>constant</u>:

$$(\partial_t+c\mathbf{k}\cdot\nabla+\tau_e^{-1})e(t,\mathbf{r},\mathbf{k}) = \tau(\mathbf{r})^{-1}\int_{2\pi} p(\mathbf{k},\mathbf{k}')e(t,\mathbf{r},\mathbf{k}')dk'+\tau_{nc}(\mathbf{r})^{-1}\int_{2\pi}\delta(\mathbf{k},\mathbf{k}')e(t,\mathbf{r},\mathbf{k}')dk', \qquad (4.5)$$

where $\delta(\mathbf{k},\mathbf{k}')$ is the delta function on the unit circle, $\tau_{nc}(\mathbf{r})$ is the scattering mean free time for the null or delta scattering events and $\tau_e^{-1} = \tau(\mathbf{r})^{-1} + \tau_{nc}(\mathbf{r})^{-1}$. In effect, all that we have done is to add the same term $\tau_{nc}(\mathbf{r})^{-1}e(t,\mathbf{r},\mathbf{k})$ on both sides of Eq. (4.4). But the benefit is in fact immense because in the fictitious medium with null collisions, the scattering mean free path is constant, so that the most basic implementations apply straightforwardly. Note that there is a certain degree of arbitrariness in the definition of τ_e. Assuming that τ is bounded in the domain of interest, we may simply take $\tau_e^{-1} = \sup \tau(\mathbf{r})^{-1}$.

In practice, these ideas may be very easily implemented as follows. The transport process is simulated in a medium where the mean free path $l_e = c\tau_e$ is constant, so that the simple exponential probability law described above still applies. At each collision point $\mathbf{r}_c$, we must decide whether a true or a fictitious scattering event occurs. To carry out this task, we select a uniformly distributed random number ϵ in the interval $]0, 1[$ and compare it to the local scattering conversion rate. If:

$$\epsilon < \tau(\mathbf{r}_c)^{-1}/\tau_e^{-1} \tag{4.6}$$

then a genuine scattering occurs and we proceed as usual with the selection of a new propagation direction. Otherwise, we have a null collision and the propagation direction is unchanged up to the the next collision. The main computational overload comes from the fact that we are in fact simulating more scattering events than actually occur in the real world. But this is largely counter-balanced by the considerable simplification of the free path length selection as well as the absence of complicated geometrical tracking of the particle.

4.9 Supplementary material

Supplement

S9.1 Additional information on data

In the section ‘Data processing and decay properties of coda waves’, we introduced the data of the Dense Array of North Anatolia, which has 73 three-component stations. In both our Q_c measurements and the MLTW analysis we average the horizontal component pairs before we analyse the data. This is because the vertical components look rather noisy, which we can observe in Fig. S15. The vertical components (last column and last row) show a strong band of energy near t = 0, which is most likely related to tele-seismic body waves.

Analysis of the power spectra of the horizontal components in all four sub-regions show that in the frequency band 0.1-0.5 Hz, most energy is around 0.3 Hz (Fig. S16). With a group velocity of $\sim$ 2.1 km/s, the dominant wavelength in our data is therefore $\sim$ 7 km. The scattering mean free path in the fault zone, in the order of 11 km, is thus larger than the dominant wavelength.

S9.2 Additional information on Q_c^{-1}

Our measurements of the coda decay are done on the envelopes of the averaged horizontal components. Fig. S17 and S18 show the Q_c measurements of the individual component pairs for the anti-causal and causal parts, respectively. The stations are alphabetically ordered, which implies a geographical ordering (see Fig. 1 of the manuscript). We observe that the maps show similar results, implying no obvious

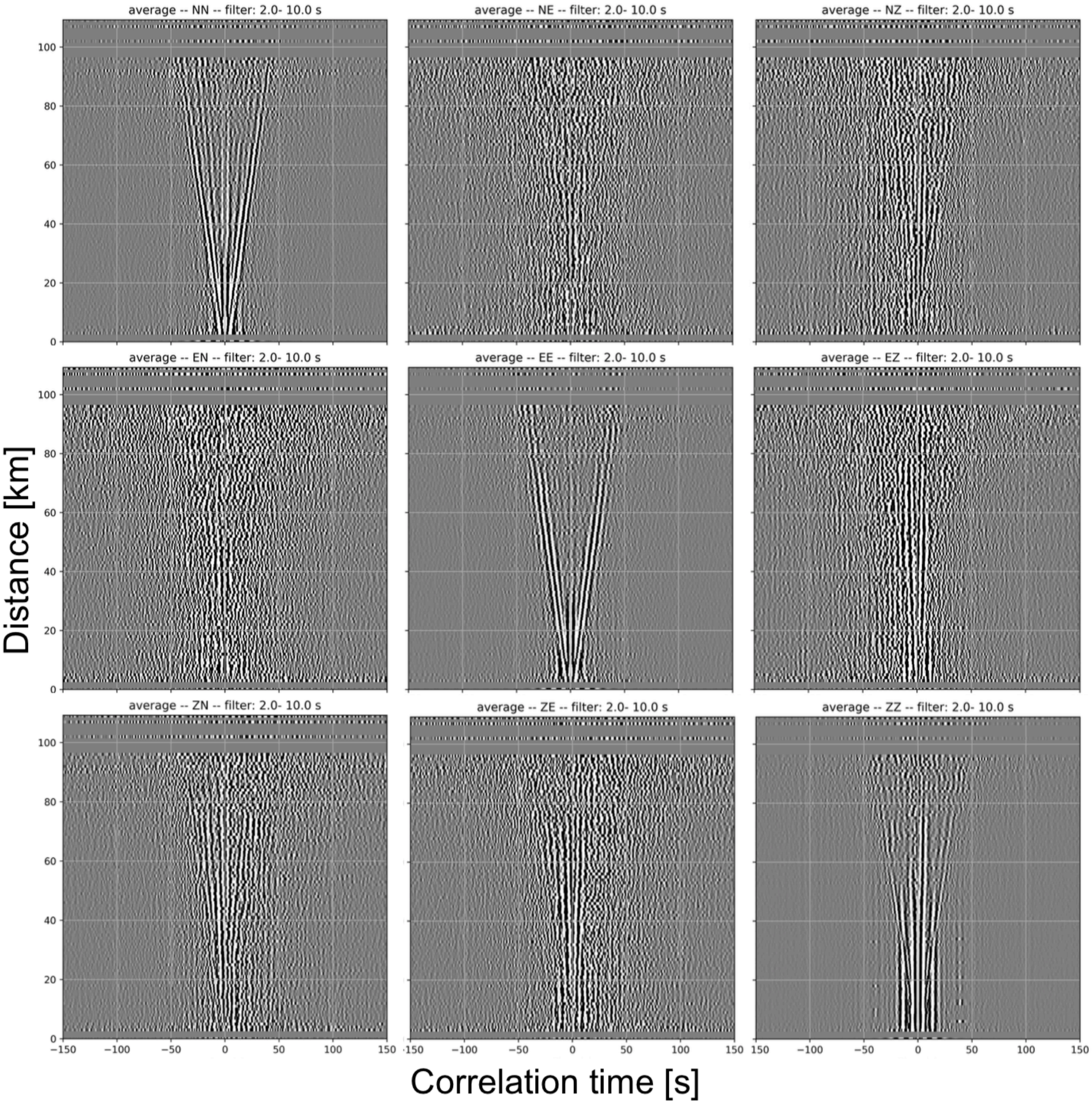

Figure S15: Bin-stacked cross-correlation functions (CCFs) calculated for all inter-station paths of the DANA network, for all three-component combinations. The data used to compose the CCFs were filtered between 0.1 and 0.5 Hz; the resulting CCFs are binned, stacked and normalised for display purposes.

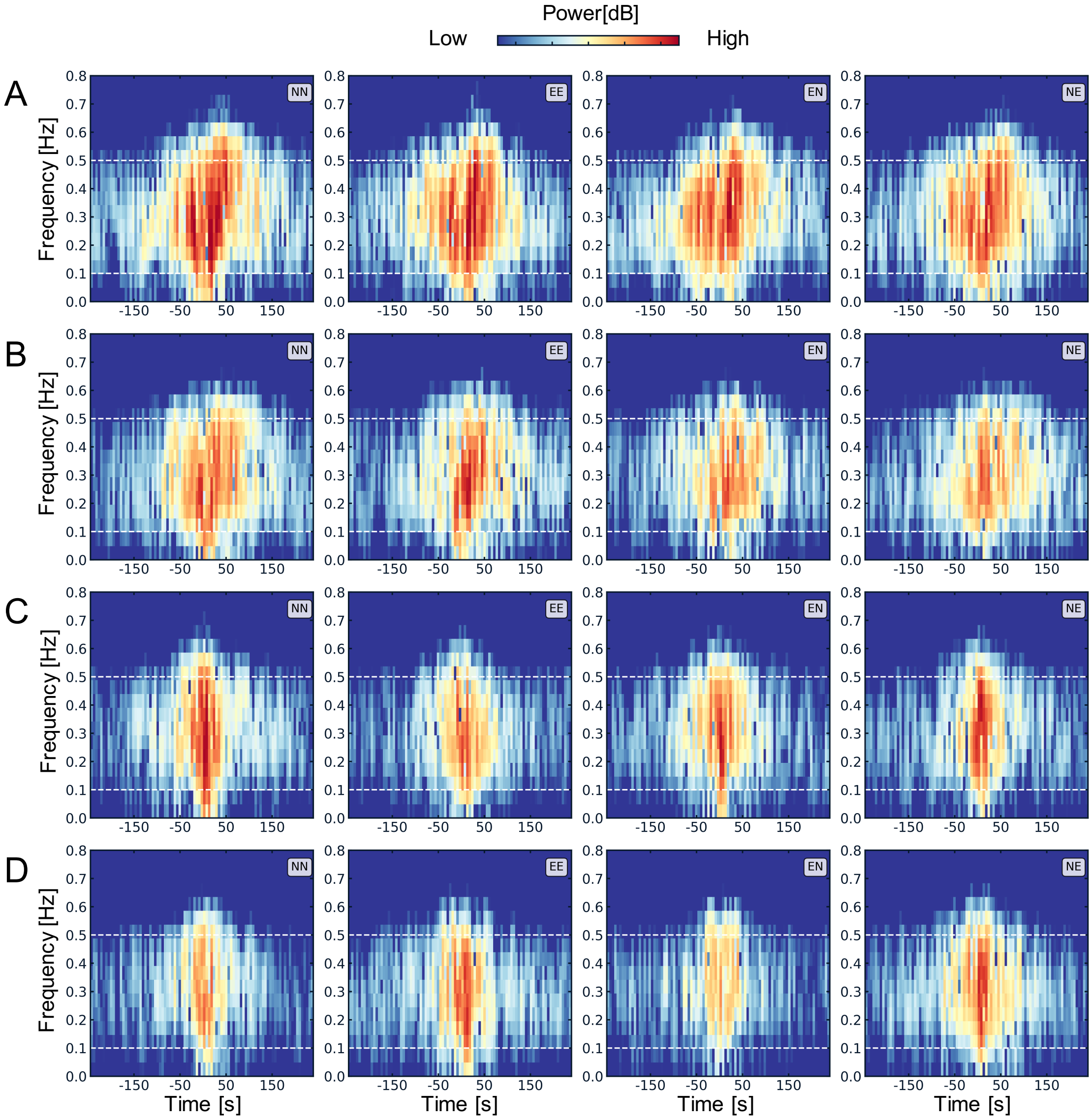

Figure S16: Spectrograms of the horizontal component pairs for the four sub-regions: A) north, B) fault zone, C) centre and D) south. Colder colours for less energy. The white dotted vertical lines show the frequency band for which we filtered the data (0.1 and 0.5 Hz).

bias in the measurements due to directivity of the noise source. This is as expected, because the waves that form the coda are theoretically, especially in the later parts, less affected by the directivity of propagation and thus by the component pair.

S9.3 Additional information on scattering properties Q_i and ℓ

Effect of Velocity

This section explores the correct surface wave group velocity per sub-region. The initial value is derived from the first arrivals on the CCFs. In these tests we change the velocity in the RTE and for the estimates of the NEDs and compare the misfits with the misfits we have for the initial velocities. The range of velocities we test are -0.7 to +0.3 km/s with steps of 0.1 km/s w.r.t. the initial velocity. For the northern sub-region (Fig. S19) using a lower velocity minimises the minimum misfit slightly and the resulting ℓ is higher, but still not better constrained. No change for Q_i compared to the initial velocity. For the central region (Fig. S20), using a 0.6 km/s lower velocity the optimal Q_i is slightly lower and ℓ is higher but still not better constrained. Lastly, for the southern sub-region (Fig. S21), we find a smaller minimal misfit using a velocity that is 0.2 km/s slower. However, the found Q_i and ℓ do not change. Fig. S22 - S24 show the velocities derived from the first arrivals of the CCFs and the ones that minimizes the misfit.

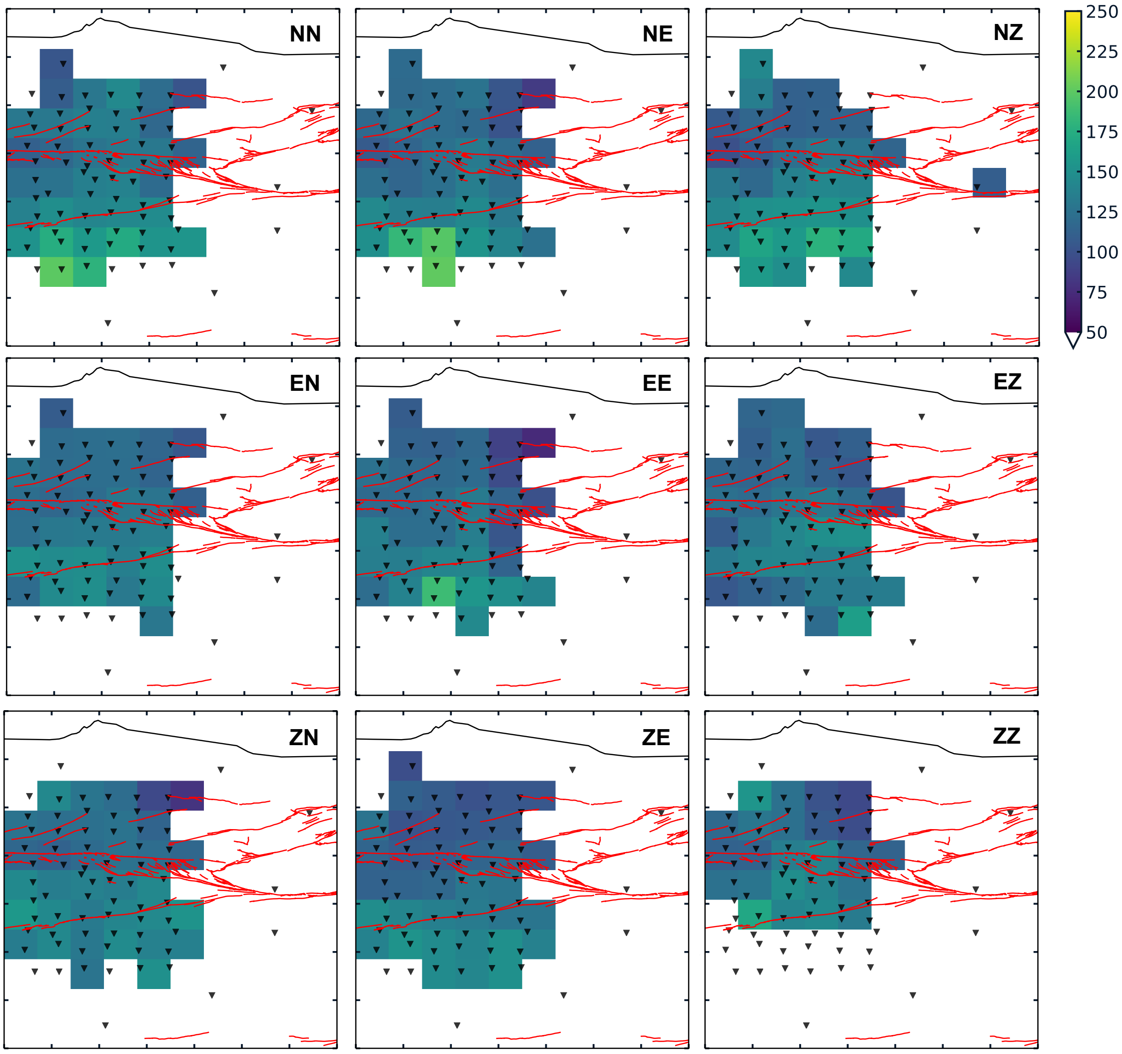

Figure S17: Q_c maps for anti-causal part of CCFs for all component combinations. Each cell shows the inverse of the arithmetic mean of the measured Q_c^{-1} values. Only cells with a minimum number of 5 rays per cell are shown. Other selection parameters are the interstation distance < 35 km and a correlation coefficient of the linear regression, $R^2 > 0.75$.

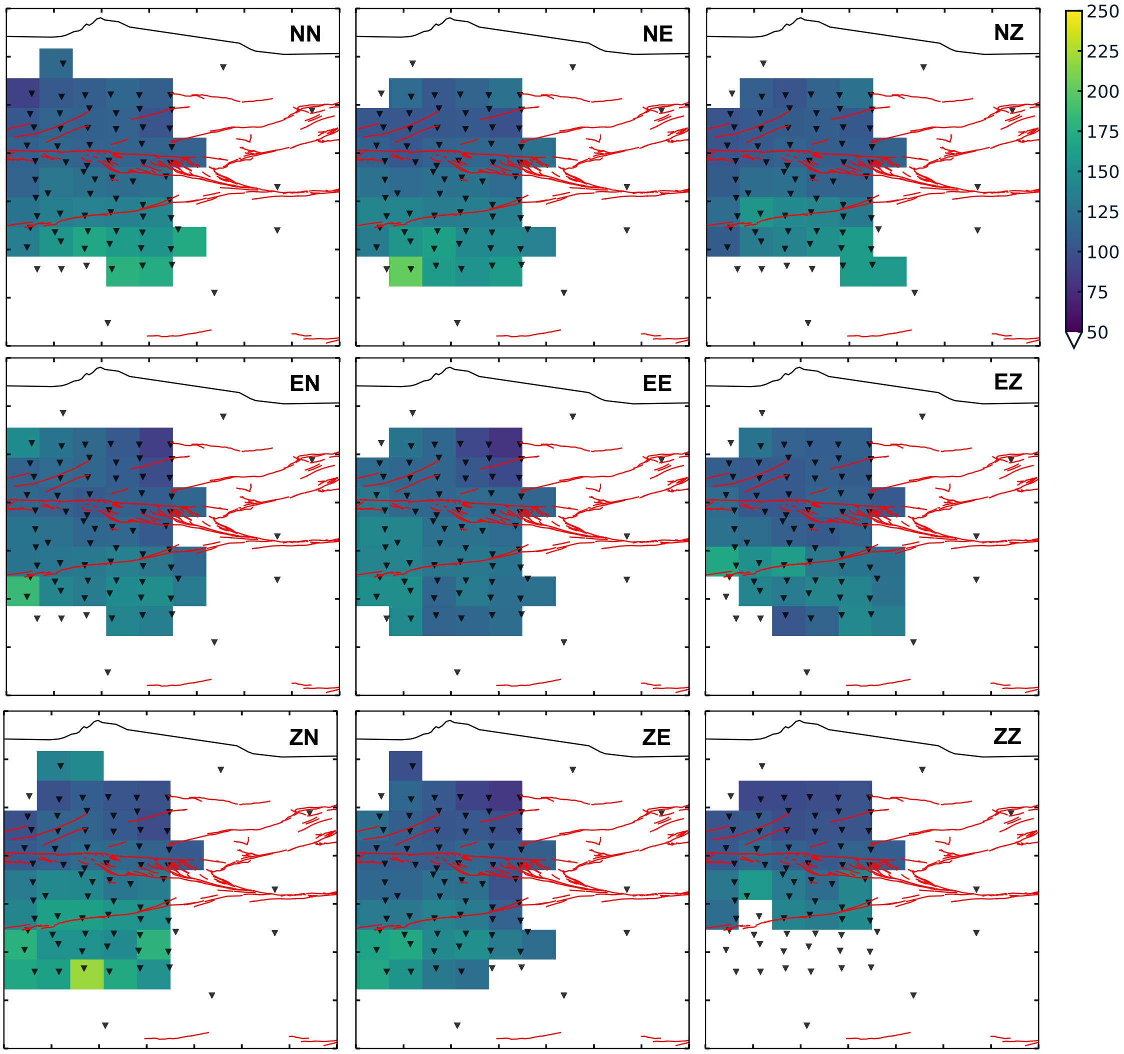

Figure S18: Q_c maps for causal part of CCFs for all component combinations. Each cell shows the inverse of the arithmetic mean of the measured Q_c^{-1} values. Only cells with a minimum number of 5 rays per cell are shown. Other selection parameters are the interstation distance < 35 km and a correlation coefficient of the linear regression, $R^2 > 0.75$.

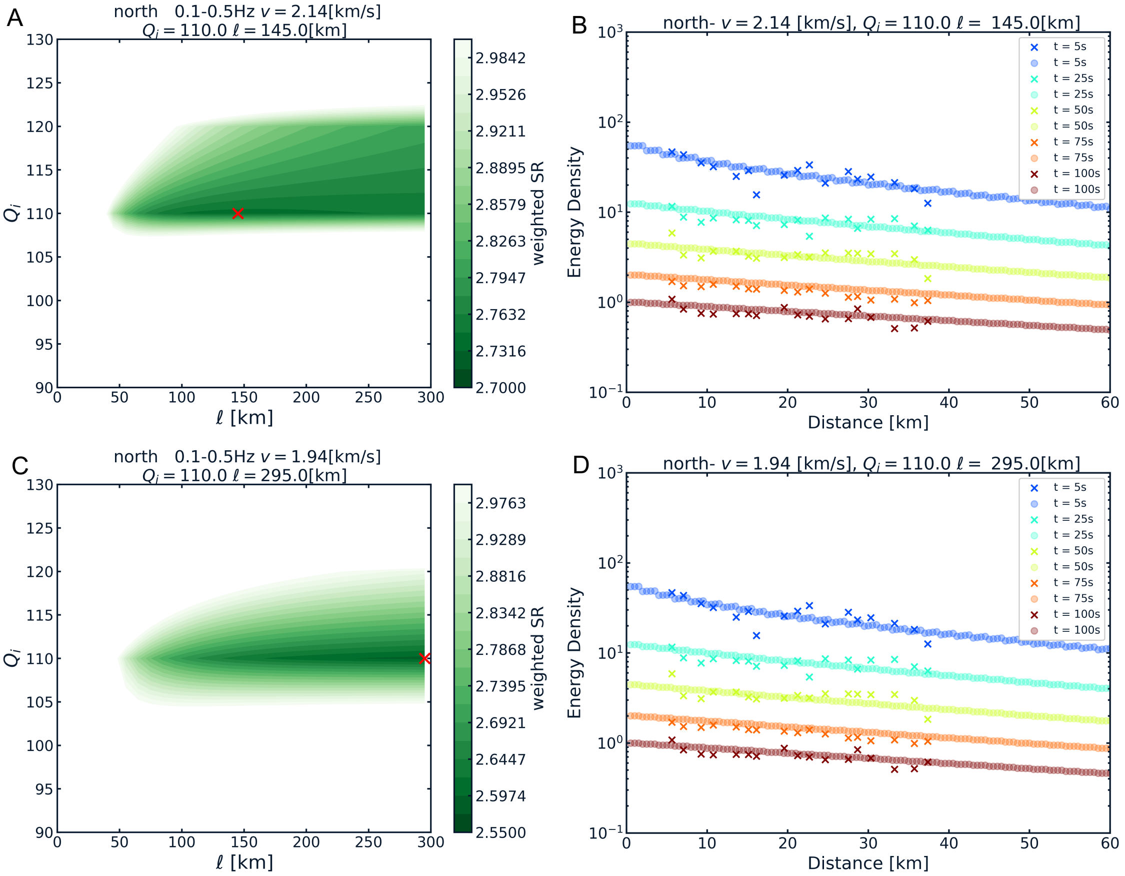

Figure S19: Velocity test results for northern sub-region. The left column shows the SM and the right column the observations (‘X’) with solution for the 2D-RTE (‘o’) using the optimal parameters. The colours indicate the time windows. A)-B) are the misfit using the original velocity derived from the arrivals on the data. C)-D) for a velocity that is 0.2 km/s less, showing the smallest minimum weighted misfit between observations and 2D RTE.

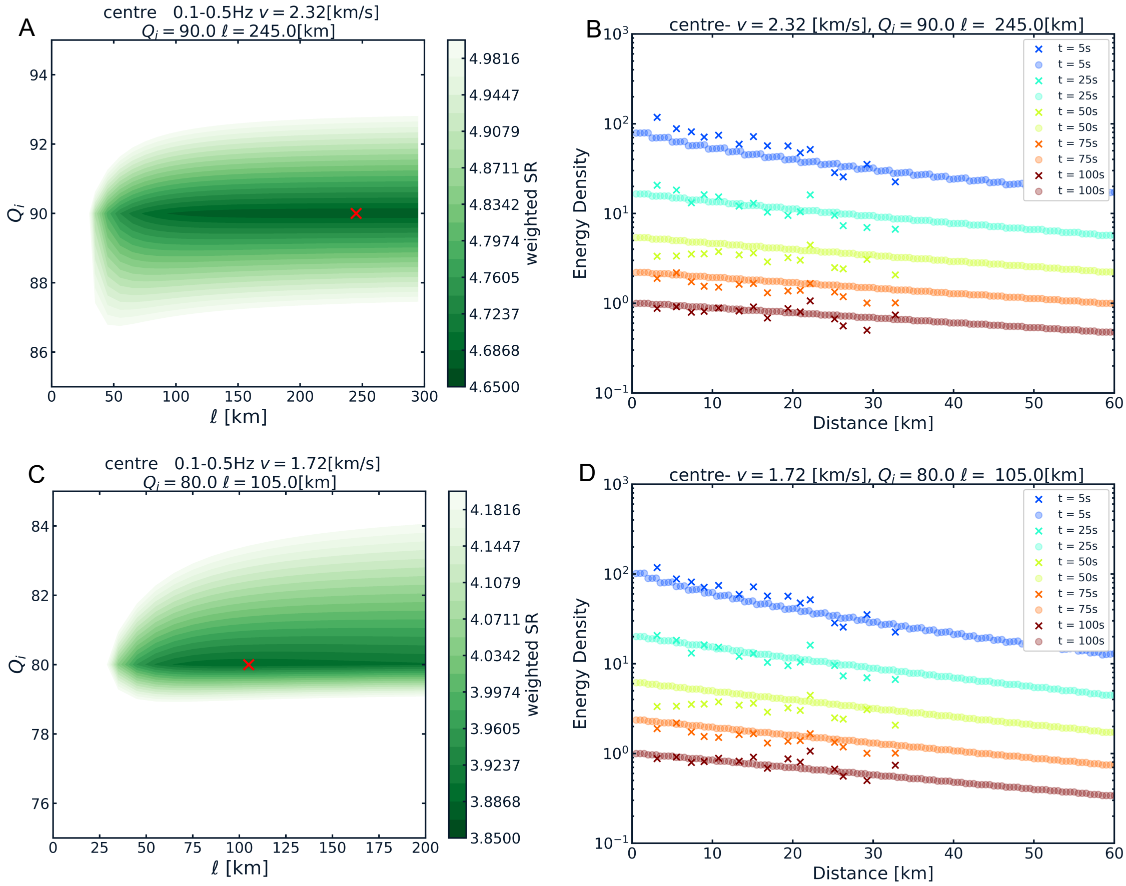

Figure S20: Velocity test results for the central sub-region. The left column shows the SM and the right column the observations ('X') with solution for the 2D-RTE ('o') using the optimal parameters. The colours indicate the time windows. A)-B) are the misfit using the original velocity derived from the arrivals on the data. C)-D) for a velocity that is 0.6 km/s less, showing the smallest minimum weighted misfit between observations and 2D RTE.

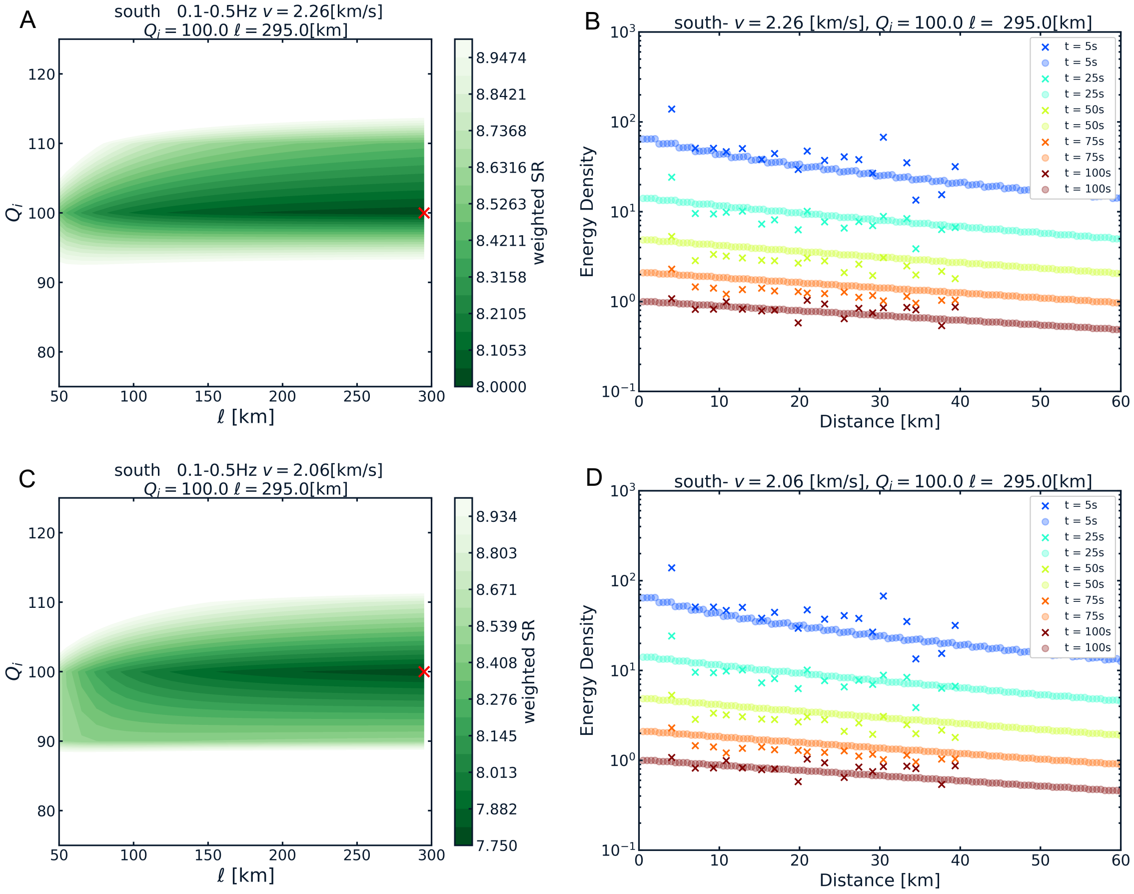

Figure S21: Velocity test results for the southern sub-region. The left column shows the SM and the right column the observations (‘X’) with solution for the 2D-RTE (‘o’) using the optimal parameters. The colours indicate the time windows. A)-B) are the misfit using the original velocity derived from the arrivals on the data. C)-D) for a velocity that is 0.2 km/s less.

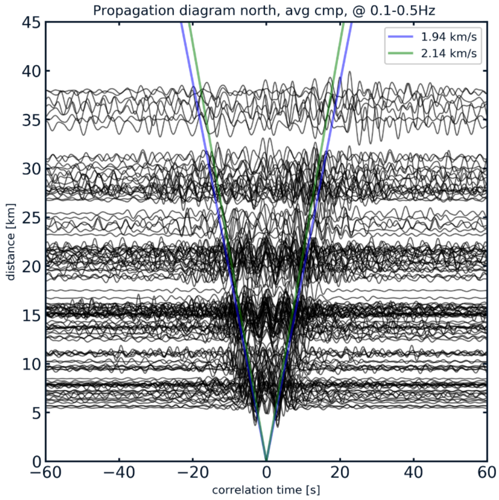

Figure S22: Cross-correlations versus distance diagram for the northern sub-region, with both the initial group velocity (green) and the velocity that gives the smallest misfit (blue) plotted on top.

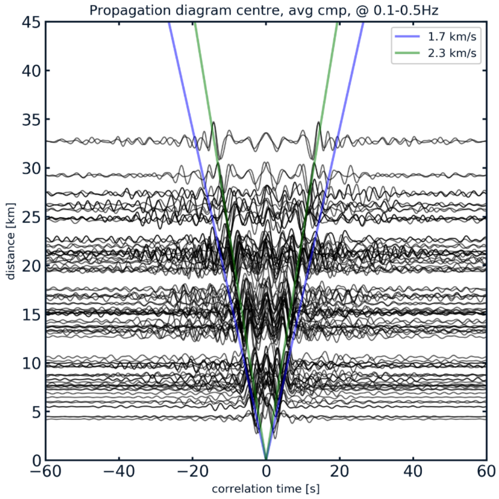

Figure S23: Cross-correlations versus distance diagram for the central sub-region, with both the initial group velocity (green) and the velocity that gives the smallest misfit (blue) plotted on top.

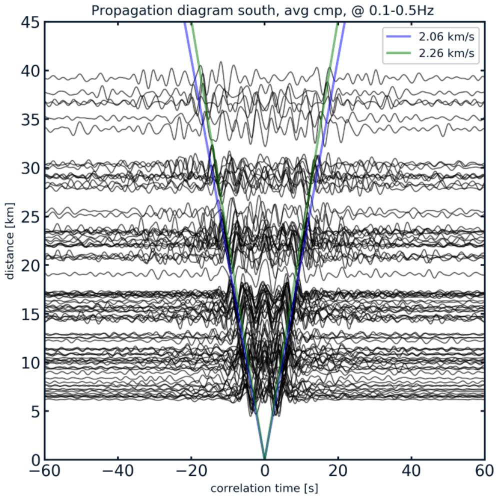

Figure S24: Cross-correlations versus distance diagram for the southern sub-region, with both the initial group velocity (green) and the velocity that gives the smallest misfit (blue) plotted on top.

Effect of Noise

The effect of SNR of the CCFs (or fluctuations in the NEDs caused by e.g. backscattering effects of the fault zone) on the optimisation is analysed by a synthetic inversion test. One group of tests is done in case of strong scattering attenuation, similar to the situation inside the fault zone. The other group of tests for weak scattering attenuation, simulating the situation outside the fault zone. The analytical solution of the RTE is compared with a 'noise-induced' solution of the RTE, in a similar way as the optimisation in the previous section where the observed data is compared to the modelled data. The 'noise' represents the fluctuations in the binned NED values. This 'noise' that we add to the solution, is within one standard deviation (STD) of the individually measured NEDs before binning. A random value within the range of ± 1 STD per distance bin of the FZ is used for the strong scattering

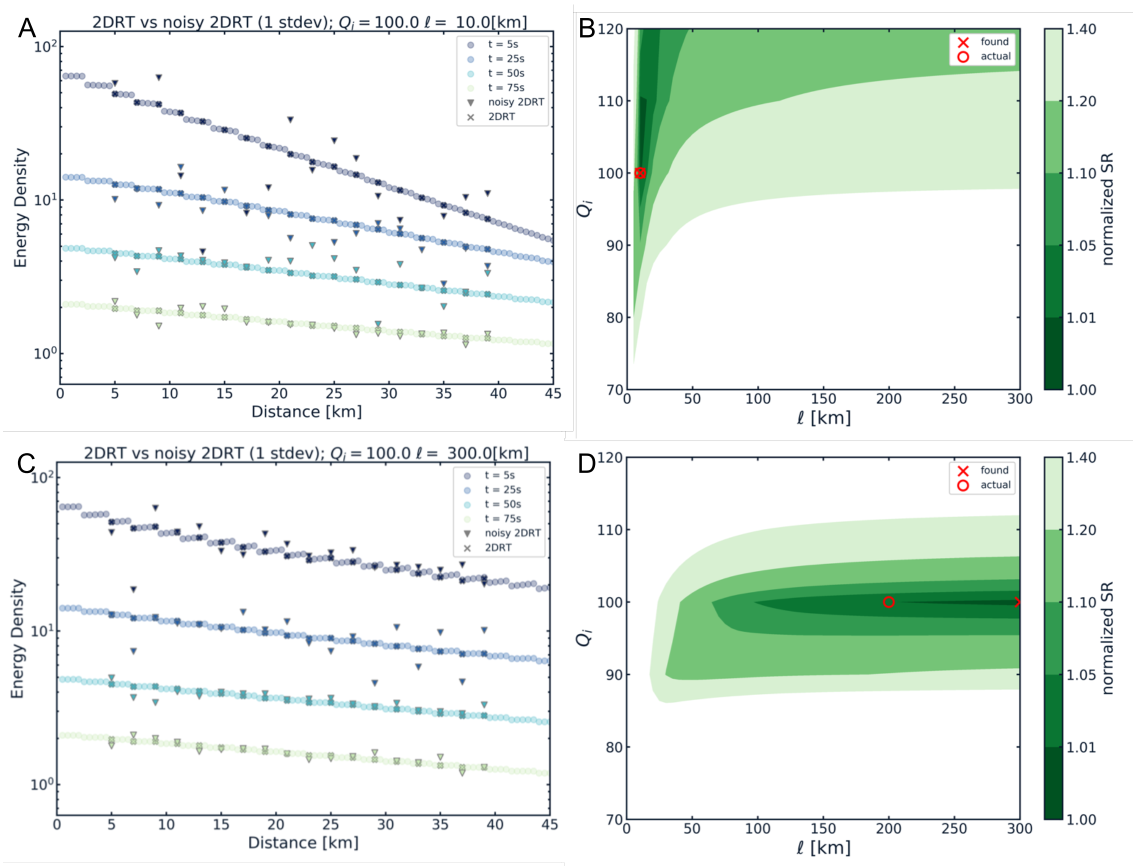

2DRT vs noisy 2DRT (1 stdev); $Q_i = 100.0$ $\ell =$ 10.0[km]

2DRT vs noisy 2DRT (1 stdev); $Q_i = 100.0$ $\ell =$ 300.0[km]

Figure S25: ‘Noise’ test to analyse the influence of fluctuations on the optimisation. A)-B) Case of rapid energy decay, simulating the situation inside the fault zone. C)-D) Case of slow energy decay, simulating the situation outside the fault zone. Panel A and C) show the NEDs for the 2D RTE as ‘o’ and the ‘noisy’ NEDs as triangles. The colours indicate the time windows; lighter colours for later times. Panel B) and D) show the normalised SR of the grid searches, with the ‘O’ indicating the value used in the non-noisy 2D RTE, and the ’X’ shows the best fitting value between ‘noisy’ and non-noisy 2D RTE.

attenuation tests. In a similar fashion, random values within the range of ± 1 STD of the central zone are taken as ‘noise’ for the test of weak scattering attenuation. Note that drawing a random value from the ± 1 STD range may underestimate the actual fluctuations we observe in the median NED values, because effectively it simulates a random value in the range of $\pm$ STD$/\sqrt{3}$.

For the strong scattering attenuation case, Q_i^{-1} and ℓ are well-constraint. This applies generally when ℓ is small w.r.t. the aperture of the array. As the scattering mean free path increases, the resolution on ℓ gets lower, i.e. only a range of potential values can be extracted. For ‘too high’ ℓ values, again w.r.t. the array size, the energy does not decay rapidly enough anymore. The distance dependence can therefore not be measured and ℓ cannot be resolved for. The former case seems to apply for ℓ less than 80 km with the current network, and the latter for $\ell > 150$ km. Fig. S25A shows an example of the resulting misfits and plots for small ℓ values.

In case of weak scattering attenuation, it is hard to constrain ℓ as can be observed in Fig. S25B. Q_i^{-1} on the other hand is still decently constrained. The rate of the energy decay with distance is small and therefore the ‘noise’ can be a dominant factor in the average spatio-temporal energy decay of the sub-region. Hence, for some regions it seems impossible to constrain the scattering mean free path properly with the current network. This is most plausibly the reason why no clear constraint on ℓ can be found for the sub-regions outside the fault zone.

S9.4 Additional information on Monte Carlo simulations

Uniform models

In the first simulations we use a uniform model with Q_i and ℓ as derived in the optimisation on the actual data (Section ‘Mapping of attenuation properties’) to confirm the validity of the simulations. Since the output of these simulations is the total intensity (and after division by the seismic velocity, the energy density) at a chosen location with time, we performed a similar optimisation as we did on the actual observations. This provides us with the opportunity to compare not only the derived scattering properties, but also the measured energy densities per time and distance.

For all four simulations we were able to retrieve the Q_i value accurately and precisely (see Fig. S26). However, the scattering mean free path proves more difficult to retrieve outside the fault zone, as explained in section ‘Mapping of attenuation properties’.

Test on Uniform Q_i

To exclude the effect of Q_i in the simulations, we aim to find one single Q_i value for the entire model space, in order to simplify the other tests by taking one variable out of the equation. This is especially important when examining the influence of the ratio between the scattering mean free path and the width of the FZ. For these test we use a non-uniform model space, one that is divided into four sub-zones, and a E-W receiver line configuration (as used in the main text). The ℓ values in the model space are as derived from the observations. We test three different values for

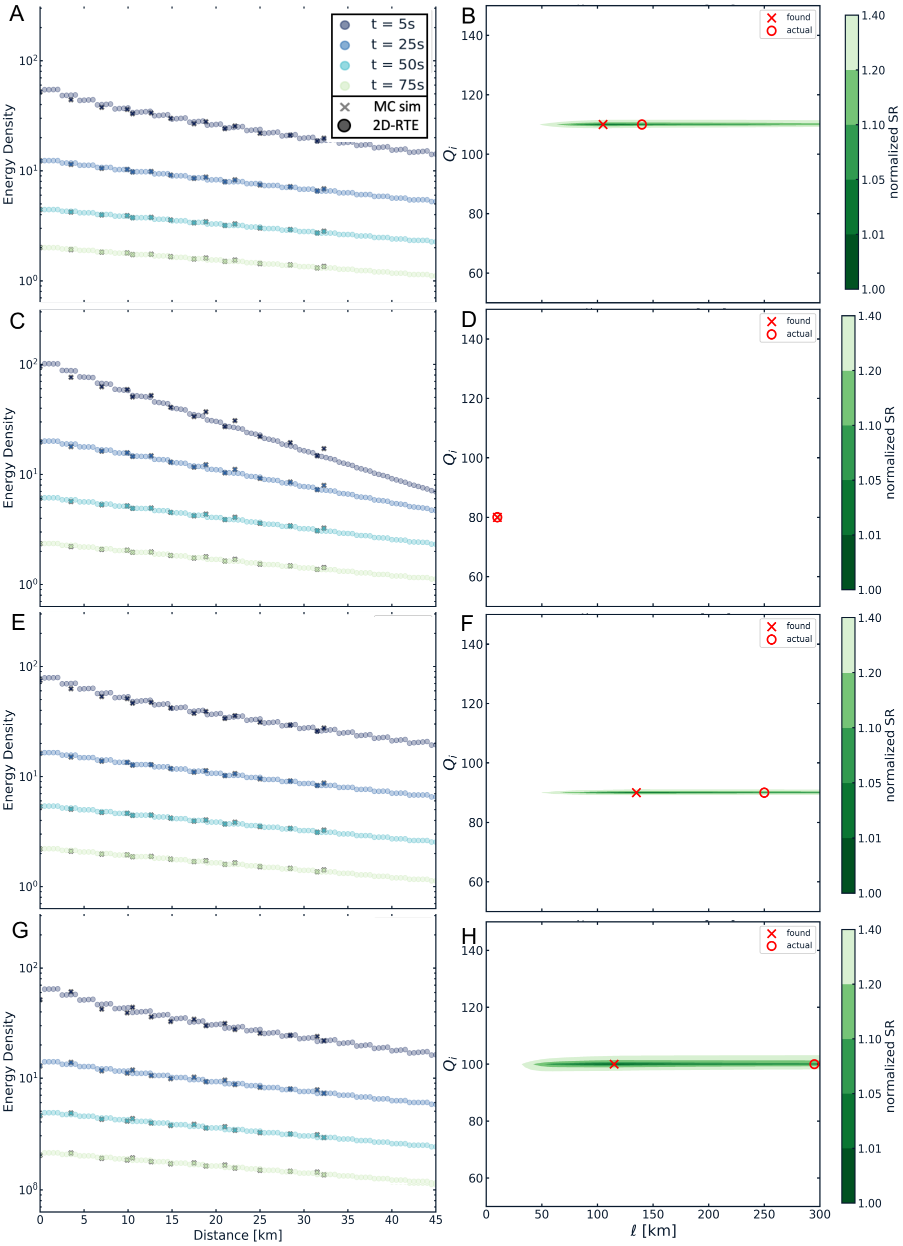

Figure S26: Optimisation results of simulated data for homogeneous models with scattering parameters from optimisation per sub-region. The figures in the left column show measured normalised energy density for simulation ('x') versus normalised energy density of 2D RTE ('o'). The colour of both the X and O indicate the time window as specified in the legend. The right column shows the misfit and best ℓ and Q_i values found for simulations ('X'), the red circle indicates the values used for the simulation. A-B are for the homogeneous model with values of the northern sub-region. C-D, E-F and G-H for fault zone, central and south respectively. NB: these values deviate slightly form the values shown in Fig. 7 of the main manuscript because these are for a grid search performed at lower resolution, so $\Delta Q_i = 10$ instead of 2 and $\Delta\ell = 5$ instead of 2 km.

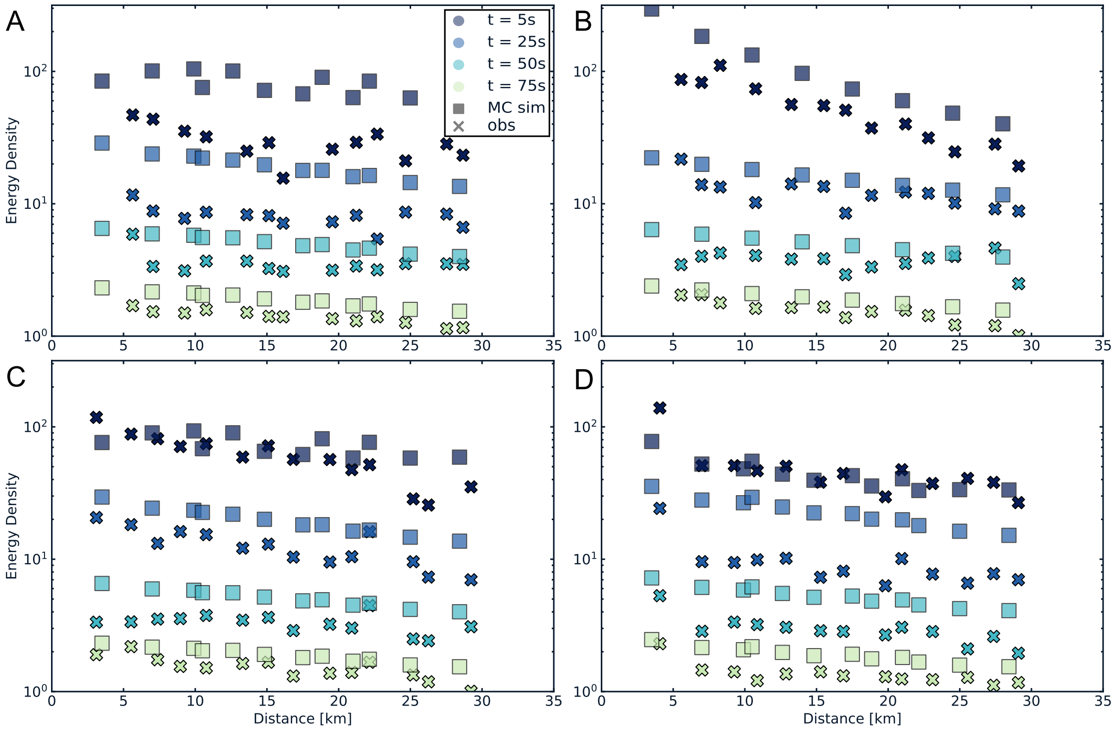

Figure S27: Normalised energy densities of simulation(squares) versus observations ('X') for a simple model using one Q_i=80 for the all four sub-zones and ℓ= 150 km outside the FZ (A,C,D) and ℓ= 10 km the FZ (B).

Q_i: 80, 90 and 100, and compare the results to the observed NEDs. The test results are shown in Fig. S27, S28, S29; panels A-D, correspond to the results in the north, FZ, centre and south respectively. The highest degree of agreement is when using a Q_i value of 100, we therefore chose to continue with this value for the tests from Section 'Constraints on the fault zone width' onward.

Non-normalised simulations compared

In the section 'The signature of a finite width scattering zone', we discuss that the energies at absolute long times for the homogeneous and heterogeneous case are very

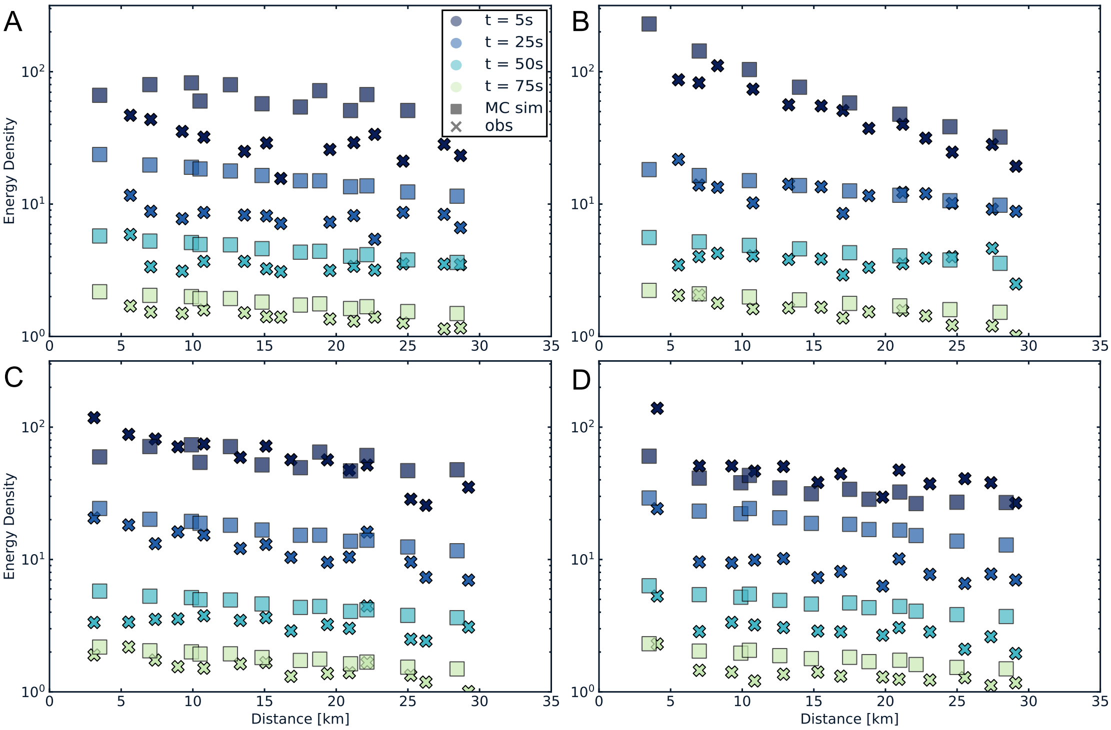

Figure S28: Normalised energy densities of simulation(squares) versus observations ('X') for a simple model using one Q_i=90 for the all four sub-zones and ℓ= 150 km outside the FZ (A,C,D) and ℓ= 10 km the FZ (B).

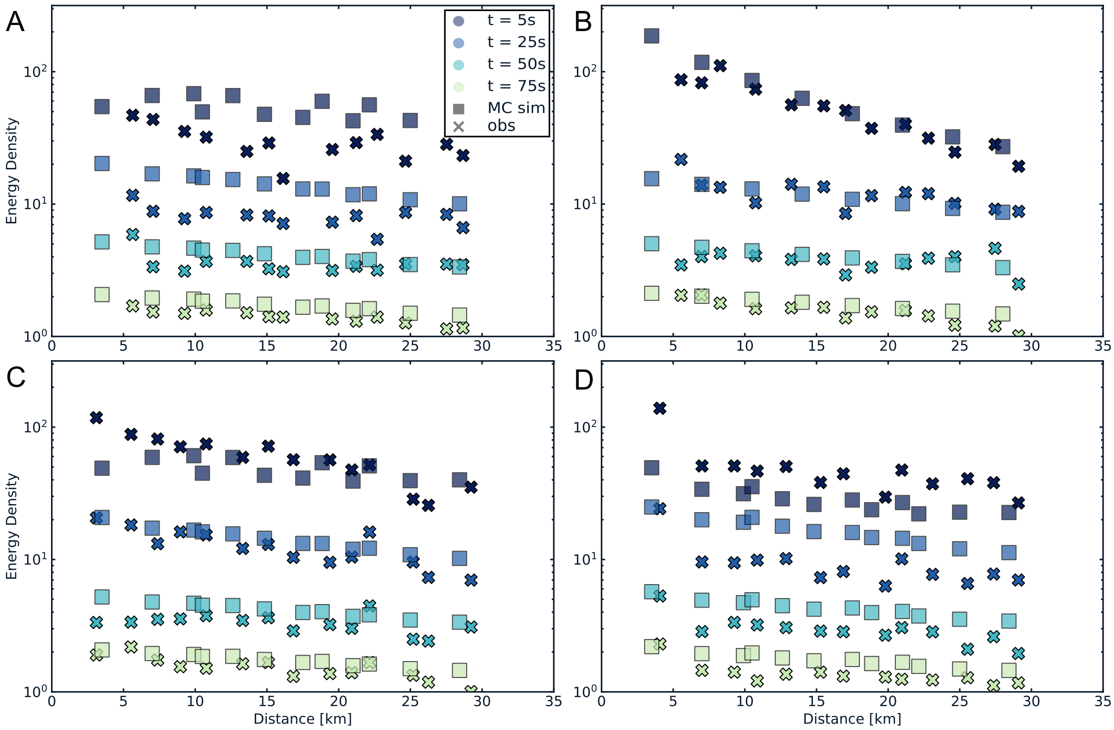

Figure S29: Normalised energy densities of simulation(squares) versus observations ('X') for a simple model using one Q_i=100 for the all four sub-zones and ℓ= 150 km outside the FZ (A,C,D) and ℓ= 10 km the FZ (B).

close. This is shown by the results for the last time window in Fig. S30.

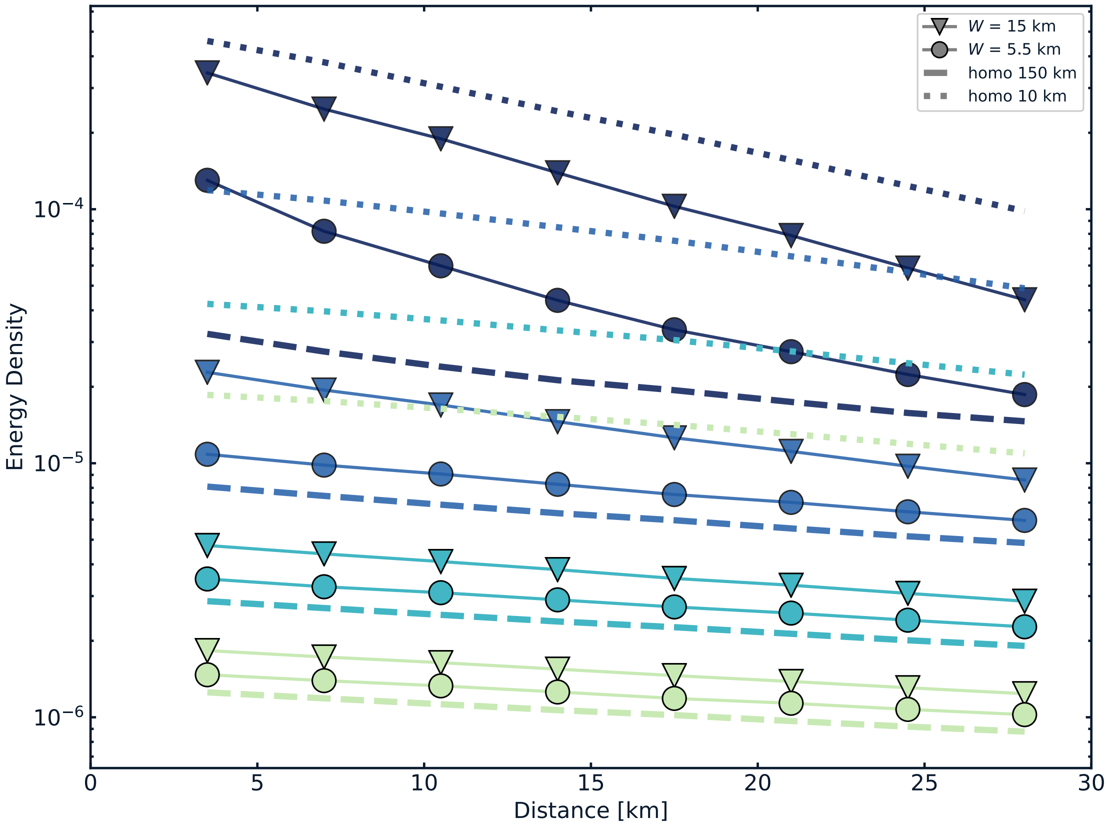

Figure S30: Comparison of spatio-temporal energy evolution of different simulations. The dashed and dotted lines show the non-normalised energy densities for the homogeneous model with ℓ= 150 km and ℓ= 10 km respectively. The non-normalised energy densities for the cases with a strong band of scattering with a width of 5.5 and 15 km are indicated by the lines with circles and triangles respectively. The colours indicate the different 15s-long time-windows, starting at 5 s, 25 s, 50 s and 75 s respectively.

Chapter 5

Coda wave sensitivity kernels for monitoring of non-uniform media

Contents

This chapter presents our numerical study on the implications of non-uniform scattering properties on coda wave sensitivity kernels for monitoring applications. The first section starts with a general introduction into sensitivity kernels, based on ray theory.

5.1 An introduction to sensitivity kernels

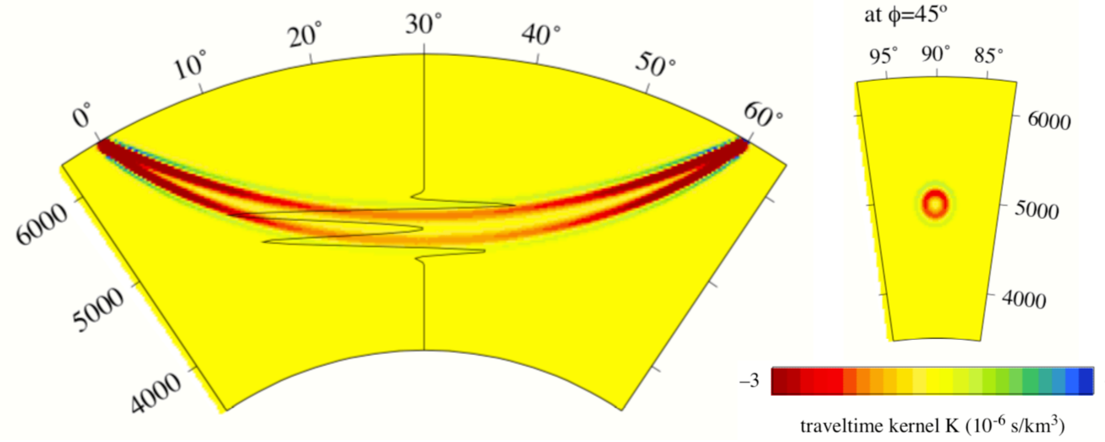

Figure 5.1: 2-D cross-sections through the 3-D 'exact' Frechet kernel K, as seen along (left; banana) and across (right; doughnut) the ray plane for a P wave at an epicentral distance of 60 degrees and a dominant period of 10 s. From Hung, Dahlen, and Nolet (2000)

To introduce the concept of sensitivity, we will look at one of the most well-known examples in seismology, namely travel-time sensitivity kernels used to carry out seismic tomography. In tomography studies, one typically analyses the observed difference between seismograms, for example the variations in wave amplitude and in seismic phase arrival times. A comparison is made between synthetic seismograms in a reference model and observed seismograms. The purpose is to perturb the reference medium such that the model predictions match the observations. The observed differences are caused by the deviation of a physical quantity with respect to its reference model. In the case of travel-time tomography a wave speed perturbation δc, results in a travel-time anomaly ΔT between the observed model and the reference model, via the following relation:

$$T - T_0 = \Delta T = \int_V K \frac{\delta c}{c} dV \tag{5.1}$$

where T_0 denotes the predicted arrival time in the reference model, T the arrival time of the model being studied, V the volume of the Earth or the system and K the Fréchet or *sensitivity kernel.* K quantifies the sensitivity of an observable, in this case the arrival time changes of the seismic phases, to perturbations of a physical quantity, in this case the wavespeed, in a certain medium. According to geometrical ray theory, the spatial sensitivity of a seismic wave to heterogeneities it passes through is limited to the path it followed, i.e. the seismic ray. The travel-time anomaly can then be expressed as:

$$\Delta T = \int_{ray} \frac{1}{\delta c} d\mathbf{x} \tag{5.2}$$

with $\mathbf{x}$ as the position vector. This approximation is, however, only valid if the wavelength λ is much smaller than the average size of the Earth's heterogeneities, $\lambda \ll a$. If $\lambda > a$ the ray becomes sensitive to the heterogeneities of the medium. As the adimensional quantity λ/a increases, the sensitivity spreads out, away from the direct path that connects source and receiver, to a volume referred to as the Fresnel volume. This theory, known as the Born-Fréchet kernel theory, suggests that not the infinitesimally small ray path, but the surrounding material affects the ray velocity. This is in sharp contrast with the previously mentioned ray theory, which defines the ray itself as the only region where the travel-time is sensitive to the medium. The sensitivity in the first zone surrounding the zero sensitivity region, is positive and called the first Fresnel zone. The second Fresnel zone has negative sensitivity. Marquering, Dahlen, and Nolet (1999) named these sensitivity kernels banana-doughnut kernels, due to their shape in the cross-sections along and perpendicular to the source-receiver direction, respectively (Fig. 5.1). A velocity anomaly in the positive (negative) zone will cause an increase (decrease) of travel time with respect to the travel time in the reference medium, respectively. On the other hand, a velocity anomaly in the zero sensitivity zone will not change the travel-time of the ballistic wave, because this zone is not 'explored' by these waves.

For at least ballistic waves, ray theory is a valid approximation to predict the onset of the signal, however it is not appropriate for multiply scattered waves. As we have seen in previous chapters, the RTE is a more suitable propagation model. Similar to eq. (5.1), which links the travel-time perturbation to the velocity changes, Mayor, Margerin, and Calvet (2014) and Margerin et al. (2016) obtained linear expressions relating observations in coda waves to medium perturbations.

In general there are three different observations one can make when monitoring the subsurface with coda waves. Comparing the current and reference recordings, one can observe: (1) delay in travel-time, or phase shift (Section 3.3.1); (2) decorrelation of the waveform (Section 3.3.3); and (3) change in intensity. As demonstrated by Margerin et al. (2016), each observation requires a specific sensitivity kernel. The travel-time kernel, K_{tt}, relates the observed travel-time delay between data for different recording periods, dT, to the macroscopic changes in elastic medium

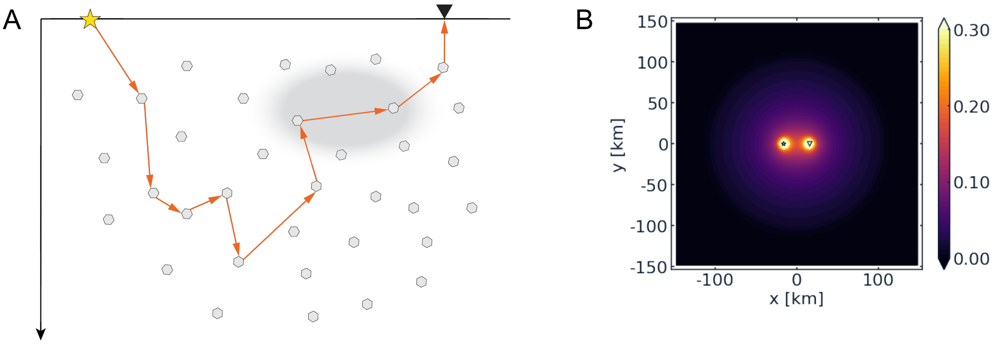

Figure 5.2: Elastic medium perturbation resulting in apparent velocity change. A) Energy traveling from source (yellow star) to receiver (black triangle) via scatterers (grey hexagonals). The red arrows represent the path of the energy, which does not change between time t_1 (reference recording) and t_2 (current recording). The grey area indicates a macroscopic change in medium properties through which the energy travels at time t_2. B) Map view of travel-time sensitivity kernel for uniform scattering medium. Brighter colours indicate higher sensitivities. The small star and triangle depict the source and receiver in the kernel, respectively.

properties, which can be seen as apparent velocity changes:

$$dT(s;r;t;r') = \int_V K_{tt}(s;r;t;r')\frac{\delta v}{v}(r')dV \tag{5.3}$$

with s, r and r' the location of the source, receiver and perturbation, respectively. Fig. 5.2A shows the change in elastic medium properties, depicted by the grey area. An example of a travel-time sensitivity kernel for a uniform medium is shown in panel B. The figure provides a map view with distances on the horizontal and vertical axis, and the high sensitivity areas are around the source and receiver.

A structural change in the subsurface, e.g. opening of fractures, results in a perturbation of scattering strength (Fig. 5.3 A). As a consequence, one can observe a decorrelation of the waveform in the recordings for different periods of time. The decorrelation kernel, K_{dc}, relates this observation with the change in scattering of the medium. The kernel takes into account the new propagation paths which have been created by the additional scatterer. The decorrelation values are expressed using the following relationship (e.g. Larose et al. 2015; Margerin et al. 2016):

$$DC(s;r;t;r') = \frac{c\,\delta\sigma}{2} K_{dc}(s;r;t;r') \tag{5.4}$$

where $\delta\sigma$ is the perturbation in scattering cross-section and c the velocity. Fig. 5.3B shows an example of a decorrelation kernel for a uniform scattering medium. High sensitivities are concentrated on the single scattering ellipse and around the source and receiver.

Another observation for a structural medium change, i.e. the scattering perturbation, is a change in intensity δI. Since the observation is different than in the case of the decorrelation, one needs another sensitivity kernel to relate the medium change with the intensity changes (Mayor, Margerin, and Calvet 2014; Margerin et al. 2016):

$$\frac{\delta I}{I}\left(dV\left(r'\right), t; r, s\right) = \omega \delta Q_{sc}^{-1}\left(r'\right) K_{sc}\left(r', t; r, s\right) dV\left(r'\right) \tag{5.5}$$

with ω the central frequency of the signal, dV a small volume containing the scattering perturbation and $Q_{sc}^{-1}(r)$ the scattering attenuation (Section 2). An example of a scattering kernel is shown in Fig. 5.3C. Similarly as for the decorrelation kernels, the strongest sensitivities are on the single scattering ellipse, but less around the source and receiver. Note that the kernels have been discretised on a relatively fine grid with pixel dimensions of 4-by-4 km, which is 60 times smaller than ℓ. The average kernel is calculated in each pixel, so all the singularities of the kernel are regularised. The kernels shown in Fig. 5.3 & 5.2 are just examples; the actual shape of the kernels

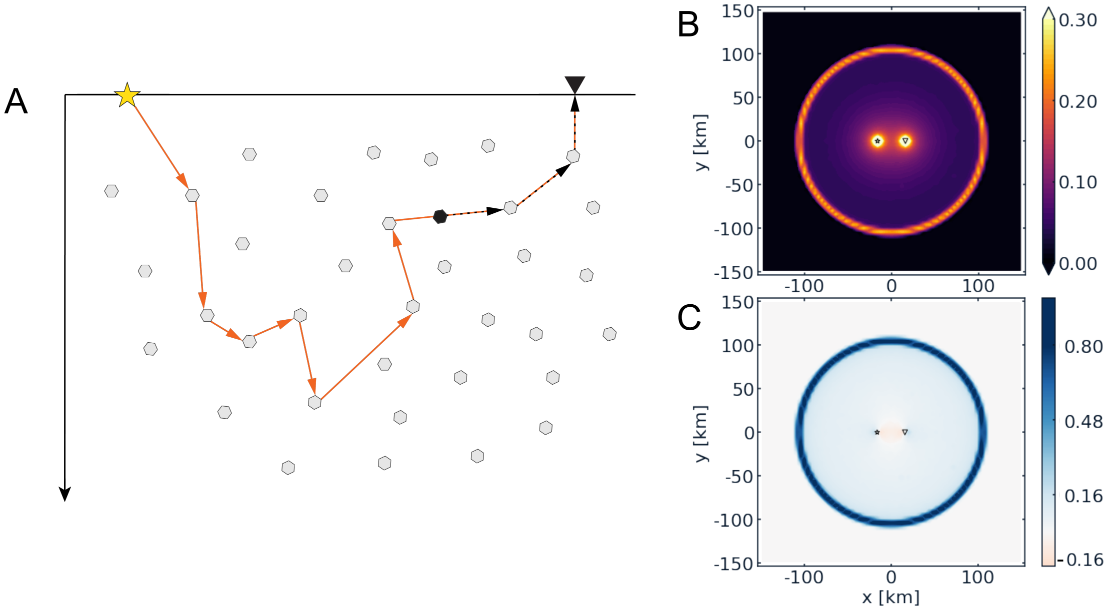

Figure 5.3: Structural medium change, indicated by additional scatterer (black hexagonal). A) Energy traveling from source (yellow star) to receiver (black triangle) via scatterers (grey hexagonals). The red arrows represent the initial path of the energy at time t_1 (reference recording), the black dotted arrows represent the path interacting with the scattering perturbation at time t_2 (current recording). B) Map view of decorrelation sensitivity kernel for uniform scattering medium. Brighter colours indicate higher sensitivities. C) Map view of scattering sensitivity kernel for uniform scattering medium. The blue and red colour indicate the positive and negative sensitivity to scattering, centred around 0. The small star and triangle depict the source and receiver in the kernel, respectively.

depend on the scattering properties and their distribution, the frequency and the lapse-time amongst other factors, as we will see later in this chapter.

The rest of this chapter is devoted to our study on the implications of non-uniform scattering properties on the sensitivities of coda waves. We will start with a general introduction into current studies on coda wave sensitivity kernels, followed by a detailed description of the specific sensitivity kernels that we use and the Monte Carlo method applied to construct them. After a presentation of the three different kernels for a uniform medium, we will provide a comprehensive discussion on the resulting kernels we obtained for non-uniform media, such as a volcanic area, half-space case and fault zone setting. To aid in the interpretation of the kernels, we introduce the interpretation of energy propagation in terms of the three key quantities: the specific energy density, the mean energy density and the energy flux vector.

5.2 Coda wave sensitivity kernels for monitoring of non-uniform scattering media

Chantal van Dinther[1]*, Ludovic Margerin*[2]*, Michel Campillo*[1]

[1] Université Grenoble Alpes, ISTerre, C.N.R.S., B.P. 53, 38041 Grenoble, France.

[2] Institut de Recherche en Astrophysique et Planétologie, Université de Toulouse III Paul Sabatier, C.N.R.S., C.N.E.S, 14, Av. Edouard Belin, 31400 Toulouse, France.

Content of this section has been submitted (in another form) to Journal of Geophysical Research.

5.2.1 Introduction

With the recent advancements in seismic sensor techniques and the rapid deployment of (dense) seismic arrays over the last decade, there has been a surge in the number of monitoring studies trying to capture the dynamic evolution of the subsurface. Due to scattering, coda waves sample a large volume of the subsurface densely for long propagation times and are thus sensitive to small changes of the medium. Consequently, coda waves may be more suitable to characterise temporal variations of the Earth's crust than direct waves, which only sample a narrow volume along the ray path between the (virtual) source and receiver. Poupinet, Ellsworth, and Frechet (1984) were first to demonstrate the feasibility of monitoring weak changes in apparent velocity caused by fault activity in California using coda waves. Poupinet, Ellsworth, and Frechet (1984) derived these global medium changes by measuring the phase shift between the coda of earthquake doublets. Later, detection of temporal medium changes has been successfully applied in numerous settings including but not limited to: volcanoes (e.g. Sens-Schönfelder and Wegler 2006; Mordret et al. 2010; Brenguier et al. 2016; Hirose, Nakahara, and Nishimura 2017; Sánchez-Pastor, Obermann, and Schimmel 2018; Mao et al. 2019; Obermann et al. 2013b) using the coda of ambient noise cross-correlations, fault zones analysing the coda of earthquake records (e.g. Schaff and Beroza 2004; Peng and Ben-Zion 2006; Wu, Peng, and Ben-Zion 2009; Roux and Ben-Zion 2014) and using noise cross-correlations (Rivet et al. 2014; Brenguier et al. 2008a), and CO_2 and geothermal reservoirs (Hillers et al. 2020; Hillers et al. 2015b; Obermann et al. 2015) using the coda of ambient noise cross-correlations.

Although measurements of temporal medium changes are interesting in its own right, knowledge about their spatial location is necessary to gain more insight into the processes that occur at depth. Geometrical regionalisation can yield a first order estimate on the spatial distribution, but a more sophisticated approach is to perform a (linear) inversion using so-called sensitivity kernels. These spatial weighting functions can provide probabilistic information on which portion of the medium has (on average) been sampled by the wave. The first sensitivity kernels for coda wave interferometry have been introduced by Pacheco and Snieder (2005) under the diffusion approximation. Shortly after, Pacheco and Snieder (2006) provided probabilistic kernels for the single scattering regime. Both kernels are in the form of a spatio-temporal convolution of mean intensities of the coda waves. Obermann et al. (2013b) applied those kernels to invert for structural and temporal velocity changes around the Piton de la Fournaise volcano on Reunion Island. To detect and locate medium changes caused by the M_w 7.9, 2008 earthquake in Wenchuan in China, Obermann et al. (2019) used a 3-D combined sensitivity kernel. However, Margerin et al. (2016) demonstrated that knowledge of the angular distribution of the energy fluxes of coda waves is required for the accurate prediction of sensitivities, in order for it to be valid with an arbitrary distribution of heterogeneities and for all propagation regimes. The authors obtained this by using a radiative transfer approach, which directly predicts specific intensities. Other developments on sensitivity kernels focus on the sensitivity as a function of depth. Obermann et al. (2016) and Obermann et al. (2013a) showed that a linear combination of the 2-D surface wave and 3-D body wave kernels are a decent proxy to describe the sensitivity as function of lapse-time and in depth. A formal approach to couple body and surface waves is provided by Margerin, Bajaras, and Campillo (2019).

Most of these studies on sensitivity kernels provide a solution for statistically homogeneous scattering media, even though it is known that the Earth's crust is not uniform in scattering strength, especially in settings and at scales for which monitoring is interesting such as volcanoes and fault zones. Wegler and Lühr (2001) derived attenuation parameters around the Merapi volcano in Indonesia. The authors found a scattering mean free path (ℓ) as low as 100 m for S waves in the frequency band of 4-20 Hz. They also reported that the scattering attenuation is at least one order of magnitude larger than the intrinsic attenuation around Merapi. Later, Yoshimoto, Wegler, and Korn (2006) estimated scattering attenuation in the north-eastern part of Honshu in Japan. For this volcanic area the authors analysed the coda of earthquake records and reported a scattering coefficient of 0.01 km^{-1} for the frequency of 10 Hz. Another study that analysed the coda of seismograms in a volcanic setting in Japan found the scattering mean free path for P and S waves to be as short as 1 km for the 8-16 Hz frequency band (Yamamoto and Sato 2010). Recently, Hirose, Nakahara, and Nishimura (2019) derived a scattering mean free path around 2 km at Sakurajima volcano in Japan, which is much smaller than the surrounding rock. In a recent study on the western part of the North Anatolian Fault Zone (NAFZ) Dinther, Margerin, and Campillo (2020) also found a strong contrast in scattering ($\sim$ factor of 15), with ℓ=10 km inside the fault zone and ℓ in the order of 150 km outside the fault zone. Gaebler et al. (2019) found similarly small scattering mean free path values along the northern strand of the NAFZ analysing the energy decay of earthquake records with a central frequency of 0.75 Hz. In this work we explore the impact of scattering distribution on coda wave sensitivity kernels. The parametric part of this study (Section 5.2.4) aids in the understanding of the kernels. Finally, we show examples of sensitivity kernels for realistic settings.

5.2.2 Coda-wave sensitivity kernels

When monitoring the sub-surface one tries to invert observations to get information about the perturbation of medium properties. As the name suggests, the sensitivity kernels quantify the spatial and temporal sensitivity of a specific observable to changes in the medium. The kernels facilitate the reconstruction in 2-D or 3-D or the spatial variation of a given physical parameter, such as the wavespeed and scattering properties. Since different observations require the use of different kernels, we compute three types of sensitivity kernels: the travel time kernel K_{tt}, the scattering kernel K_{sc} and the decorrelation kernel K_{dc}.

The travel-time kernel, K_{tt}, relates the observed travel-time delay (or phase shifts) between data for different recording periods to the macroscopic changes in elastic medium properties, which can be seen as apparent velocity changes. In this study we use the kernel as defined by Margerin et al. (2016) and Mayor, Margerin, and Calvet (2014):

$$K_{tt}\left(\mathbf{r}', t; \mathbf{r}, \mathbf{r}_0\right) = S^D \int_0^t \int_{S^D} \frac{I\left(\mathbf{r}', t-t', -\mathbf{n}'; \mathbf{r}\right) I\left(\mathbf{r}', t', \mathbf{n}'; \mathbf{r}_0\right) dt' dn'}{I\left(\mathbf{r}, t; \mathbf{r}_0\right)} \tag{5.6}$$

where S^D denotes the unit sphere in space dimension D, as well as its area. The intensity propagators I, for the energies traveling from source ($\mathbf{r}$) to receiver ($\mathbf{r}_0$), via a perturbation ($\mathbf{r}'$), are based on the 2-D radiative transfer equation (RTE; Sato (1993) and Paasschens (1997)). Note that the intensity has dimension $[L]^{-D}$ (Paasschens 1997) so that the kernel has dimension $[t][L]^{-D}$. The use of specific intensities implies that we keep track of the directivity of the energy propagation ($\mathbf{n}'$). The kernels are thus valid for all propagation regimes, not just for the diffusion regime. The validity of the kernels also holds for anisotropic scattering, although we consider only isotropic scattering in current work. Previously, Mayor, Margerin, and Calvet (2014) introduced a sensitivity kernel for the perturbation of intensity caused by a local change in absorption. In Margerin et al. (2016) this sensitivity kernels is reinterpreted probabilistically. The kernels are a time density, such that they are equal to the time spent by the waves around a given point, per unit volume or surface.

A structural change in the sub-surface, e.g. the growth of a fault, results in a perturbation of scattering. As a consequence, one can observe a decorrelation of the waveform in the recordings for different periods of time. The decorrelation kernel, K_{dc}, relates this observation with the change in scattering of the medium. The kernel takes into account the new propagation paths which have been created by the addition of scatterers, and is defined as follows (Planès et al. 2014; Margerin et al. 2016):

$$K_{dc}\left(\mathbf{r}', t; \mathbf{r}, \mathbf{r}_0\right) = \int_0^t \frac{I\left(\mathbf{r}', t-t'; \mathbf{r}\right) I\left(\mathbf{r}, t'; \mathbf{r}_0\right) dt'}{I\left(\mathbf{r}, t; \mathbf{r}_0\right)} \tag{5.7}$$

Another observation for the same medium change, i.e. the scattering perturbation, is a change in intensity δI. Since the observation is different than in the case of the decorrelation, one needs another sensitivity kernel. Physically, a perturbation in scattering located in a volume $\mathrm{d}V(\mathbf{r}')$ has two effects on the intensity. (1) An energy loss, which can be quantified by evaluating the seismic phonons that cross $\mathrm{d}V(\mathbf{r}')$. This is effectively what can be monitored with K_{tt}. (2) An increased probability of energy reaching the receiver due to the additional paths created by the additional scatterer. This is effectively what K_{dc} could provide us with. Therefore the scattering sensitivity kernel, K_{sc} as derived by Mayor, Margerin, and Calvet (2014) is defined as:

$$K_{sc}\left(\mathbf{r}', t; \mathbf{r}, \mathbf{r}_0\right) = K_{dc}\left(\mathbf{r}', t; \mathbf{r}, \mathbf{r}_0\right) - K_{tt}\left(\mathbf{r}', t; \mathbf{r}, \mathbf{r}_0\right) \tag{5.8}$$

A characteristic of this kernel is that the integral over all detection points $\mathbf{r}$ gives 0, implied by the conservation of energy as demonstrated in the work of Mayor, Margerin, and Calvet (2014). We will also find in the results (e.g. Fig. 5.4) that the kernels have both positive and negative sensitivities to scattering perturbations. In other words, the spatial contribution of intensities is modified but the total intensities remain unchanged.

5.2.3 Calculation of sensitivity kernels: a Monte Carlo simulation approach

To compute the above defined sensitivity kernels we perform Monte Carlo simulations based on the 2-D RTE with isotropic scattering. This section is rather technical in nature and may be read independently from the rest of the manuscript. We recall that in a Monte-Carlo approach, the transport of energy is represented by random walks of discrete seismic "phonons" (Shearer and Earle 2004) that undergo a sequence of collisions in a scattering and absorbing medium. In practice, the medium is often discretised onto elementary volumes where the number of phonons is monitored as a function of time to estimate the energy density. But it is also possible to compute the energy density detected at a specific point of the medium by evaluating the probability for the phonon to return to the receiver at each scattering event (see e.g. Hoshiba 1991, for a detailed treatment). In the present work, we adopt the latter approach.

Differential Monte-Carlo approach.

While early applications focused mostly on the computation of energy envelopes, the introduction of sensitivity kernels based on RTE has stimulated the development of

Monte-Carlo approaches to compute the derivatives of seismogram envelopes with respect to attenuation model parameters. In a recent investigation of PKP precursors, Sens-Schönfelder, Bataille, and Bianchi (2020) use Monte-Carlo simulations to compute the forward and backward intensities propagating from the source to the perturbation and from the receiver to the perturbation, respectively. The convolution integral in Eq. (5.7)-(5.8) is then evaluated numerically. The method highlights very nicely the regions of the deep Earth contributing to the detection of precursors. Takeuchi (2016) introduced a differential Monte-Carlo method where both the envelope and its partial derivative are calculated in a single simulation. An interesting application of the method, highlighting both the lateral and depth dependence of attenuation in Japan, has been provided by Ogiso (2019). In this work, we also employ the differential approach but in a way quite distinct from Takeuchi (2016). For clarity, we recall the basic ingredients of the method in this section and present our implementation in the next.

The central idea of the differential Monte-Carlo method is best explained with an example (see Lux and Koblinger 1991, for a detailed treatment). Consider for instance the impact of a perturbation of the scattering coefficient on the energy density. Suppose that a seismic phonon has just been scattered at point $\mathbf{r}'$ in a reference medium with scattering coefficient g. The probability density function (pdf) of the position $\mathbf{r}$ of the next collision point may be written as:

$$P(\mathbf{r};\mathbf{r}'|g) = g(\mathbf{x})e^{-\displaystyle\int_{\mathbf{r}'}^{\mathbf{r}} g(\mathbf{x})dx}, \tag{5.9}$$

where the integral is carried on the ray connecting the point $\mathbf{r}'$ to the point $\mathbf{r}$. Note that we allow the scattering coefficient to vary spatially in the reference medium. The distribution of path length in the perturbed medium is obtained by the substitution $g \to g + \delta g$ in Eq. (5.9). In the differential Monte-Carlo method, the envelopes in the reference and perturbed medium are calculated simultaneously via a biasing scheme for the latter (Lux and Koblinger 1991). To picture the idea, one may imagine a "true" phonon propagating in the reference medium and a "virtual" mate following exactly the same trajectory as the "true" phonon albeit in the perturbed medium. As the latter propagates in the reference medium, the statistical weight of its virtual mate is updated to compensate exactly for the genuine frequency of occurrence of the path in the perturbed medium. As an example, let us consider the change of weight occurring after the phonon has left the collision point $\mathbf{r}'$ until it is scattered again at point $\mathbf{r}$. Denoting by w the correction factor, we find:

$$\begin{aligned} w(\mathbf{r};\mathbf{r}') =& \frac{P(\mathbf{r};\mathbf{r}'|g+\delta g)}{P(\mathbf{r};\mathbf{r}'|g)} \\ =& \frac{(g(\mathbf{r})+\delta g(\mathbf{r}))e^{-\int_{\mathbf{r}'}^{\mathbf{r}} \delta g(\mathbf{x})dx}}{g(\mathbf{r})} \end{aligned} \tag{5.10}$$

An obvious condition of applicability is that $g(\mathbf{r}) > 0$, implying that a collision is indeed possible at the point $\mathbf{r}$ in the reference medium. We also remark that there is no assumption on the 'smallness' of δg in the derivation of (5.10). For the computation of sensitivity kernels, we thus further require $\delta g/g \ll 1$ and perform a Taylor expansion to obtain (Takeuchi 2016; Ogiso 2019):

$$w(\mathbf{r};\mathbf{r}') = 1 + \frac{\delta g(\mathbf{r})}{g(\mathbf{r})} - \int_{\mathbf{r}'}^{\mathbf{r}} \delta g(\mathbf{x})dx \tag{5.11}$$

The interpretation of the above formula is as follows: as the virtual phonon propagates between the two collision points $\mathbf{r}'$ and $\mathbf{r}$, its weight decreases progressively following the integral term; at the collision point $\mathbf{r}$, its weight undergoes a positive jump $\delta g(\mathbf{r})/g(\mathbf{r})$. These two contributions may respectively be related to the loss and gain terms in Eq. (5.8). There are two difficulties in the practical application of formula (5.11). The first one becomes apparent when one discretizes the kernel onto a grid of pixels (in 2-D, or voxels in 3-D): the path of the particle inside each pixel has to be carefully monitored to calculate the integral in Eq. (5.11). Such particle tracking can be at the origin of significant computational overhead. The other difficulty is inherent to the spatial variation of the scattering coefficient. Generating the exact path length distribution for the pdf (5.9) involves the computation of the line integral of g which may be very time consuming. In what follows, we propose a method that solves both of these issues by transferring all the sensitivity computation to collision points. A strength of the method is that particle tracking is minimal. Furthermore, a completely arbitrary distribution of scattering properties -including discontinuities of the scattering coefficient- may be implemented transparently and in an “exact” fashion. The main drawback of the approach is that the introduction of statistical weights may result in an increase of the variance of the results. For the applications at hand, we did not find this issue to be limiting.

The method of null or delta collisions

We begin by recalling a simple and very efficient method to simulate the transport of energy in an arbitrarily scattering and absorbing medium, referred to as the method of null or delta collisions (Lux and Koblinger 1991). The starting point is the radiative transfer equation:

$$(\partial_t + c\mathbf{k}\cdot\nabla + \tau(\mathbf{r})^{-1} + t_a(\mathbf{r})^{-1})e(t,\mathbf{r},\mathbf{k}) = \tau(\mathbf{r})^{-1}\int p(\mathbf{k},\mathbf{k}')e(t,\mathbf{r},\mathbf{k}')dk' \tag{5.12}$$

where c, τ, t_a and $p(\mathbf{k},\mathbf{k}')$ refer to the energy velocity, the scattering mean free time, the absorption time and the scattering pattern, respectively. The integral on the right-hand side is carried over all the directions of propagation. We remark that Eq. (5.12) is equivalent to the following modified transport Eq.:

$$\begin{multline}(\partial_t + c\mathbf{k}\cdot\nabla + \tau(\mathbf{r})^{-1} + t_a(\mathbf{r})^{-1} + \tau_\delta(\mathbf{r})^{-1})e(t,\mathbf{r},\mathbf{k}) = \\ \tau(\mathbf{r})^{-1}\int p(\mathbf{k},\mathbf{k}')e(t,\mathbf{r},\mathbf{k}')dk' + \tau_\delta(\mathbf{r})^{-1}\int \delta(\mathbf{k},\mathbf{k}')e(t,\mathbf{r},\mathbf{k}')dk', \end{multline} \tag{5.13}$$

which features a new scattering process with pattern $\delta(\mathbf{k},\mathbf{k}')$ (the delta function on the unit sphere) and mean free time $\tau_\delta(\mathbf{r})$. This new process is characterized by the property that it leaves the propagation direction unchanged. It is worth emphasizing that such delta-collisions or null-collisions do not modify the statistics of true physical scattering events. Because the scattering coefficient of delta-collisions is entirely arbitrary, we may always adjust it in a way such that $\tau_\delta(\mathbf{r})^{-1}+\tau(\mathbf{r})^{-1}+t_a(\mathbf{r})^{-1} = \tau_e^{-1}$, where the extinction time τ_e is fixed. By adding the new scattering process, we have in effect turned a possibly very complicated medium into a much simpler one where the extinction length is constant. This method has been implemented by Dinther, Margerin, and Campillo (2020) to model the scattering of seismic waves across the North-Anatolian fault zone. The price to be paid is that one has to simulate more scattering events than in the original problem. However, in the perspective of computing sensitivities, this is not necessarily a drawback. Indeed, as shown below, all the contributions to the sensitivity come exclusively from collision points in the modified numerical scheme.

Sensitivity computations

We begin by noting that in the numerical simulations, absorption is treated as a phonon capture event, which puts it on the same footing as a scattering event. Indeed, it is important to keep in mind that the extinction time incorporates the three possible types of interactions: physical scattering, delta scattering and absorption. Rather than terminating the phonon history after an absorption event, we ascribe a weight w to the particle. At each collision w is multiplied by a factor equal to the local "survival" probability of the phonon $1 - t_a(\mathbf{r})^{-1}/\tau_e^{-1}$. That this procedure correctly models the exponential decay of the intensity along its path may be demonstrated heuristically as follows. Consider two neighbouring points on the ray path of a seismic phonon and denote by s a spatial coordinate on the ray. If the path length δs is sufficiently small, we may neglect multiple scattering events. In this scenario, either the phonon propagates freely over δs, or it suffers from an additional collision upon which its weight is updated. Hence we have on average:

$$w(s+\delta s) = w(s)\left(1 - \frac{\delta s}{c\tau_e}\right) + w(s)\left(1 - \frac{t_a(s)^{-1}}{\tau_e^{-1}}\right)\frac{\delta s}{c\tau_e} \tag{5.14}$$

where we approximate the scattering probability by $(c\tau_e)^{-1}ds$. Using a Taylor expansion of the left-hand side, simplifying and rearranging terms we obtain:

$$\frac{dw(s)}{ds} = -\frac{w(s)}{ct_a(s)} \tag{5.15}$$

which proves the statement. The same line of reasoning will be used below to calculate the contribution of the path from the last scattering event to the receiver.

Thanks to these preliminaries, it is now straightforward to apply the differential Monte-Carlo method to our problem. As an illustration, let us consider the impact of a scattering perturbation $\delta\tau^{-1}(\mathbf{r})$. Again it is conceptually convenient to consider two phonons: a real phonon propagating in the reference medium and an imaginary phonon propagating in the perturbed medium. We shall also require that the perturbed and unperturbed media have the same extinction time τ_e. Since this parameter can be arbitrarily chosen, this condition can always be fulfilled. By imposing the equality of the extinction time in the reference and perturbed medium, we remove any change of the weight of the virtual phonon in between two collisions. Furthermore, our choice imposes that the rate of delta collisions in the perturbed medium be given by $\tau_\delta^{-1} - \delta\tau$. As a consequence, both delta collisions and physical scattering events contribute to the sensitivity to a scattering perturbation. Following the same reasoning as in the derivation of Eq. (5.10), the weight of the virtual phonon after a delta collision at point $\mathbf{r}$ is updated as follows:

$$w(\mathbf{r}) \to w(\mathbf{r}) \times \frac{\tau_\delta(\mathbf{r})^{-1} - \delta\tau(\mathbf{r})^{-1}}{\tau_e^{-1}} \times \frac{\tau_e^{-1}}{\tau_\delta(\mathbf{r})^{-1}} \to w(\mathbf{r}) \left(1 - \frac{\delta\tau(\mathbf{r})^{-1}}{\tau_\delta(\mathbf{r})^{-1}}\right) \tag{5.16}$$

This last equation highlights that the rate of imaginary collisions must always be strictly positive. The same reasoning applied to a physical scattering event yields:

$$w(\mathbf{r}) = 1 + \delta\tau(\mathbf{r})^{-1}/\tau(\mathbf{r})^{-1} \tag{5.17}$$

Comparing Eq. (5.11) with Eq. (5.16)-(5.17), it is clear that what our method does in effect is to calculate the line integral in (5.11) by a Monte-Carlo approach, where the imaginary collisions serve as sample points for the quadrature. It is however worth noting that we did not make any smallness assumption in the derivation of (5.16)-(5.17). The case of a perturbation of absorption may be treated exactly along the same lines. We find that at imaginary collisions, Eq. (5.16) applies with the substitution $\delta\tau(\mathbf{r})^{-1} \to \delta t_a(\mathbf{r})^{-1}$.

The last point to be discussed concerns the treatment of the return probability of the phonon from the last scattering event at $\mathbf{r}$ to the detector at $\mathbf{d}$ in the method of partial summations of Hoshiba (1991). This probability involves the factor $e^{-\int_{\mathbf{r}}^{\mathbf{d}}(t_a(\mathbf{x})^{-1}+\tau(\mathbf{x})^{-1})dx}$, so that any modification of the attenuation properties affect the line integral. We could of course compute this contribution by traditional methods but we would then lose the benefits of the transfer of the sensitivity to collision points. To remedy this difficulty, we replace the numerical evaluation of the integral by the following Monte-Carlo procedure:

1. Starting from position $\mathbf{r}$, randomly select the distance l to a new collision point on the ray connecting the last scattering point to the detector. Recall that the pdf of l is simply given by $(\tau_e c)^{-1}\exp(-(\tau_e c)^{-1} l)$.
2. At the collision point, modify the weight of the particle by the factor $\tau_\delta(r)^{-1}/\tau_e^{-1}$. Compute the factors affecting the sensitivities to scattering (or absorption) following Eq. (5.16).
3. Repeat (1) until the phonon has traveled beyond $\mathbf{d}$

The probabilistic interpretation of this procedure is as follows: the only possibility for the phonon to reach the detector without additional physical scattering or absorption event is to undergo delta scatterings only. That the weight of the particle decreases as desired can be easily established by following the same argument as in the derivation of (5.14).

In numerical applications, the kernels are discretised onto pixels whose dimensions fix the lower bound for the spatial resolution that may be achieved in an inversion. As a consequence, the discretised kernels introduce both spatial and temporal averaging as compared to their analytical counterparts (Mayor, Margerin, and Calvet 2014). A positive consequence is that all singularities are automatically regularized, which allows for a more straightforward application of the kernels. Furthermore, whereas analytical kernels are attached to the uniform reference medium, the Monte-Carlo approach lends itself naturally to an iterative linearized inversion procedure. From a numerical perspective, the most important feature of our method is the high degree of flexibility, which allows one to very simply model arbitrary non-uniform scattering and absorbing medium, including the presence of discontinuities in the model parameters. We believe that this simplicity largely balances the slowdown entailed by the simulation of artificial scattering events.

For the simulations we use a grid of 76-by-76 pixels, where each of the pixels has a dimension of 4-by-4 km. The kernel is evaluated every second, up to a maximum lapse-time of 120 s. The final temporal resolution, however, is 5 s, due to the application of a 5 s moving window to average the kernels and reduce the statistical fluctuations. The total number of phonons simulated for each model is 4 $\times 10^9$. The source-receiver distance R equals 32 km for most simulations (uniform and half-space case), with the placement of the source and receiver in the centre of the pixels. Note that reciprocity holds for all the kernels, so physically there is no distinction between source and receiver. Nevertheless, the reference to source and receiver is used to facilitate the discussion of the results. For all simulations the full grid space has a uniform value for the intrinsic quality factor $Q_i^{uni} = 100$, based on values recently derived for a normal crustal setting in Turkey, in the vicinity of the Izmit rupture zone (e.g. Dinther, Margerin, and Campillo 2020). The scattering mean free path varies depending on the model.

5.2.4 Sensitivity kernels for non-uniform scattering media

In this section we discuss the effect of the scattering distribution on the sensitivity kernels. Guided by the results obtained in a volcanic setting, we introduce the physical interpretation for each of the three different kernels. The second context for which we investigate the sensitivity implications caused by non-uniform scattering distribution is for a model with two half-spaces. This case is illustrated with the aid of two parametric studies which facilitate the interpretation of the kernels. We will finish this section with an application to a fault zone model.

To facilitate the discussion we compare the results for all three non-uniform models to the kernels for uniform media. The latter are shown in Fig. 5.4 at a lapse-time of 100 s for increasing scattering strengths. The columns from left to right show K_{tt}, K_{sc} and K_{dc}, respectively. The results obtained for a reference medium, with ℓ_1= 30 km, is shown at the top row. The scattering mean free path varies over orders of magnitude in the Earth, therefore we compare the reference medium with weaker scattering media. The middle and lower rows of Fig. 5.4 depict the results for increasing ℓ: 2 $\times \ell_1$ and 8 $\times \ell_1$, respectively. The epicentral distance is fixed at R = 32 km. The numerical results shown in Fig. 5.4 will serve as guides to understand the more complex cases associated to non-uniform scattering properties.

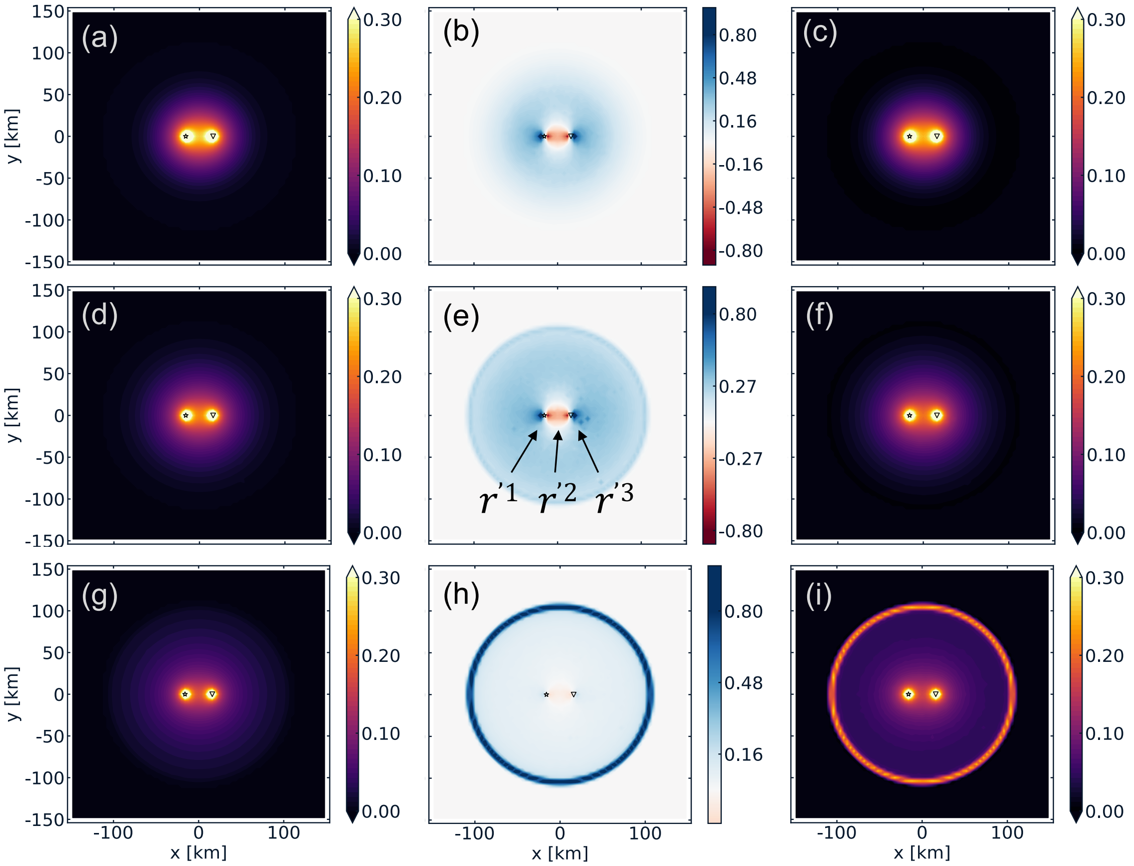

Figure 5.4: Sensitivity kernels for uniform scattering media at 100 s lapse-time. The columns show K_{tt}, K_{sc} and K_{dc}, respectively. The scattering mean free path increases from top to bottom: ℓ_1, $2\times\ell_1$, $8\times\ell_1$, with $\ell_1 = 30$ km. The source-receiver distance, $R_0 = 32$ km. The annotations r'^1- r'^3 point to positive, negative and positive sensitivity along the line connecting source and receiver, respectively. All kernels are normalised with respect to the maximum value. Note that for K_{sc} to colour bar is symmetric around zero, with red as negative and blue as positive sensitivities, respectively.

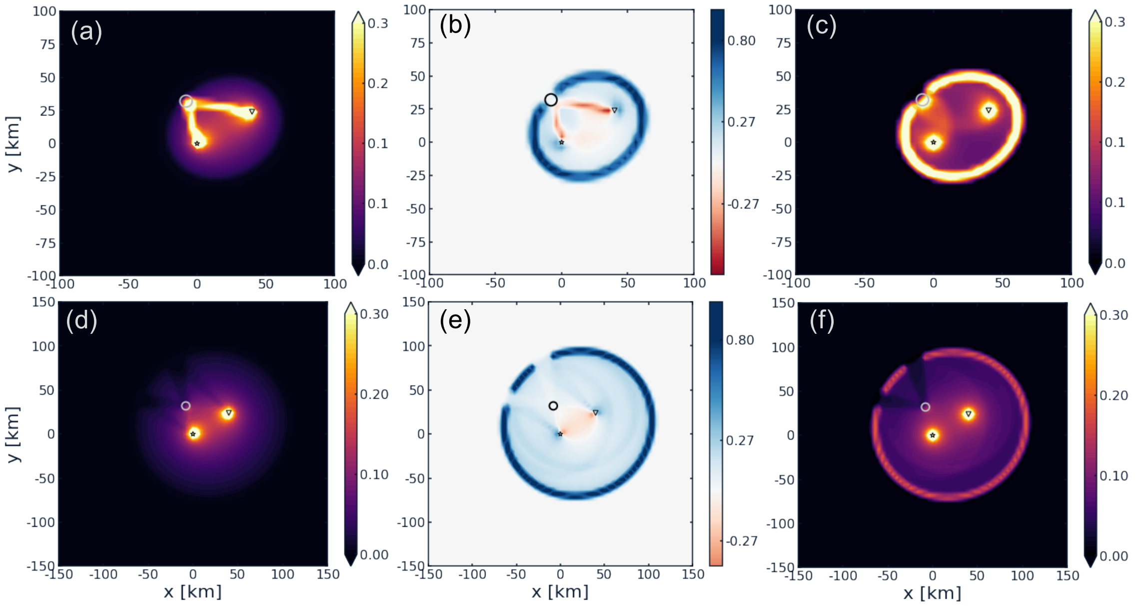

Figure 5.5: Sensitivity kernels for volcanic setting, for lapse-time of 40 s (upper) and 80 s (lower). The columns show K_{tt}, K_{sc} and K_{dc} respectively. The volcano is depicted as a circle with radius $\sqrt{20}$ km and $\ell_v = 2$ km, outside the volcano $\ell = 150$ km. The source-receiver distance is approximately 47 km. Note that axis extent is not the same for 40 s (±100 km) and 80 s (±150 km). All kernels are normalised with respect to the maximum value. The colour bar for K_{sc} is symmetric around zero.

Volcanic setting

Fig. 5.5 shows the kernels for two stations with approximately 50 km inter-station distance, at 40 s (upper row) and 80 s (lower row) lapse-times, in the vicinity of a volcano. The volcano has a radius of $\sqrt{20}$ km and a scattering mean free path of 2 km. This scattering value is based on the findings of Hirose, Nakahara, and Nishimura (2019) at the Sakurajima volcano in Japan. The surrounding crust has a weaker scattering strength with $\ell = 150$ km, and for simplicity the intrinsic absorption is considered uniform with $Q_i = 100$.

There are a couple of observations standing out from Fig. 5.5. First, the travel-

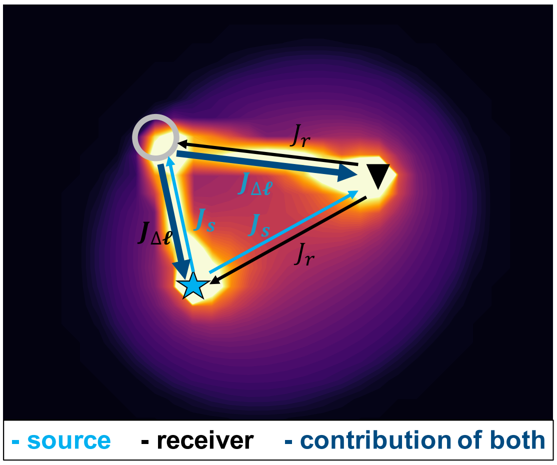

Figure 5.6: Energy fluxes in K_{tt} for volcanic setting. Blue star depicts the source, black triangle the receiver and grey circle the volcano. Flux J_s (J_r) from the source (receiver) to volcano, respectively. Back-scattered energy $J_{\Delta\ell}$, originally from source via volcano to receiver (and vice versa) but it also has a contribution energy coming from source (receiver) that scatters back to the source (receiver), respectively. Both source and receiver emit energy into all directions, also on the direct path between them, as indicated by J_s and J_r.

time and decorrelation kernel are very dissimilar. Second, the volcano appears to be a reflector for the energy fluxes at early lapse-times. To explain these observations and improve the understanding of the kernels we will discuss all three kernels separately and compare them to the uniform case as reference, starting with the travel-time kernel, then the decorrelation kernel and finally the scattering kernel.

As defined in Eq. (5.6), K_{tt} is dependent on the propagation direction of the main waves (indicated by the dependence on $\mathbf{n}'$), that is on the *specific* intensity. There are two intensities in the kernel: (1) the forward intensity from the source to the perturbation; and (2) the backward intensity from the receiver to the perturbation. Where these two intensities are simultaneously high and in opposite direction, the travel-time kernel shows high sensitivities. In the uniform case, the two unique sources of energy fluxes are the source ($\boldsymbol{J_s}$) and receiver ($\boldsymbol{J_r}$). In the case of a localized perturbation with high scattering contrast, energy may be backscattered by the heterogeneity, giving rise to an additional flux $\boldsymbol{J_{\Delta\ell}}$. The dominant fluxes for the volcanic setting are shown in the Fig. 5.6. As a result of the highly scattering volcano, energy fluxes flow from the source towards the volcano (blue $\boldsymbol{J_s}$), and from the volcano to the receiver (blue $\boldsymbol{J_{\Delta\ell}}$). Similarly, energy fluxes flow from the receiver to the volcano (black $\boldsymbol{J_r}$) and from the volcano to the source (black $\boldsymbol{J_{\Delta\ell}}$). Part of the back-scattered energy towards the source (receiver) is the direct reflection of energy that originally came from the source (receiver) itself, respectively. Taking all those fluxes and their overlap into account, for early lapse-time (40 s), we can explain the high sensitivities on the paths connecting source and receiver via the volcano, because the specific intensities are high and opposite in direction at those paths. For the uniform case we can observe higher specific intensities on the source-receiver line, especially for strong scattering media (Fig. 5.4a). This path is less favourable in the volcanic setting, because the specific intensities are much higher on the paths that connect source and receiver via the volcano. With other words, for early lapse-times the volcano creates a secondary energy flux and therefore an additional path favourable to energy transport between source and receiver, which is not present in the uniform case. For later lapse-time (80 s; Fig. 5.5d), K_{tt} resembles its equivalent for a uniform medium. Yet the imprint of the volcano remains as the strongly scattering zone prevents direct energy to travel through and causes a ‘shadow’ in the kernel for late lapse-time.

The decorrelation kernels appear rather different from their travel-time counterparts. Indeed, Eq. (5.7) shows that K_{dc} does not depend on the specific intensities, but on the mean intensities instead. The decorrelation kernel will thus be high where

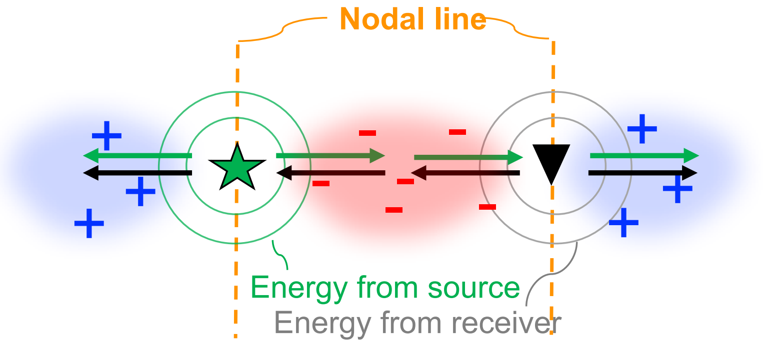

Figure 5.7: Graphical interpretation of the fluxes explaining the pattern of the scattering kernel for a uniform scattering medium. Energy from the source (green star) is emitted in all directions, indicated by the green circles. The green arrows depict the fluxes from the source in the source-receiver line. Similarly, energy from the receiver (black triangle) is emitted in all directions, indicated by the gray circles. The black arrows depict fluxes from the receiver in the source-receiver line. In the space between source and receiver the fluxes have opposite direction, resulting in negative sensitivity (red '-'). In the outside spaces the fluxes from source and receiver have similar directions, resulting in positive sensitivity to scattering (blue '+'). The nodal lines are depicted by the orange dashed line.

the mean intensities emitted by the source, receiver and possible secondary sources are high. For this reason the travel-time and decorrelation kernel are dissimilar. The K_{dc} for the volcanic case at early lapse-time (40s; Fig. 5.5c) shows high sensitivity around the source/receiver and on the single scattering ellipse. Additionally, high sensitivity can be observed in the halos surrounding source and volcano, and receiver and volcano, respectively. Energy becomes rapidly diffuse when it enters into the volcano, therefore the high intensities inside the volcano are on the side that faces the source and receiver. Hence, the bend in the single scattering ellipse. For later lapse-times (80 s; Fig. 5.5f), K_{dc} resembles the uniform K_{dc} (Fig. 5.4i). Nevertheless, the imprint of the strongly scattering volcano remains, causing a 'shadow' on the ellipse of the decorrelation kernel.

The scattering kernel combines the above described properties of the travel-time and decorrelation kernels, as is evident from its definition in Eq. (5.8). In order to understand the scattering kernel in the vicinity of a volcano, we will first discuss the pattern of K_{sc} for the uniform case (e.g. Fig. 5.4 e). As mentioned in Section 5.2.2, the scattering kernel has positive and negative sensitivities. The signs in the kernels can be understood in the following way. If we imagine point sources at the locations of the source and receiver that inject energy into the medium at time $t = 0$. We can consider the energy propagation as a flux, going from source to receiver (and vice versa). At late lapse-times, which is at several scattering mean free times τ (where $\tau = \ell/c$ with c as wave velocity), the energy is diffuse. Previously, it has been shown in the literature that in the diffusion regime the scattering kernel is controlled by the scalar product of the energy flux vectors ($\boldsymbol{J}$) for sources located at the position of the source/receiver (e.g. Arridge 1995; Wilson and Adam 1983; Mayor, Margerin, and Calvet 2014):

$$\lim_{t \to +\infty} K_{\mathrm{sc}}\left(\mathbf{r};\mathbf{r}';\mathbf{r}_0;t\right) = D(1-g)\int_0^t \mathbf{J}_s\left(\mathbf{r}';\mathbf{r};t-t'\right)\cdot\mathbf{J}_r\left(\mathbf{r}';\mathbf{r}_0;t'\right)\mathrm{d}t' \tag{5.18}$$

with g denoting the mean cosine of the scattering angle. Fig. 5.7 shows a schematic diagram of the fluxes in the scattering kernel for a uniform medium. The energy flux from the source flows away in all directions from the source and similarly for the receiver. On the direct path between source and receiver, these fluxes have opposite direction while on the outside the fluxes have similar directions. As a consequence of the scalar product in Eq. (5.18), the fluxes in opposite direction lead to an area of negative sensitivity to scattering on the direct path. Here, the probability of energy reaching the other receiver is decreased. On the outer side of the direct path between source-receiver, there is a positive sensitivity due to the scalar product of the fluxes in similar direction. In these positive areas the probability of energy reaching the other receiver is increased. The line that divides the positive and the negative sensitivities in the vicinity of the source/receiver is referred to as the nodal line (Fig. 5.7). To describe the pattern of the scattering kernel in more detail we imagine placing additional scatterers at three locations in Fig. 5.7. If an extra scatterer would have been placed left of the source, the chances of additional energy reaching the receiver would have been increased due to the possibility of back-scattering. Due to reciprocity, this same argument holds for an additional scatterer right of the receiver. On the other hand, if an additional scatterer would have been placed in the red area, between source and receiver, the chance of energy coming from the source and reaching the receiver would decrease and consequently this area has negative scattering sensitivity to scattering.

Now that we have discussed the positive and negative signs in K_{sc} for a uniform medium we continue the discussion about the volcanic case. K_{sc} will be high in absolute terms where the actual energy fluxes are simultaneously large and aligned, either parallel or anti-parallel. Consequently, an additional energy transport channel in the scattering kernel for early lapse-times (40 s) appears, connecting the source and receiver via the volcano (Fig. 5.5b). The negative sensitivity on the direct path between source and receiver is also present, albeit weaker than on the path via the volcano. Similarly as for K_{tt}, this is due to lower specific intensities on the direct path. Furthermore, we can observe the contribution of the decorrelation kernel to the scattering kernel, for both the early and late lapse-times. In particular, the single scattering ellipse and the halos of high sensitivity, that are also present in K_{dc}, can be observed in Fig. 5.5(b & e). Although K_{sc} for the volcanic setting at late lapse-time (80 s) resembles its equivalent for a uniform model, the effect of the volcano remains.

Half-space setting

In the northeastern region of Honshu, Japan, Yoshimoto, Wegler, and Korn (2006) estimated the spatial distribution of scattering properties and found that the volcanic front separates the front-arc from the back-arc in terms of intrinsic attenuation and scattering coefficients by a factor of two. With this in mind, we explore the effect of non-uniform scattering distribution on the coda wave sensitivities, in a setting with two half-spaces. For all half-space cases, ℓ_1 is the smallest scattering mean free path we consider, it is kept constant at 30 km and consistently on the left side of the model. The right HS has weaker scattering ($\ell_1 < \ell_2$), where ℓ_2 is chosen to vary by a factor of 2, 3, 4 or 8 of ℓ_1. The boundary between the half-spaces is placed exactly at the boundary between two pixels. d represents the distance of source/receiver from a boundary of scattering contrast.

The resulting kernels with stations in opposite half-space are shown in Fig. 5.8, for t =100 s. From the top row to the bottom, we show the results for increasing scattering contrast between ℓ_1 (the reference half-space, on the left) and ℓ_2 (the right half space): $\ell_2 = 2\ \times\ell_1$ (upper), $\ell_2 = 3\ \times\ell_1$ (middle) and $\ell_2 = 8\ \times\ell_1$(lower). The dashed line, placed at 6 km from the source, depicts the boundary between the two half-spaces. The epicentral distance is the same as for the uniform cases, $R =$ 32 km. We can observe that all three kernels for all degrees of scattering contrast are asymmetric, with the asymmetry intensifying as the contrast between ℓ_1 and ℓ_2 increases. In the travel-time kernel there is a strong effect of back-scattering,

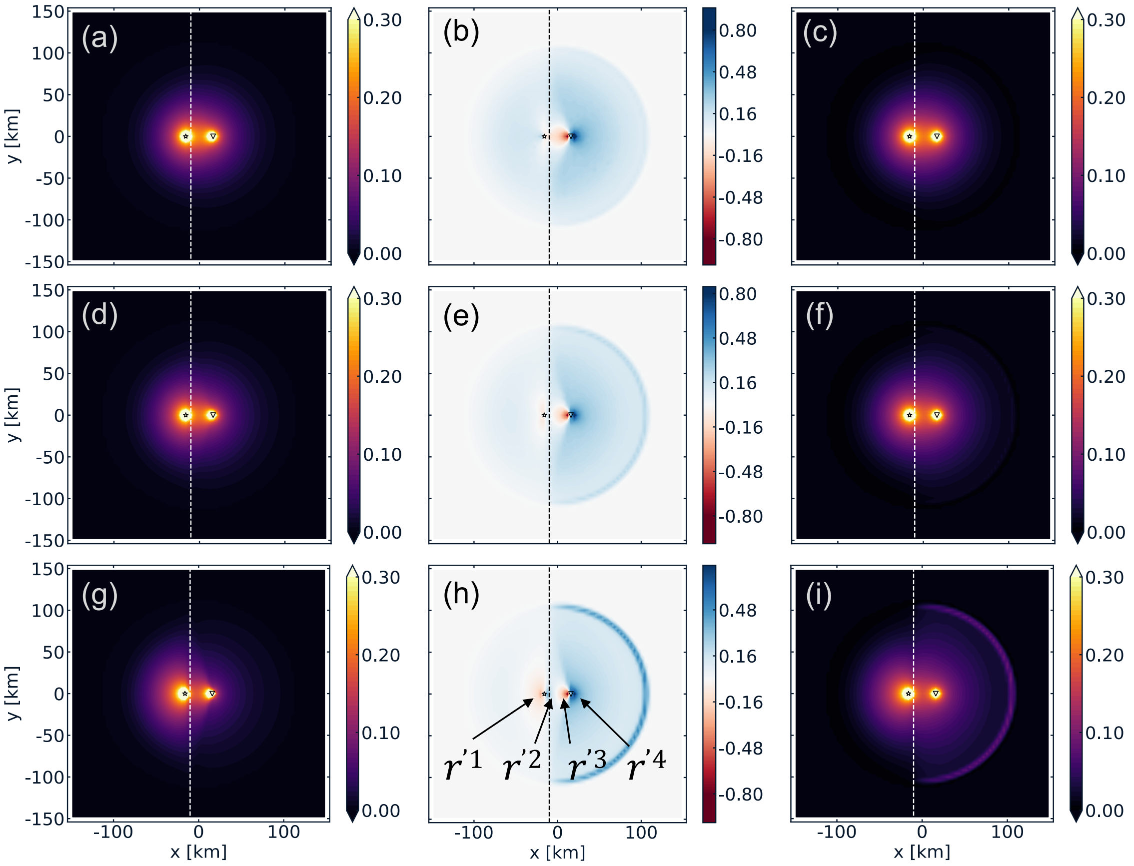

Figure 5.8: Sensitivity kernels for a half-space setting at 100 s lapse-time. The columns show K_{tt}, K_{sc} and K_{dc}, respectively. The scattering mean free path in the right half-space increases from top to bottom: $2\times\ell_1$, $3\times\ell_1$, $8\times\ell_1$, with $\ell_1 = 30$ km. The left half-space has a fixed scattering mean free path of ℓ_1. The source-receiver distance, $R_0 = 32$ km. The annotations r'^1- r'^4 point to negative, positive, negative and positive sensitivity along the line connecting source and receiver, respectively. All kernels are normalised with respect to the maximum value. Note that for K_{sc} the colour bar is symmetric around zero, with red as negative and blue as positive sensitivities, respectively.

especially for the case where $\frac{\ell_2}{\ell_1} = 8$ (Fig. 5.8 g). The specific intensities appear higher in the strong scattering half-space, also between the receiver in the right half-space and the edge of the halo of higher intensities in the left-half space. For the decorrelation kernels we can observe the increased difference between dominant propagation regimes for increasing scattering contrasts. For example in Fig. 5.8 (i) the dominant type of wave propagation in the left HS is diffusion. Therefore, the mean intensity and thus the sensitivity is concentrated in a larger area around the source. However, in the right HS the single scattering is the dominant propagation regime, consequently, strong sensitivities can be observed on the single scattering ellipse. The most striking observation from Fig. 5.8 is the 'flipped' pattern in the scattering kernels (w.r.t. the pattern for the uniform case), for $\frac{\ell_2}{\ell_1} \geq 3$ (Fig. 5.8 e and h). In the strong scattering HS (with ℓ_1), the sensitivity to an additional scatterer left of the source is negative (r'^1 in panel h), while it was positive for the uniform case (Fig. 5.4 e). On the other side of the source (r'^2) it is positive, while for the uniform case it was negative. The sensitivity to an additional scatterer in the weaker scattering HS (with ℓ_2) appears similar to that for the uniform case in the vicinity of the receiver, with negative sensitivity at r'^3 and positive at r'^4, regardless of the scattering strength or contrast.

Fig. 5.8 shows that for a certain scattering contrast, the pattern of the scattering kernel changes significantly w.r.t. the uniform kernel. As explained in the volcano case this is due to the active fluxes: from the source, $\boldsymbol{J_s}$, and receiver, $\boldsymbol{J_r}$, but also the flux governed by the contrast in scattering $\boldsymbol{J_{\Delta\ell}}$. In order to improve our understanding of the 'flipped' scattering kernel for the half-space and to gain more insight into the factors that affect the active fluxes we perform two additional tests.

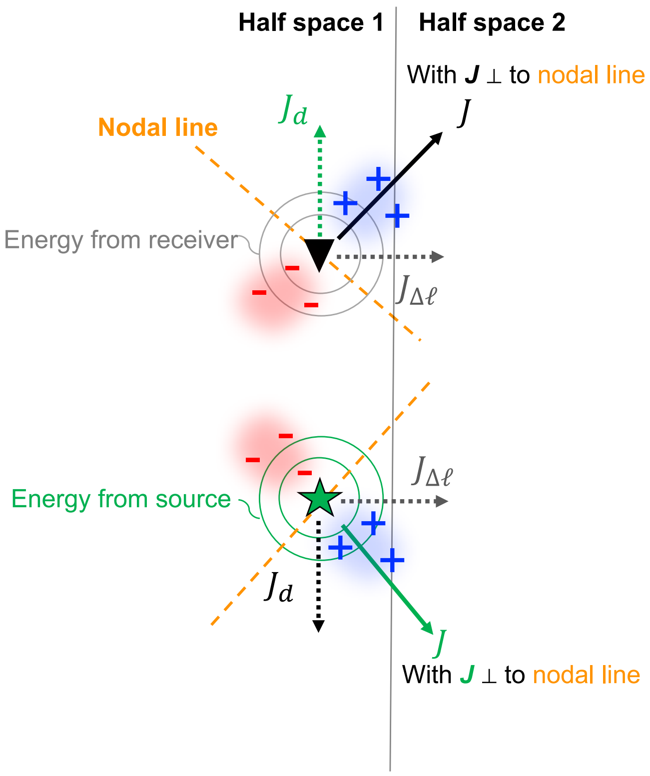

Figure 5.9: Graphical representation of the active fluxes and K_{sc} in case of a medium with two half-spaces. The green fluxes are from the source. The green (black) J_d is the part of the source (receiver) energy in the direction of the receiver (source), respectively. The resulting flux at the source, green J, (receiver, black J) has contributions from J_d and $J_{\Delta\ell}$, where $J_{\Delta\ell}$ is the flux induced by the contrast in scattering, respectively. Nodal line, depicted in orange, separates positive and negative sensitivity to scattering.

In one test we take four models in which the scattering distribution of the medium is fixed, but the location of one of the sources rotates. In another parametric test we investigate the effect of several parameters on the magnitude and directivity of each flux.

If we consider the part of $\boldsymbol{J_s}$ ($\boldsymbol{J_r}$) flowing in the direction of the receiver (source), respectively, as the direct flux $\boldsymbol{J_d}$. Then the current flux at source/receiver is a combination of $\boldsymbol{J_d}$ and $\boldsymbol{J_{\Delta\ell}}$, as illustrated in Fig. 5.9. For the situation in Fig. 5.9,

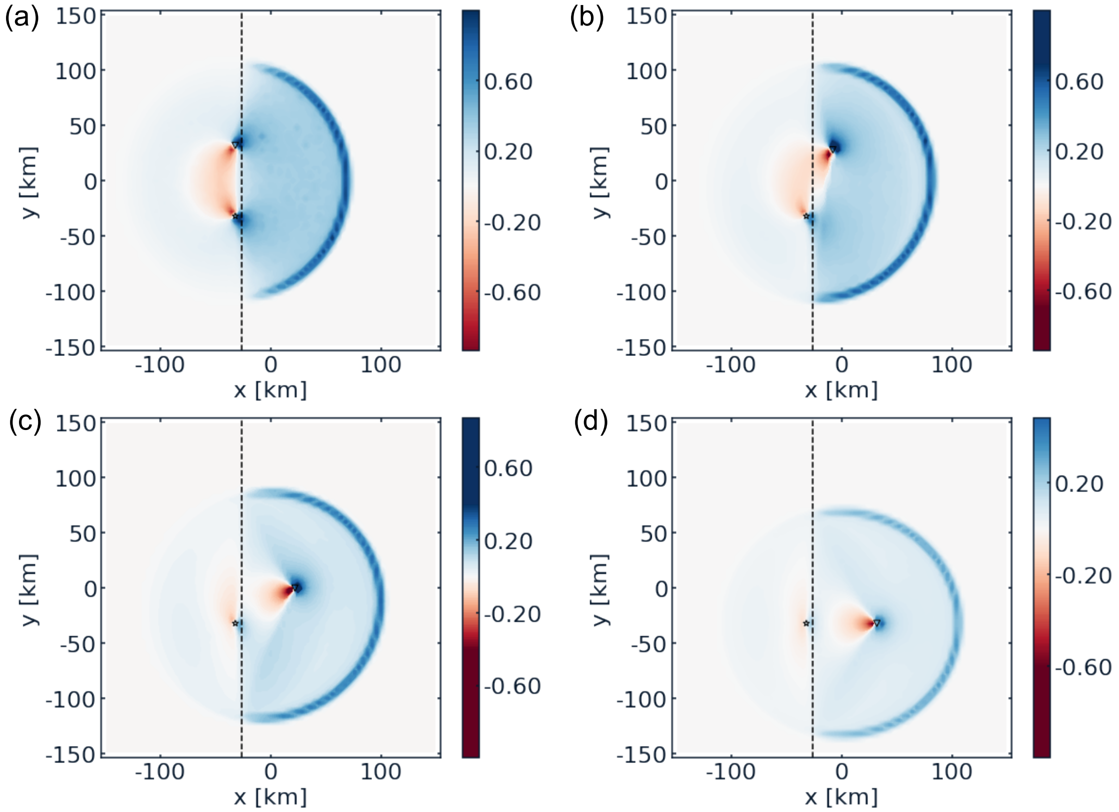

Figure 5.10: Sensitivity kernels for a half-space setting at 100 s lapse-time. The scattering mean free path for the left (right) half-space is fixed for all panels at ℓ_1 ($8\times\ell_1$), respectively. The source-receiver orientation changes gradually from parallel to the boundary to perpendicular to the boundary, from (a) - (d), respectively. To enhance visibility of the kernel pattern the source-receiver distance is larger, with R = 2 x R_0. The distance of the most left source/receiver is fixed at 6 km.

the magnitude of $\boldsymbol{J_{\Delta\ell}}$ depends on the contrast of scattering between both half-spaces. The orientation of $\boldsymbol{J_{\Delta\ell}}$ is perpendicular to the boundary of scattering and from the stronger scattering half-space to the weaker scattering half-space. The orientation of $\boldsymbol{J_d}$ depends on the source and receiver positions, while its magnitude depends on the source-receiver distance and lapse-time.

Fig. 5.10 demonstrates how the direct flux and the flux induced by the scattering contrast contribute to the pattern of the scattering kernel. In all four panels the scattering contrast is the same, with $\frac{\ell_2}{\ell_1} = 8$, and the orientation of $\boldsymbol{J_{\Delta\ell}}$ is perpendicular to the scattering boundary. From panel (a) to (d) the location of the upper source changes, but its distance to the receiver is kept constant at $R = 32$ km ($2 \times R_0$). We rotate the source-receiver orientation from parallel to the boundary (Fig. 5.10 a) to perpendicular to the boundary (Fig. 5.10 d). This causes the orientation of $\boldsymbol{J_d}$ to rotate and therefore the kernel pattern to change from a 'squeezed' version of the uniform kernel (Fig.5.10 a and 5.9) to a kernel with completely opposite sensitivity in the stronger scattering HS (w.r.t. the uniform kernel), as we have already seen in Fig. 5.8 (h).

There are multiple parameters that affect either direction or amplitude of $\boldsymbol{J_d}$, $\boldsymbol{J_{\Delta\ell}}$, and/or relative contribution of both fluxes and therefore the kernels; a selection is shown in Fig. 5.11. The effect in scattering contrast, and as a consequence on $\boldsymbol{J_{\Delta\ell}}$, can be seen when comparing Fig. 5.11 (a) where $\ell_2 = 2 \times \ell_1$ with Fig. 5.11 (b) where $\ell_2 = 8 \times \ell_1$. When we increase ℓ_2 in the right HS from 2 (panel a) to 8 (panel b) we see that the kernel looks more asymmetric. Not only is the sensitivity partly focused on the singly scattering ellipse for the weaker scattering HS, but also in the vicinity of the source and receiver we observe a deformation of the kernel w.r.t. to the uniform case. The angle γ, between the HS boundary and the nodal line, decreases. Note that the nodal line is always perpendicular to the current flux at source/receiver, as show in Fig. 5.7 and 5.9. The change in γ is due to the larger $\boldsymbol{J_{\Delta\ell}}$ induced by the increasing scattering contrast. This alters the magnitude and direction of the current flux, despite the unchanged orientation of the individual fluxes $\boldsymbol{J_{\Delta\ell}}$ and $\boldsymbol{J_d}$. Another parameter that affects the pattern of K_{sc} is the source-receiver distance, which directly affects the contribution of $\boldsymbol{J_d}$ to the current flux. For a larger R the

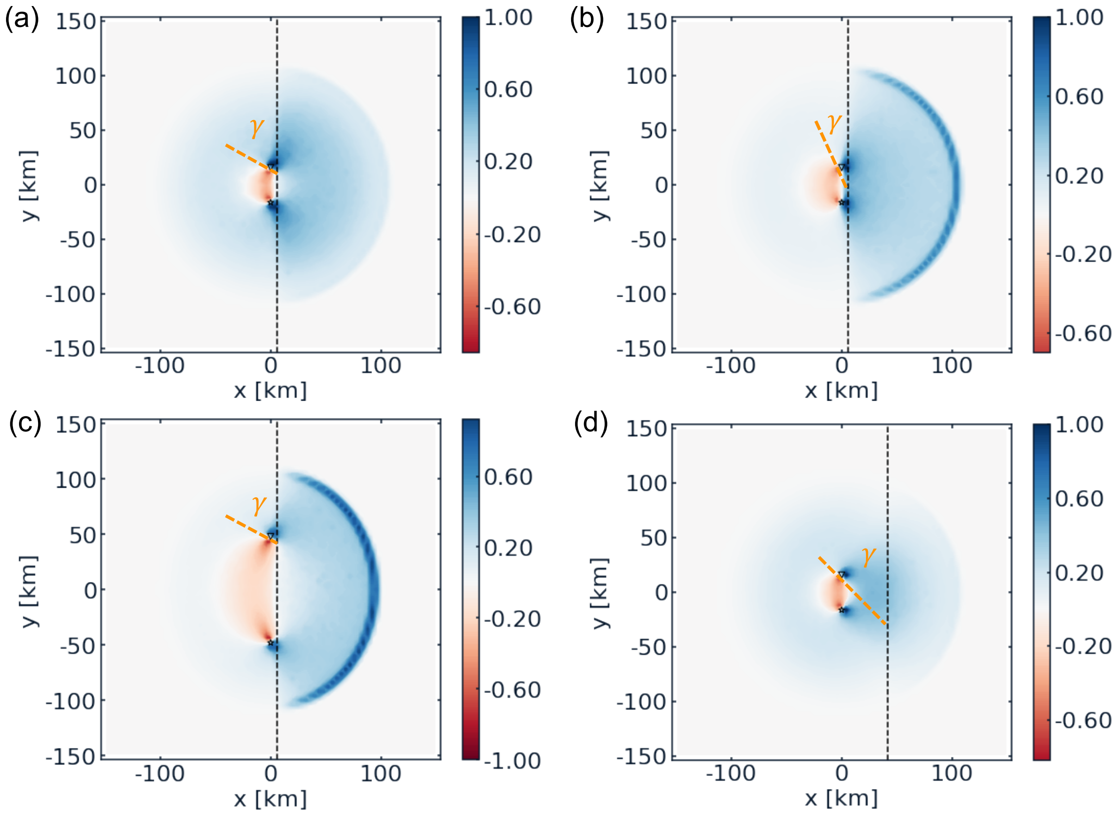

Figure 5.11: Sensitivity kernels for a half-space setting at 100 s lapse-time. Scattering mean free path of left half-space for all panels is ℓ_1= 30 km. Source and receiver are placed parallel to half-space boundary. (a) ℓ of right half-space is $2\times\ell_1$, $R = R_0 =$ 32 km and distance to half-space boundary $d = 6$ km. (b) ℓ of right half-space is $8\times\ell_1$, $R = R_0$ and $d = 6$ km. (c) ℓ of right half-space is $8\times\ell_1$, $R = 3\times R_0$ and $d =$ 6 km. (d) ℓ of right half-space is $8\times\ell_1$, $R = R_0$ and $d = 42$ km. γ denotes the angle between the nodal line (orange dashed line) and the half-space boundary. Note that the colour bar is symmetric around zero.

angle γ increases as can be observed when comparing the kernel for $R = R_0$ (panel B) to $R = 3 \times R_0$ (panel C). Additionally, when comparing Fig. 5.11B to Fig. 5.11D we observe that the distance of the receivers to the boundary of scattering contrast, d, also plays an important role in the pattern of the kernel. The kernel for larger d (panel D) appears more similar to the kernel for uniform scattering (e.g. Fig. 5.4) than the kernel for smaller d (panel B). Thus the effect of the non-uniformity decreases with increasing d. The lack of sensitivity on the singly scattering ellipse (panel D) is a consequence of the energy being already diffuse before reaching the weaker scattering half-space.

Those two tests show that we can improve our interpretation of the scattering kernels by understanding the actual fluxes.

Finally, Fig. 5.12 shows the effect of non-uniform scattering on the kernels for a model with stations far away from the boundary of scattering contrast. The receivers are placed ∼100 km from the contrast of scattering inside the weaker scattering half-space, where $\ell_1 = 30$ km and $\ell_2 = 240$ km. In the travel-time kernel (Fig. 5.12 a) the strong backscattering effect, caused by the contrast in scattering, results in a larger sensitivity towards the strong scattering half-space. This is due to the high specific intensities caused by the opposite fluxes from the strong scattering half-space w.r.t. the fluxes from the source and receiver. This travel-time kernel is rather different from the travel-time kernel for the uniform case, where the sensitivity would have solely be around the source and receiver. The decorrelation kernel shows concentrated sensitivities on the single scattering ellipse, as we have seen in the uniform weakly scattering medium. Furthermore, higher sensitivities can be explained between boundary of scattering on one hand, and the source and receiver

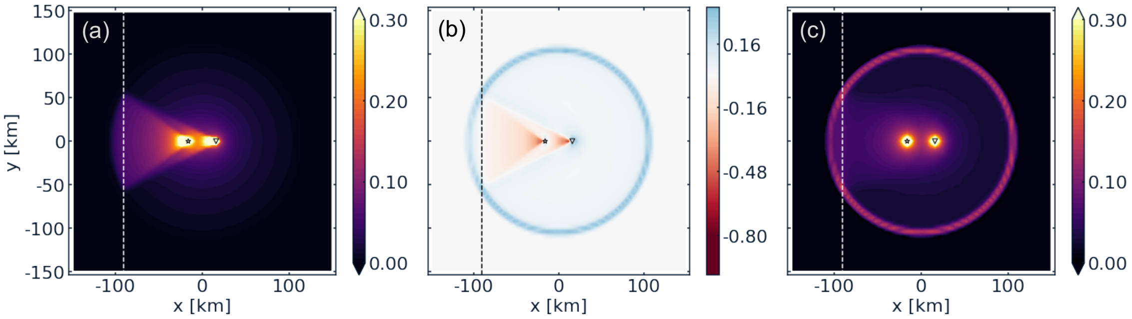

Figure 5.12: Sensitivity kernels for half-spaces at 100 s lapse-time, for a setting where source and receiver are far away from the boundary of scattering contrast (58 and 90 km, respectively). The columns show K_{tt}, K_{sc} and K_{dc}, respectively. All kernels are normalised with respect to the maximum value. The colour bar for K_{sc} is symmetric around zero.

on the other hand, by the increase of mean intensities in those areas. Fig. 5.12 (b) shows that the impact on the scattering kernel is also significant. The contribution of the specific intensities, as in the travel-time kernel, is clearly visible and results in strong negative sensitivities towards the stronger scattering half-space. Furthermore, we can obser the single scattering ellipse, as we have seen in the decorrelation kernels.

The results in Fig. 5.12 thus show that even at large distance from a boundary of scattering contrast the effect of non-uniform scattering properties on the sensitivity kernels can be significant. It is therefore important to have knowledge about the distribution of scattering for a large area around your area of interest, in order to monitor changes of the sub-surface correctly.

Fault zone setting

The last application we consider is a fault zone setting. The parameters are based on findings of the North Anatolian Fault Zone: a narrow fault zone of width = 8 km, with ℓ = 10 km inside and ℓ=150 km outside the fault zone (Dinther, Margerin,

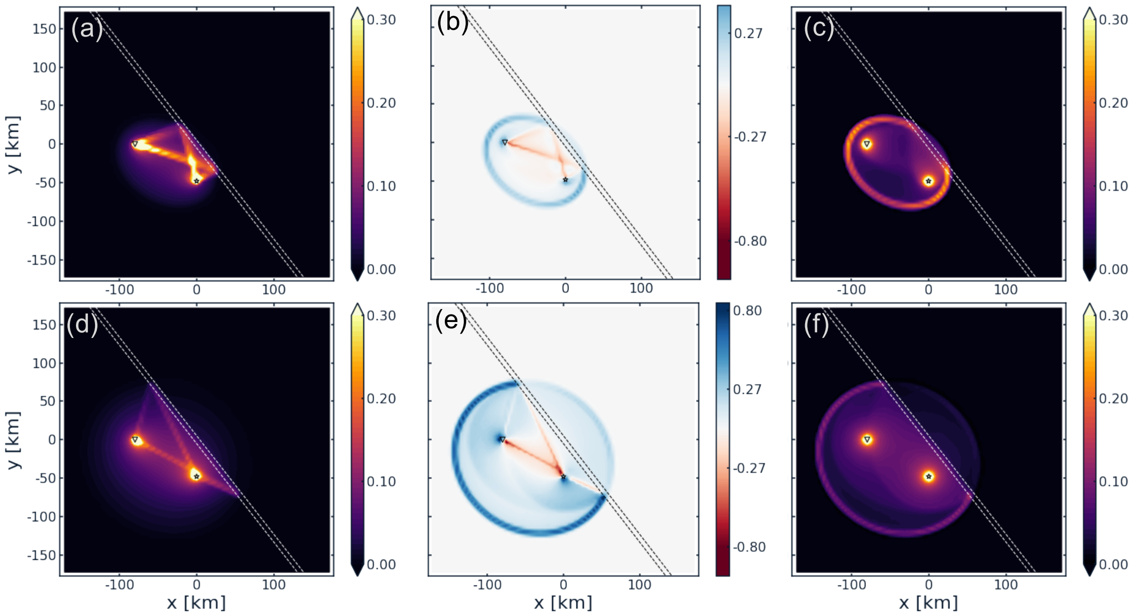

Figure 5.13: Sensitivity kernels for fault zone setting with source and receiver on one side of the fault (dashed lines), for lapse-time of 65 s (upper) and 100 s (lower). The columns show K_{tt}, K_{sc} and K_{dc}, respectively. The width of the fault zone, measured along the horizontal axis is 8 km. The scattering mean free path in and outside the fault zone are $\ell_{FZ} = 10$ km and $\ell = 150$ km, respectively. The interstation distance is approximately 93 km. All kernels are normalised with respect to the maximum value. The colour bar for K_{sc} is symmetric around zero.

and Campillo 2020). Fig. 5.13 shows the resulting kernels for 65 s (upper) and 100 s (lower) lapse-times, respectively. Note that due to the interstation distance of ~ 93 km in combination with a seismic velocity of 2.1 km s^{-1}, the earliest lapse-times for which the kernels are evaluated are around 45 s. The travel-time and scattering kernels may appear slightly more complex than kernels shown for the other non-uniform media. This is due to the additional fluxes from the intersections of the single scattering ellipse with the fault zone towards the source and receiver. Consequently, the overlap of fluxes increases in opposite direction and therefore additional energy transport channels that connect source and receiver are formed in the K_{tt}. In the travel-time kernel for early lapse-time (65 s) we can observe a spot with concentrated sensitivity where the energy transport paths between source (receiver) and fault zone, respectively, cross. At this location the specific intensities are high and in opposite direction. Similarly, the simultaneous large and aligned energy fluxes create additional energy transport paths between source and receiver in the scattering kernel (5.13 b and e). The contribution of the high mean intensities is also visible in K_{sc}, similar to the halos of high sensitivities that are formed around source and receiver in the decorrelation kernel. Again K_{dc} does not resemble K_{tt} and shows that the highly diffusive fault zone acts as a barrier for energy passing through. Hence, the low mean intensity on the right side of the fault zone.

5.2.5 Concluding remarks

For monitoring the temporal evolution of the sub-surface we need coda wave sensitivity kernels that linearly relate observed changes in recordings to physical medium changes. Here we compute travel-time, scattering and decorrelation kernels based on a flexible

Monte Carlo method, which enables us to include non-uniformly distributed scattering properties. In this work we have shown that non-uniform scattering properties can have a profound but non-intuitive effect on coda wave sensitivity kernels. Hence, it would be misleading to neglect the effect of the scattering distribution. The actual impact on the kernels depends on a combination of lapse-time and mean free time, it is therefore important to have knowledge about the geology and an estimate on the scattering mean free path in the wider region that is targeted to be monitored.

There are two unique energy sources, the source and the receiver, for either uniform or non-uniform cases. Yet we have shown that due to non-uniform scattering properties additional energy transport channels can appear between the source and receiver, which do not exist in the case of a uniform scattering medium. Therefore, the sensitivity kernels for non-uniform scattering media can appear rather complex. Although the physical interpretation of the three different kernels is as follows:(1) The decorrelation kernel is the most straightforward to interpret and has high sensitivities where the mean intensities are high. (2) The travel-time kernel requires that the specific intensities are simultaneously large and in opposite direction. (3) The scattering kernel combines the properties of both the decorrelation and travel-time kernel and has high absolute sensitivities where the energy fluxes are simultaneously large and parallel or anti-parallel. Furthermore, the pattern of positive and negative sensitivities in the scattering kernel is controlled by the scalar product of the current fluxes from the source and receiver. The interpretation of the scattering kernel is more intuitive when considering the active energy fluxes.

There are two fluxes contributing to the resulting fluxes around source/receiver: (1) the direct flux between the source and receiver, and (2) the flux induced by the non-uniformity of scattering. The direction and magnitude of these two fluxes in turn depend on several parameters including distance from the boundary of scattering contrast, source-receiver spacing, orientation of the source-receiver line and the scattering contrast. In order to fully understand the kernels, it requires knowledge of these actual fluxes, primarily from the source/receiver and partly governed by the distribution of scattering, because the magnitude and direction of the fluxes may lead to additional pathways for energy transport. Regarding Eq. (5.18), the validity of interpreting the energy propagation as energy fluxes is only valid in the diffusion regime. Yet with our findings it appears that this interpretation may be extended to any propagation regime. However, more rigorous mathematical work is required to prove this.

Finally, this study visually demonstrates the difference between travel-time and decorrelation kernels, although mathematically this has already been shown by Margerin et al. (2016). Therefore, it emphasises that one needs to be careful with applying physical approximations to the wavefield, such as the diffusion approximation that would result in similar decorrelation and travel-time kernels.

Conclusion and outlook

Concluding remarks

The results presented in this thesis deal with the aspect of non-uniform scattering properties as input for subsurface monitoring applications.

In the first part of this thesis I have introduced the main concepts involved in wave scattering of complex media. Chapter 3 discussed the main methods to image attenuation properties using earthquake coda waves, with a focus on separating the scattering and intrinsic attenuation parameters. To improve current spatial resolution whilst excluding the temporal and spatial dependence on earthquake occurrence, one can carry out similar analysis exploiting ambient noise records. Using the previously proven technique of Green's function retrieval by correlation, we successfully constructed cross-correlation functions for a dense array in the eastern part of Northern Anatolia, Turkey 4. Analysis of the spatio-temporal energy decay of these noise based CCFs allowed us to estimate the scattering mean free path and the intrinsic absorption coefficient in the North Anatolian Fault zone, near the Izmit rupture zone. Hence, we demonstrated that a strong scattering fault zone (where ℓ= 10 km) with limited width and a scattering contrast of more than a factor of 10, is a reasonable first order scattering model for the northern strand of this part of the North Anatolian Fault Zone. Furthermore, late diffusive waves in the northern strand of the fault zone and surroundings were observed in the data, and successfully replicated in a numerical simulation. On the contrary, no evidence of a similar strong scattering zone around the southern strand was found.

In Chapter 3, I have also discussed current studies and methodologies on monitoring the Earth's dynamic evolution that can give a first order insight into the magnitude and location of the changes at depth. Most of those existing studies, however, did not consider geological structures and their related scattering properties. Taking into account existing geological information is necessary to improve the correctness of the resulting detection and location of medium changes. Incorporating the scattering properties found in the study on the NAFZ (Chapter 4), we explored in a numerical study the impact of a non-uniform change of scattering properties on the spatio-temporal sensitivity of coda waves (Chapter 5). With a flexible Monte Carlo method, based on radiative transfer theory, we calculated separate sensitivity kernels for three different observables, namely travel-time, coherence and intensity. We demonstrated that laterally varying scattering properties can have a profound effect on the sensitvities of coda waves, for which the actual impact depends on a combination of lapse-time and scattering mean free time. This emphasises again the need to image scattering properties for the target medium. Furthermore, we discussed how the knowledge about the mean intensity, specific intensity and energy flux, partly governed by the distribution of scattering strength, aids in the understanding of the decorrelation, travel-time and intensity kernels, respectively.

The majority of previously proposed coda wave sensitivity kernels for monitoring are valid in the diffusive approximation only, in which there is no dependence on directivity for the energy fluxes. However, we have demonstrated and visually illustrated the importance of the use of specific intensity for the travel-time and scattering kernels, in the context of volcanic and fault zone setting models. Consequently, this emphasises that one needs to be careful with applying physical approximations to the wavefield, such as the diffusion approximation when this is not valid, as that would result in wrong kernels, showing for example incorrectly similar decorrelation and travel-time sensitivity kernels.

To summarize, this thesis contributes to the understanding of laterally varying scattering properties on the spatio-temporal sensitivities of coda waves. Furthermore, it demonstrated the feasibility of estimating scattering and attenuation parameters from ambient noise cross-correlations at short length scale. These contributions are a small step towards better detection and localisation of dynamic changes that occur in the heterogeneous Earth. Other improvements and potential next steps are outlined in the following section.

Outlook and perspectives

The first study in this thesis dealt with imaging of horizontally varying scattering properties in the North Anatolian Fault zone. First order insight on the scattering properties with depth in this region, could be gained by combining the presented results with the imaging results of Touma and colleagues (in prep.), who use a distortion matrix approach to image scatterers at depth. Another aspect, is to improve the estimation of the scattering mean free path outside the fault zone along the northern strand of the NAF. The aperture of the DANA network did not allow for extraction of energy densities at large distances. Combing measurements of other temporary or permanent stations in the region that are at larger distances from the DANA array could provide the opportunity to constrain ℓ outside the fault zone better. Alternatively, high quality earthquake data at low frequencies together with either the DANA array or other stations in the vicinity could allow for estimation of ℓ outside the fault zone too.

A short term future perspective of the work on the sensitivity kernels, is a monitoring application in which we invert for medium changes using the presented non-uniform kernels. Currently, we are working on an inversion application using synthetic data in a realistic fault zone setting. Envelopes for uniform media and fault zone settings are constructed using the presented Monte Carlo simulations. The difference in intensity between those envelopes is used as an observable when inverting for the perturbation in scattering using the scattering sensitivity kernels. In a separate inversion for the same fault zone setting, we invert for apparent velocity changes. We integrate the travel-time kernels in space to obtain the delay times. A linear inversion using the kernel-derived delay times and the presented travel-time kernels will allow us to obtain the spatial distribution of apparent velocity changes. An extension to actual data would be an interesting next step.

A logical continuation of the current work on 2-D sensitivity kernels would be the extension to 3-D, to include depth sensitivity. However, this brings several challenges.

The first challenge, is the required theoretical or computational advancements to solve the radiative transfer equation in 3-D. Monte Carlo simulations are well-known methods to solve the RTE numerically. Unfortunately though, the mayor drawback is their slow convergence. Therefore, if a numerical approach is chosen to calculate 3-D sensitivity kernels, it could potentially benefit from computational advancements, such as a more effective algorithm or an improved computational infrastructure. Furthermore, the extension to 3-D requires the implementation of surface and body wave coupling. A practical proxy to a 3-D sensitivity kernel has been proposed by Obermann et al. (2013a) and Obermann et al. (2016) in the form of a 'combined' kernel. This kernel is a linear combination of 2-D surface wave and 3-D body wave kernels. A formal approach to couple body and surface waves is provided by Margerin, Bajaras, and Campillo (2019), but further development is needed before this theory can be implemented. Advancements in the field of rotational seismology could potentially also provide insights into the contributions of the different wave modes to the coda.

Another interesting future opportunity lies in the implementation of advanced machine learning techniques to improve the quality of the Green's functions. If only high quality noise data is selected for the reconstruction of the Green's function, the overall signal-to-noise ratio may be better. This could improve the spatial sensitivities for monitoring too, due to the more accurate input parameters of the kernels. Furthermore, it could increase the temporal resolution of the observed medium changes.

In the future we may also expect new data recorded with new sensors, such as distributed acoustic sensors (DAS) and rotational sensors. Today, the implementation of measurements from these devices is not straightforward and brings various challenges. Nevertheless, there is ample progress in view to use the theoretical developments presented in this thesis.

Bibliography

Abubakirov, IR and AA Gusev (1990). “Estimation of scattering properties of lithosphere of Kamchatka based on Monte-Carlo simulation of record envelope of a near earthquake”. In: *Physics of the earth and Planetary Interiors* 64.1, pp. 52–67.

Akbayram, Kenan, Christopher C Sorlien, and Aral I Okay (2016). “Evidence for a minimum 52±1 km of total offset along the northern branch of the North Anatolian Fault in northwest Turkey”. In: *Tectonophysics* 668, pp. 35–41.

Aki, Keiiti (1957). “Space and time spectra of stationary stochastic waves, with special reference to microtremors”. In: *Bulletin of the Earthquake Research Institute* 35, pp. 415–456.

— (1969). “Analysis of the seismic coda of local earthquakes as scattered waves”. In: *Journal of geophysical research* 74.2, pp. 615–631.

— (1973). “Scattering of P waves under the Montana LASA”. In: *Journal of Geophysical Research* 78.8, pp. 1334–1346.

Aki, Keiiti and Bernard Chouet (1975). “Origin of coda waves: source, attenuation, and scattering effects”. In: *Journal of geophysical research* 80.23, pp. 3322–3342.

Akinci, A, AG Taktak, and S Ergintav (1994). “Attenuation of coda waves in Western Anatolia”. In: *Physics of the Earth and Planetary Interiors* 87.1-2, pp. 155–165.

Anggono, Titi et al. (2012). “Spatio-temporal changes in seismic velocity associated with the 2000 activity of Miyakejima volcano as inferred from cross-correlation analyses of ambient noise”. In: *Journal of volcanology and geothermal research* 247, pp. 93–107.

Ardhuin, Fabrice, Lucia Gualtieri, and Eléonore Stutzmann (2019). “Physics of ambient noise generation by ocean waves”. In: *Seismic Ambient Noise*, pp. 69–108.

Arridge, Simon R (1995). “Photon-measurement density functions. Part I: Analytical forms”. In: *Applied Optics* 34.31, pp. 7395–7409.

Aslan, Gokhan et al. (2019). “Shallow creep along the 1999 Izmit Earthquake rupture (Turkey) from GPS and high temporal resolution interferometric synthetic aperture radar data (2011–2017)”. In: *Journal of Geophysical Research: Solid Earth* 124.2, pp. 2218–2236.

Baig, Adam M, Michel Campillo, and Florent Brenguier (2009). “Denoising seismic noise cross correlations”. In: *Journal of Geophysical Research: Solid Earth* 114.B8.

Ben-Zion, Yehuda and Charles G Sammis (2003). “Characterization of fault zones”. In: *Pure and Applied Geophysics* 160.3-4, pp. 677–715.

Bensen, GD et al. (2007). “Processing seismic ambient noise data to obtain reliable broad-band surface wave dispersion measurements”. In: *Geophysical Journal International* 169.3, pp. 1239–1260.

Bonnefoy-Claudet, Sylvette, Fabrice Cotton, and Pierre-Yves Bard (2006). “The nature of noise wavefield and its applications for site effects studies: A literature review”. In: *Earth-Science Reviews* 79.3-4, pp. 205–227.

Boué, Pierre et al. (2013). “Teleseismic correlations of ambient seismic noise for deep global imaging of the Earth”. In: *Geophysical Journal International* 194.2, pp. 844–848.

Brenguier, F et al. (2014). “Mapping pressurized volcanic fluids from induced crustal seismic velocity drops”. In: *Science* 345.6192, pp. 80–82.

Brenguier, F et al. (2020). “Noise-based ballistic wave passive seismic monitoring. Part 1: body waves”. In: *Geophysical Journal International* 221.1, pp. 683–691.

Brenguier, Florent et al. (2008a). “Postseismic relaxation along the San Andreas fault at Parkfield from continuous seismological observations”. In: *science* 321.5895, pp. 1478–1481.

Brenguier, Florent et al. (2008b). “Towards forecasting volcanic eruptions using seismic noise”. In: *Nature Geoscience* 1.2, pp. 126–130.

Brenguier, Florent et al. (2016). “4-D noise-based seismology at volcanoes: Ongoing efforts and perspectives”. In: *Journal of Volcanology and Geothermal Research* 321, pp. 182–195.

Calvet, Marie and Ludovic Margerin (2013). “Lapse-time dependence of coda Q: Anisotropic multiple-scattering models and application to the Pyrenees”. In: *Bulletin of the Seismological Society of America* 103.3, pp. 1993–2010.

Campillo, Michel (2006). “Phase and correlation inrandom’seismic fields and the reconstruction of the Green function”. In: *Pure and applied geophysics* 163.2-3, pp. 475–502.

Campillo, Michel and Anne Paul (2003). “Long-range correlations in the diffuse seismic coda”. In: *Science* 299.5606, pp. 547–549.

Campillo, Michel et al. (2011). “New developments on imaging and monitoring with seismic noise”. In:

Carcolé, Eduard and Haruo Sato (2010). "Spatial distribution of scattering loss and intrinsic absorption of short-period S waves in the lithosphere of Japan on the basis of the Multiple Lapse Time Window Analysis of Hi-net data". In: *Geophysical Journal International* 180.1, pp. 268–290.

Chaput, J et al. (2015). "Multiple scattering from icequakes at Erebus volcano, Antarctica: Implications for imaging at glaciated volcanoes". In: *Journal of Geophysical Research: Solid Earth* 120.2, pp. 1129–1141.

Claerbout, Jon F (1968). "Synthesis of a layered medium from its acoustic transmission response". In: *Geophysics* 33.2, pp. 264–269.

Clarke, Daniel et al. (2011). "Assessment of resolution and accuracy of the Moving Window Cross Spectral technique for monitoring crustal temporal variations using ambient seismic noise". In: *Geophysical Journal International* 186.2, pp. 867–882.

Colombi, Andrea et al. (2014). "On the temporal stability of the coda of ambient noise correlations". In: *Comptes Rendus Geoscience* 346.11-12, pp. 307–316.

DANA (2012). *Dense Array for North Anatolia.* International Federation of Digital Seismograph Networks doi:10.7914/SN/YH2012.

Del Pezzo, Edoardo, Francesca Bianco, and Gilberto Saccorotti (2001). "Separation of intrinsic and scattering Q for volcanic tremor: An application to Etna and Masaya volcanoes". In: *Geophysical research letters* 28.16, pp. 3083–3086.

Derode, A et al. (2003a). "Recovering the Green's function from field-field correlations in an open scattering medium". In:

Derode, Arnaud et al. (2003b). "How to estimate the Green's function of a heterogeneous medium between two passive sensors? Application to acoustic waves". In: *Applied Physics Letters* 83.15, pp. 3054–3056.

Dinther, Chantal van, Ludovic Margerin, and Michel Campillo (2020). “Laterally varying scattering properties in the North Anatolian Fault Zone from ambient noise cross-correlations”. In: *Geophysical Journal International*.

Duran, Alejandro, Thomas Planès, and Anne Obermann (2020). “Coda-wave decorrelation sensitivity kernels in 2-D elastic media: a numerical approach”. In: *Geophysical Journal International* 223.2, pp. 934–943.

Duvall, Thomas Lee et al. (1993). “Time–distance helioseismology”. In: *Nature* 362.6419, pp. 430–432.

Emre, Ömer et al. (2018). “Active fault database of Turkey”. In: *Bulletin of Earthquake Engineering* 16.8, pp. 3229–3275.

Eulenfeld, Tom and Ulrich Wegler (2016). “Measurement of intrinsic and scattering attenuation of shear waves in two sedimentary basins and comparison to crystalline sites in Germany”. In: *Geophysical Journal International* 205.2, pp. 744–757.

— (2017a). “Crustal intrinsic and scattering attenuation of high-frequency shear waves in the contiguous United States”. In: *Journal of Geophysical Research: Solid Earth* 122.6, pp. 4676–4690.

— (2017b). “Crustal intrinsic and scattering attenuation of high-frequency shear waves in the contiguous United States”. In: *Journal of Geophysical Research: Solid Earth* 122.6, pp. 4676–4690.

Fehler, Michael and Haruo Sato (2003). “Coda”. In: *Pure and applied geophysics* 160.3-4, pp. 541–554.

Fehler, Michael et al. (1992). “Separation of scattering and intrinsic attenuation for the Kanto-Tokai region, Japan, using measurements of S-wave energy versus hypocentral distance”. In: *Geophysical Journal International* 108.3, pp. 787–800.

Fink, Mathias (1992). “Time reversal of ultrasonic fields. I. Basic principles”. In: *IEEE transactions on ultrasonics, ferroelectrics, and frequency control* 39.5, pp. 555–566.

Friedrich, Andree, Frank Krüger, and Klaus Klinge (1998). “Ocean-generated microseismic noise located with the Gräfenberg array”. In: *Journal of Seismology* 2.1, pp. 47–64.

Froment, Berenice, Michel Campillo, and Philippe Roux (2011). “Reconstructing the Green’s function through iteration of correlations”. In: *Comptes Rendus Geoscience* 343.8-9, pp. 623–632.

Gaebler, Peter et al. (2019). “Imaging of shear wave attenuation along the central part of the North Anatolian Fault Zone, Turkey”. In: *Journal of Seismology* 23.4, pp. 913–927.

Giles, PM et al. (1997). “A subsurface flow of material from the sun’s equator to its poles”. In: *Nature* 390.6655, pp. 52–54.

Gouedard, Pierre et al. (2008). “Cross-correlation of random fields: Mathematical approach and applications”. In: *Geophysical prospecting* 56.3, pp. 375–393.

Gusev, AA and IR Abubakirov (1987). “Monte-Carlo simulation of record envelope of a near earthquake”. In: *Physics of the Earth and Planetary Interiors* 49.1-2, pp. 30–36.

Gusev, Alexander A (1995). “Vertical profile of turbidity and coda Q”. In: *Geophysical Journal International* 123.3, pp. 665–672.

Hadziioannou, Céline (2011). “Ondes sismiques en milieu complexe: Mesure des variations temporelles des vitesses”. PhD thesis. Université de Grenoble.

Hadziioannou, Céline et al. (2009). “Stability of monitoring weak changes in multiply scattering media with ambient noise correlation: Laboratory experiments”. In: *The Journal of the Acoustical Society of America* 125.6, pp. 3688–3695.

Hadziioannou, Céline et al. (2011). “Improving temporal resolution in ambient noise monitoring of seismic wave speed”. In: *Journal of Geophysical Research: Solid Earth* 116.B7.

Hennino, R et al. (2001). “Observation of equipartition of seismic waves”. In: *Physical review letters* 86.15, p. 3447.

Hillers, G, M Campillo, and K-F Ma (2014). “Seismic velocity variations at TCDP are controlled by MJO driven precipitation pattern and high fluid discharge properties”. In: *Earth and Planetary Science Letters* 391, pp. 121–127.

Hillers, G et al. (2015a). “Seasonal variations of seismic velocities in the San Jacinto fault area observed with ambient seismic noise”. In: *Geophysical Journal International* 202.2, pp. 920–932.

Hillers, Gregor et al. (2015b). “Noise-based monitoring and imaging of aseismic transient deformation induced by the 2006 Basel reservoir stimulation”. In: *Geophysics* 80.4, KS51–KS68.

Hillers, Gregor et al. (2020). “The 2018 Geothermal Reservoir Stimulation in Espoo/Helsinki, Southern Finland: Seismic Network Anatomy and Data Features”. In: *Seismological Research Letters* 91.2A, pp. 770–786.

Hirose, Takashi, Hisashi Nakahara, and Takeshi Nishimura (2017). “Combined use of repeated active shots and ambient noise to detect temporal changes in seismic velocity: Application to Sakurajima volcano, Japan”. In: *Earth, Planets and Space* 69.1, p. 42.

— (2019). “A Passive Estimation Method of Scattering and Intrinsic Absorption Parameters From Envelopes of Seismic Ambient Noise Cross-Correlation Functions”. In: *Geophysical Research Letters* 46.7, pp. 3634–3642.

Hirose, Takashi et al. (2020). “Locating Spatial Changes of Seismic Scattering Property by Sparse Modeling of Seismic Ambient Noise Cross-Correlation Functions: Application to the 2008 Iwate-Miyagi Nairiku (M w 6.9), Japan, Earthquake”. In: *Journal of Geophysical Research: Solid Earth* 125.6, e2019JB019307.

Hoshiba, Mitsuyuki (1991). “Simulation of multiple-scattered coda wave excitation based on the energy conservation law”. In: *Physics of the Earth and Planetary Interiors* 67.1-2, pp. 123–136.

— (1993). “Separation of scattering attenuation and intrinsic absorption in Japan using the multiple lapse time window analysis of full seismogram envelope”. In: *Journal of Geophysical Research: Solid Earth* 98.B9, pp. 15809–15824.

— (1994). “Simulation of coda wave envelope in depth dependent scattering and absorption structure”. In: *Geophysical research letters* 21.25, pp. 2853–2856.

Hoshiba, Mitsuyuki, Haruo Sato, and Michael Fehler (Jan. 1991). “Numerical basis of the separation of scattering and intrinsic absorption from full seismogram envelope: A Monte-Carlo simulation of multiple isotropic scattering”. In: *Papers in Meteorology and Geophysics* 42, pp. 65–91. DOI: `10.2467/mripapers.42.65`.

Hu, Hefei et al. (2008). “Localization of ultrasound in a three-dimensional elastic network”. In: *Nature Physics* 4.12, pp. 945–948.

Hung, S-H, FA Dahlen, and Guust Nolet (2000). “Fréchet kernels for finite-frequency traveltimes—II. Examples”. In: *Geophysical Journal International* 141.1, pp. 175–203.

Izgi, Gizem et al. (2020). “Crustal seismic attenuation parameters in the western region of the North Anatolian Fault Zone”. In: *Journal of Geodynamics* 134, p. 101694.

Jin, Anshu et al. (1994). "Separation of intrinsic and scattering attenuation in southern California using TERRAscope data". In: *Journal of Geophysical Research: Solid Earth* 99.B9, pp. 17835–17848.

Jing, Yueling, Yuehua Zeng, and Gao Lin (2014). "High-frequency seismogram envelope inversion using a multiple nonisotropic scattering model: Application to aftershocks of the 2008 Wells earthquake". In: *Bulletin of the Seismological Society of America* 104.2, pp. 823–839.

Kahraman, Metin et al. (2015). "Crustal-scale shear zones and heterogeneous structure beneath the North Anatolian Fault Zone, Turkey, revealed by a high-density seismometer array". In: *Earth and Planetary Science Letters* 430, pp. 129–139.

Kanu, Chinaemerem and Roel Snieder (2015a). "Numerical computation of the sensitivity kernel for monitoring weak changes with multiply scattered acoustic waves". In: *Geophysical Supplements to the Monthly Notices of the Royal Astronomical Society* 203.3, pp. 1923–1936.

— (2015b). "Time-lapse imaging of a localized weak change with multiply scattered waves using numerical-based sensitivity kernel". In: *Journal of Geophysical Research: Solid Earth* 120.8, pp. 5595–5605.

King, GCP (1986). "Speculations on the geometry of the initiation and termination processes of earthquake rupture and its relation to morphology and geological structure". In: *Pure and applied geophysics* 124.3, pp. 567–585.

Korn, M (1990). "A modified energy flux model for lithospheric scattering of teleseismic body waves". In: *Geophysical Journal International* 102.1, pp. 165–175.

Larose, Eric et al. (2006). "Correlation of random wavefields: An interdisciplinary review". In: *Geophysics* 71.4, SI11–SI21.

Larose, Eric et al. (2010). “Locating a small change in a multiple scattering environment”. In: *Applied Physics Letters* 96.20, p. 204101.

Larose, Eric et al. (2015). “Locating and characterizing a crack in concrete with diffuse ultrasound: A four-point bending test”. In: *The Journal of the Acoustical Society of America* 138.1, pp. 232–241.

Lobkis, Oleg I and Richard L Weaver (2001). “On the emergence of the Green’s function in the correlations of a diffuse field”. In: *The Journal of the Acoustical Society of America* 110.6, pp. 3011–3017.

Longuet-Higgins, Michael Selwyn (1950). “A theory of the origin of microseisms”. In: *Philosophical Transactions of the Royal Society of London. Series A, Mathematical and Physical Sciences* 243.857, pp. 1–35.

Lux, Iván and László Koblinger (1991). *Monte Carlo particle transport methods: neutron and photon calculations*. CRC Press.

Lyakhovsky, V et al. (2009). “Non-linear damage rheology and wave resonance in rocks”. In: *Geophysical Journal International* 178.2, pp. 910–920.

Lyakhovsky, Vladimir et al. (1997). “Non-linear elastic behaviour of damaged rocks”. In: *Geophysical Journal International* 130.1, pp. 157–166.

Maeda, Takuto, Haruo Sato, and Takeshi Nishimura (2008). “Synthesis of coda wave envelopes in randomly inhomogeneous elastic media in a half-space: single scattering model including Rayleigh waves”. In: *Geophysical Journal International* 172.1, pp. 130–154.

Mao, Shujuan et al. (2019). “High temporal resolution monitoring of small variations in crustal strain by dense seismic arrays”. In: *Geophysical Research Letters* 46.1, pp. 128–137.

Mao, Shujuan et al. (2020). “On the measurement of seismic traveltime changes in the time–frequency domain with wavelet cross-spectrum analysis”. In: *Geophysical Journal International* 221.1, pp. 550–568.

Margerin, L et al. (1999). “Residence time of diffuse waves in the crust as a physical interpretation of coda Q: application to seismograms recorded in Mexico”. In: *Geophysical Journal International* 138.2, pp. 343–352.

Margerin, Ludovic (2005). “Introduction to radiative transfer of seismic waves”. In: *Geophysical Monograph-American Geophysical Union* 157, p. 229.

— (2006). “Attenuation, transport and diffusion of scalar waves in textured random media”. In: *Tectonophysics* 416.1-4, pp. 229–244.

Margerin, Ludovic, Andres Bajaras, and Michel Campillo (2019). “A scalar radiative transfer model including the coupling between surface and body waves”. In: *Geophysical Journal International* 219.2, pp. 1092–1108.

Margerin, Ludovic, Michel Campillo, and Bart Tiggelen (1998). “Radiative transfer and diffusion of waves in a layered medium: new insight into coda Q”. In: *Geophysical journal international* 134.2, pp. 596–612.

Margerin, Ludovic, Michel Campillo, and Bart Van Tiggelen (2000). “Monte Carlo simulation of multiple scattering of elastic waves”. In: *Journal of Geophysical Research: Solid Earth* 105.B4, pp. 7873–7892.

Margerin, Ludovic and G Nolet (2003). “Multiple scattering of high-frequency seismic waves in the deep Earth: PKP precursor analysis and inversion for mantle granularity”. In: *Journal of Geophysical Research: Solid Earth* 108.B11.

Margerin, Ludovic et al. (2009). “Energy partition of seismic coda waves in layered media: Theory and application to Pinyon Flats Observatory”. In: *Geophysical Journal International* 177.2, pp. 571–585.

Margerin, Ludovic et al. (2016). "Sensitivity kernels for coda-wave interferometry and scattering tomography: theory and numerical evaluation in two-dimensional anisotropically scattering media". In: *Geophysical Journal International* 204.1, pp. 650–666.

Marquering, Henk, FA Dahlen, and Guust Nolet (1999). "Three-dimensional sensitivity kernels for finite-frequency traveltimes: the banana-doughnut paradox". In: *Geophysical Journal International* 137.3, pp. 805–815.

Mayeda, Kevin et al. (1992). "A comparative study of scattering, intrinsic, and coda Q- 1 for Hawaii, Long Valley, and central California between 1.5 and 15.0 Hz". In: *Journal of Geophysical Research: Solid Earth* 97.B5, pp. 6643–6659.

Mayor, Jessie (2016). "Regional variations of seismic attenuation in metropolitan France from observations and modeling of the seismic coda". PhD thesis. Université Paul Sabatier-Toulouse III.

Mayor, Jessie, Ludovic Margerin, and Marie Calvet (2014). "Sensitivity of coda waves to spatial variations of absorption and scattering: radiative transfer theory and 2-D examples". In: *Geophysical Journal International* 197.2, pp. 1117–1137.

Meier, Ueli, Nikolai M Shapiro, and Florent Brenguier (2010). "Detecting seasonal variations in seismic velocities within Los Angeles basin from correlations of ambient seismic noise". In: *Geophysical Journal International* 181.2, pp. 985–996.

Mordret, A et al. (2010). "Monitoring of phreatic eruptions using interferometry on retrieved cross-correlation function from ambient seismic noise: Results from Mt. Ruapehu, New Zealand". In: *Journal of Volcanology and Geothermal Research* 191.1-2, pp. 46–59.

Mordret, Aurélien, Nikolaı M Shapiro, and Satish Singh (2014). “Seismic noise-based time-lapse monitoring of the Valhall overburden”. In: *Geophysical Research Letters* 41.14, pp. 4945–4952.

Mordret, Aurélien et al. (2020). “Noise-based ballistic wave passive seismic monitoring. Part 2: surface waves”. In: *Geophysical Journal International* 221.1, pp. 692–705.

Moreau, L et al. (2017). “Improving ambient noise correlation functions with an SVD-based Wiener filter”. In: *Geophysical Journal International* 211.1, pp. 418–426.

Nakata, Nori and Gregory C Beroza (2015). “Stochastic characterization of mesoscale seismic velocity heterogeneity in Long Beach, California”. In: *Geophysical Supplements to the Monthly Notices of the Royal Astronomical Society* 203.3, pp. 2049–2054.

Nakata, Nori et al. (2015). “Body wave extraction and tomography at Long Beach, California, with ambient-noise interferometry”. In: *Journal of Geophysical Research: Solid Earth* 120.2, pp. 1159–1173.

Nakata, Nori et al. (2016). “Body and surface wave reconstruction from seismic noise correlations between arrays at Piton de la Fournaise volcano”. In: *Geophysical Research Letters* 43.3, pp. 1047–1054.

Nishida, K (2013). “Global propagation of body waves revealed by cross-correlation analysis of seismic hum”. In: *Geophysical Research Letters* 40.9, pp. 1691–1696.

Nishida, Kiwamu, Naoki Kobayashi, and Yoshio Fukao (2002). “Origin of Earth’s ground noise from 2 to 20 mHz”. In: *Geophysical research letters* 29.10, pp. 52–1.

Nishimura, Takeshi et al. (2005). “Temporal changes in seismic velocity of the crust around Iwate volcano, Japan, as inferred from analyses of repeated active seismic experiment data from 1998 to 2003". In: *Earth, planets and space* 57.6, pp. 491–505.

Obara, Kazushige and Haruo Sato (1995). "Regional differences of random inhomogeneities around the volcanic front in the Kanto-Tokai area, Japan, revealed from the broadening of S wave seismogram envelopes". In: *Journal of Geophysical Research: Solid Earth* 100.B2, pp. 2103–2121.

Obermann, Anne et al. (2013a). "Depth sensitivity of seismic coda waves to velocity perturbations in an elastic heterogeneous medium". In: *Geophysical Journal International* 194.1, pp. 372–382.

Obermann, Anne et al. (2013b). "Imaging preeruptive and coeruptive structural and mechanical changes of a volcano with ambient seismic noise". In: *Journal of Geophysical Research: Solid Earth* 118.12, pp. 6285–6294.

Obermann, Anne et al. (2015). "Potential of ambient seismic noise techniques to monitor the St. Gallen geothermal site (Switzerland)". In: *Journal of Geophysical Research: Solid Earth* 120.6, pp. 4301–4316.

Obermann, Anne et al. (2016). "Lapse-time-dependent coda-wave depth sensitivity to local velocity perturbations in 3-D heterogeneous elastic media". In: *Geophysical Journal International* 207.1, pp. 59–66.

Obermann, Anne et al. (2019). "4-D Imaging of Subsurface Changes with Coda Waves: Numerical Studies of 3-D Combined Sensitivity Kernels and Applications to the $\mathrm{M}_w7.9, 2008 Wenchuan Earthquake$". In: *Pure and Applied Geophysics* 176.3, pp. 1243–1254.

Ogiso, Masashi (2019). "A method for mapping intrinsic attenuation factors and scattering coefficients of S waves in 3-D space and its application in southwestern Japan". In: *Geophysical Journal International* 216.2, pp. 948–957.

Okay, Aral I and Okan Tüysüz (1999). “Tethyan sutures of northern Turkey”. In: *Geological Society, London, Special Publications* 156.1, pp. 475–515.

Paasschens, JCJ (1997). “Solution of the time-dependent Boltzmann equation”. In: *Physical Review E* 56.1, p. 1135.

Pacheco, C and R Snieder (2006). “Time-lapse traveltime change of singly scattered acoustic waves”. In: *Geophysical Journal International* 165.2, pp. 485–500.

Pacheco, Carlos and Roel Snieder (2005). “Time-lapse travel time change of multiply scattered acoustic waves”. In: *The Journal of the Acoustical Society of America* 118.3, pp. 1300–1310.

Padhy, Simanchal, U Wegler, and M Korn (2007). “Seismogram envelope inversion using a multiple isotropic scattering model: Application to aftershocks of the 2001 Bhuj earthquake”. In: *Bulletin of the Seismological Society of America* 97.1B, pp. 222–233.

Paul, A and M Campillo (2001). “Extracting the Green function between two stations from coda waves”. In: *AGUFM* 2001, S21D–0610.

Paul, Anne et al. (2005). “Empirical synthesis of time-asymmetrical Green functions from the correlation of coda waves”. In: *Journal of Geophysical Research: Solid Earth* 110.B8.

Peng, Zhigang and Yehuda Ben-Zion (2006). “Temporal changes of shallow seismic velocity around the Karadere-Düzce branch of the north Anatolian fault and strong ground motion”. In: *Pure and Applied Geophysics* 163.2-3, pp. 567–600.

Planès, Thomas et al. (2014). “Decorrelation and phase-shift of coda waves induced by local changes: multiple scattering approach and numerical validation”. In: *Waves in Random and Complex Media* 24.2, pp. 99–125.

Poli, P et al. (2012a). "Body-wave imaging of Earth's mantle discontinuities from ambient seismic noise". In: *Science* 338.6110, pp. 1063–1065.

Poli, P et al. (2012b). "Noise directivity and group velocity tomography in a region with small velocity contrasts: the northern Baltic shield". In: *Geophysical Journal International* 192.1, pp. 413–424.

Poli, Piero et al. (2020). "Seasonal and Coseismic Velocity Variation in the Region of L'Aquila From Single Station Measurements and Implications for Crustal Rheology". In: *Journal of Geophysical Research: Solid Earth* 125.7, e2019JB019316.

Poupinet, G, WL Ellsworth, and J Frechet (1984). "Monitoring velocity variations in the crust using earthquake doublets: An application to the Calaveras Fault, California". In: *Journal of Geophysical Research: Solid Earth* 89.B7, pp. 5719–5731.

Poyraz, Selda Altuncu et al. (2015). "New constraints on micro-seismicity and stress state in the western part of the North Anatolian Fault Zone: Observations from a dense seismic array". In: *Tectonophysics* 656, pp. 190–201.

Richards, Paul G and Keiiti Aki (1980). *Quantitative Seismology: Theory and Methods*. Freeman.

Richter, Tom et al. (2014). "Comprehensive observation and modeling of earthquake and temperature-related seismic velocity changes in northern Chile with passive image interferometry". In: *Journal of Geophysical Research: Solid Earth* 119.6, pp. 4747–4765.

Rivet, Diane et al. (2014). "Seismic velocity changes, strain rate and non-volcanic tremors during the 2009–2010 slow slip event in Guerrero, Mexico". In: *Geophysical Journal International* 196.1, pp. 447–460.

Roux, Philippe and Yehuda Ben-Zion (2014). “Monitoring fault zone environments with correlations of earthquake waveforms”. In: *Geophysical Journal International* 196.2, pp. 1073–1081.

Roux, Philippe et al. (2005). “P-waves from cross-correlation of seismic noise”. In: *Geophysical Research Letters* 32.19.

Rytov, Sergei M, Yu A Kravtsov, and Valeryan I Tatarskii (1988). “Principles of statistical radiophysics. Volume 2- Correlation theory of random processes((Book))”. In: *Berlin and New York, Springer-Verlag, 1988, 242.*

Sabra, Karim G et al. (2005). “Surface wave tomography from microseisms in Southern California”. In: *Geophysical Research Letters* 32.14.

Saito, Tatsuhiko (2010). “Love-wave excitation due to the interaction between a propagating ocean wave and the sea-bottom topography”. In: *Geophysical Journal International* 182.3, pp. 1515–1523.

Sánchez-Pastor, Pilar, Anne Obermann, and Martin Schimmel (2018). “Detecting and locating precursory signals during the 2011 El Hierro, Canary Islands, submarine eruption”. In: *Geophysical Research Letters* 45.19, pp. 10–288.

Sánchez-Sesma, Francisco J et al. (2011). “A theory for microtremor H/V spectral ratio: application for a layered medium”. In: *Geophysical Journal International* 186.1, pp. 221–225.

Sato, Haruo (1993). “Energy transportation in one-and two-dimensional scattering media: analytic solutions of the multiple isotropic scattering model”. In: *Geophysical Journal International* 112.1, pp. 141–146.

— (2019). “Isotropic scattering coefficient of the solid earth”. In: *Geophysical Journal International* 218.3, pp. 2079–2088.

Sato, Haruo, Michael C Fehler, and Takuto Maeda (2012). *Seismic wave propagation and scattering in the heterogeneous earth.* Vol. 496. Springer.

Sato, Haruo, Hisashi Nakahara, and Masakazu Ohtake (1997). “Synthesis of scattered energy density for nonspherical radiation from a point shear-dislocation source based on the radiative transfer theory”. In: *Physics of the earth and planetary interiors* 104.1-3, pp. 1–13.

Schaff, David P and Gregory C Beroza (2004). “Coseismic and postseismic velocity changes measured by repeating earthquakes”. In: *Journal of Geophysical Research: Solid Earth* 109.B10.

Şengör, AMC et al. (2005). “The North Anatolian fault: A new look”. In: *Annu. Rev. Earth Planet. Sci.* 33, pp. 37–112.

Sens-Schönfelder, Christoph, K Bataille, and Marcelo Bianchi (2020). “High Frequency (6 Hz) PKPab precursors and their sensitivity to deep Earth heterogeneity”. In: *Geophysical Research Letters*, e2020GL089203.

Sens-Schönfelder, Christoph, Eraldo Pomponi, and Aline Peltier (2014). “Dynamics of Piton de la Fournaise volcano observed by passive image interferometry with multiple references”. In: *Journal of Volcanology and Geothermal Research* 276, pp. 32–45.

Sens-Schönfelder, Christoph, Roel Snieder, and Xun Li (2019). “A model for nonlinear elasticity in rocks based on friction of internal interfaces and contact aging”. In: *Geophysical Journal International* 216.1, pp. 319–331.

Sens-Schönfelder, Christoph and Ulrich Wegler (2006). “Passive image interferometry and seasonal variations of seismic velocities at Merapi Volcano, Indonesia”. In: *Geophysical research letters* 33.21.

Shang, Tieliang and Longsheng Gao (1988a). “Transportation theory of multiple scattering and its application to seismic coda waves of impulse source”. In: *Science in China Series B-Chemistry, Biological, Agricultural, Medical & Earth Sciences* 31.12, pp. 1503–1514.

— (1988b). “Transportation theory of multiple scattering and its application to seismic coda waves of impulse source”. In: *Science in China Series B-Chemistry, Biological, Agricultural, Medical & Earth Sciences* 31.12, pp. 1503–1514.

Shapiro, Nikolai M and Michel Campillo (2004). “Emergence of broadband Rayleigh waves from correlations of the ambient seismic noise”. In: *Geophysical Research Letters* 31.7.

Shapiro, Nikolai M et al. (2005). “High-resolution surface-wave tomography from ambient seismic noise”. In: *Science* 307.5715, pp. 1615–1618.

Shapiro, NM et al. (2000). “The energy partitioning and the diffusive character of the seismic coda”. In: *Bulletin of the Seismological Society of America* 90.3, pp. 655–665.

Shearer, Peter M and Paul S Earle (2004). “The global short-period wavefield modelled with a Monte Carlo seismic phonon method”. In: *Geophysical Journal International* 158.3, pp. 1103–1117.

Singh, Sudarshan and Robert B Herrmann (1983). “Regionalization of crustal coda Q in the continental United States”. In: *Journal of Geophysical Research: Solid Earth* 88.B1, pp. 527–538.

Snieder, Roel (2006). “The theory of coda wave interferometry”. In: *Pure and Applied geophysics* 163.2-3, pp. 455–473.

Snieder, Roel, Alejandro Duran, and Anne Obermann (2019). “Locating velocity changes in elastic media with coda wave interferometry”. In: *Seismic Ambient Noise*, p. 188.

Snieder, Roel et al. (2002). “Coda wave interferometry for estimating nonlinear behavior in seismic velocity”. In: *Science* 295.5563, pp. 2253–2255.

Soergel, Dorian et al. (2020). “Coda-Q in the 2.5–20 s period band from seismic noise: application to the greater Alpine area”. In: *Geophysical Journal International* 220.1, pp. 202–217.

Stehly, L, Michel Campillo, and NM Shapiro (2006). “A study of the seismic noise from its long-range correlation properties”. In: *Journal of Geophysical Research: Solid Earth* 111.B10.

Stehly, Laurent, Paul Cupillard, and Barbara Romanowicz (2011). “Towards improving ambient noise tomography using simultaneously curvelet denoising filters and SEM simulations of seismic ambient noise”. In: *Comptes Rendus Geoscience* 343.8-9, pp. 591–599.

Stehly, Laurent et al. (2008a). “Reconstructing Green’s function by correlation of the coda of the correlation (C3) of ambient seismic noise”. In: *Journal of Geophysical Research: Solid Earth* 113.B11.

— (2008b). “Reconstructing Green’s function by correlation of the coda of the correlation (C3) of ambient seismic noise”. In: *Journal of Geophysical Research: Solid Earth* 113.B11.

Stehly, Laurent et al. (2015). “Monitoring seismic wave velocity changes associated with the Mw 7.9 Wenchuan earthquake: increasing the temporal resolution using curvelet filters”. In: *Geophysical Journal International* 201.3, pp. 1939–1949.

Takahashi, Tsutomu et al. (2007). “Strong inhomogeneity beneath Quaternary volcanoes revealed from the peak delay analysis of S-wave seismograms of microearthquakes in northeastern Japan”. In: *Geophysical Journal International* 168.1, pp. 90–99.

Takano, Tomoya et al. (2020). “Noise-based passive ballistic wave seismic monitoring on an active volcano”. In: *Geophysical Journal International* 220.1, pp. 501–507.

Takeuchi, Nozomu (2016). “Differential Monte Carlo method for computing seismogram envelopes and their partial derivatives”. In: *Journal of Geophysical Research: Solid Earth* 121.5, pp. 3428–3444.

Taylor, G and G Hillers (2020). “Estimating temporal changes in seismic velocity using a Markov chain Monte Carlo approach”. In: *Geophysical Journal International* 220.3, pp. 1791–1803.

Taylor, George, Sebastian Rost, and Gregory Houseman (2016). “Crustal imaging across the North Anatolian Fault Zone from the autocorrelation of ambient seismic noise”. In: *Geophysical Research Letters* 43.6, pp. 2502–2509.

Taylor, George et al. (2019). “Near-surface structure of the North Anatolian Fault zone from Rayleigh and Love wave tomography using ambient seismic noise”. In: *Solid Earth*.

Wang, Qing-Yu et al. (2017). “Seasonal crustal seismic velocity changes throughout Japan”. In: *Journal of Geophysical Research: Solid Earth* 122.10, pp. 7987–8002.

Wang, Qing-Yu et al. (2019). “Evidence of changes of seismic properties in the entire crust beneath Japan after the Mw 9.0, 2011 Tohoku-oki earthquake”. In: *Journal of Geophysical Research: Solid Earth* 124.8, pp. 8924–8941.

Wang, W and PM Shearer (2017). “Using direct and coda wave envelopes to resolve the scattering and intrinsic attenuation structure of Southern California”. In: *Journal of Geophysical Research: Solid Earth* 122.9, pp. 7236–7251.

Wapenaar, Kees et al. (2010a). “Tutorial on seismic interferometry: Part 1—Basic principles and applications”. In: *Geophysics* 75.5, 75A195–75A209.

Wapenaar, Kees et al. (2010b). “Tutorial on seismic interferometry: Part 2—Underlying theory and new advances”. In: *Geophysics* 75.5, 75A211–75A227.

Weaver, Richard, Berenice Froment, and Michel Campillo (2009). “On the correlation of non-isotropically distributed ballistic scalar diffuse waves”. In: *The Journal of the Acoustical Society of America* 126.4, pp. 1817–1826.

Weaver, Richard L (1982). “On diffuse waves in solid media”. In: *The Journal of the Acoustical Society of America* 71.6, pp. 1608–1609.

Weaver, Richard L and Oleg I Lobkis (2001). “Ultrasonics without a source: Thermal fluctuation correlations at MHz frequencies”. In: *Physical Review Letters* 87.13, p. 134301.

Wegler, U (2004). “Diffusion of seismic waves in a thick layer: Theory and application to Vesuvius volcano”. In: *Journal of Geophysical Research: Solid Earth* 109.B7.

Wegler, Ulrich and Birger G Lühr (2001). “Scattering behaviour at Merapi volcano (Java) revealed from an active seismic experiment”. In: *Geophysical Journal International* 145.3, pp. 579–592.

Wegler, Ulrich and C Sens-Schönfelder (2007). “Fault zone monitoring with passive image interferometry”. In: *Geophysical Journal International* 168.3, pp. 1029–1033.

Wilson, Brian C and Gerhard Adam (1983). “A Monte Carlo model for the absorption and flux distributions of light in tissue”. In: *Medical physics* 10.6, pp. 824–830.

Wu, Chunquan, Zhigang Peng, and Yehuda Ben-Zion (2009). “Non-linearity and temporal changes of fault zone site response associated with strong ground motion”. In: *Geophysical Journal International* 176.1, pp. 265–278.

Wu, RS and K Aki (1985). “Elastic wave scattering by a random medium and the small-scale inhomogeneities in the lithosphere”. In: *Journal of Geophysical Research: Solid Earth* 90.B12, pp. 10261–10273.

Wu, Ru-Shan (1985). “Multiple scattering and energy transfer of seismic waves—separation of scattering effect from intrinsic attenuation—I. Theoretical modelling”. In: *Geophysical Journal International* 82.1, pp. 57–80.

Wu, Ru-Shan and Keiiti Aki (1988). “Introduction: Seismic wave scattering in three-dimensionally heterogeneous earth”. In: *Scattering and Attenuations of Seismic Waves, Part I.* Springer, pp. 1–6.

Yamamoto, Mare and Haruo Sato (2010). “Multiple scattering and mode conversion revealed by an active seismic experiment at Asama volcano, Japan”. In: *Journal of Geophysical Research: Solid Earth* 115.B7.

Yao, Huajian, Robert D Van Der Hilst, and Jean-Paul Montagner (2010). “Heterogeneity and anisotropy of the lithosphere of SE Tibet from surface wave array tomography”. In: *Journal of Geophysical Research: Solid Earth* 115.B12.

Yılmaz, Y et al. (1995). “Geological evolution of the late Mesozoic continental margin of Northwestern Anatolia”. In: *Tectonophysics* 243.1-2, pp. 155–171.

Yoshimoto, K, U Wegler, and M Korn (2006). “A volcanic front as a boundary of seismic-attenuation structures in northeastern Honshu, Japan”. In: *Bulletin of the Seismological Society of America* 96.2, pp. 637–646.

Zhan, Zhongwen et al. (2010). “Retrieval of Moho-reflected shear wave arrivals from ambient seismic noise”. In: *Geophysical Journal International* 182.1, pp. 408–420.